universität wien

MASTERARBEIT | MASTER'S THESIS

Titel | Title

Characterization of Phases in Ternary Systems for Soldering Applications

verfasst von | submitted by

Jan-Luca Stampf MU BSc

angestrebter akademischer Grad | in partial fulfilment of the requirements for the degree of

Diplom-Ingenieur (Dipl.-Ing.)

Wien | Vienna, 2024

Studienkennzahl lt. Studienblatt | Degree programme code as it appears on the student record sheet:	UA 066 658
Studienrichtung lt. Studienblatt | Degree programme as it appears on the student record sheet:	Masterstudium Chemie und Technologie der Materialien
Betreut von | Supervisor:	ao. Univ.-Prof. Mag. Dr. Klaus Richter

Table of Contents

List of abbreviations

DTA	differential thermal analysis
SC-XRD	single-crystal X-ray diffraction
SEM	scanning electron microscopy
P-XRD	powder X-ray diffraction

List of equations

List of figures

List of reactions

List of tables

Abstract (English)

The aim of this thesis was to synthesize and characterize previously uncharacterized phases in the ternary systems Al-Fe-Ge, Au-Si-Ti and Au-Ni-Sn. Samples were weighed in according to or near the composition of the desired phase composition and annealed at elevated temperatures with the aim of growing pure and large enough crystals for single-crystal X-ray diffraction. Furthermore, powder X-ray diffraction, scanning electron microscopy, optical microscopy and differential thermal analysis were utilized to analyze the phases. In the Al-Fe-Ge system the phase $\tau 8$ was synthesized and characterized as orthorhombic of space group *Fmm2* with formula Al_7FeGe_2. The observation of split positions in $\tau 8$ give rise to different local coordination models. In the Au-Si-Ti system the phase T2 was synthesized and characterized as cubic of space group *I43d* with formula $Au_{8-x}Si_6Ti_9$ (x ~ 0.9). The structure is best described as clusters of Si_6Ti_9 surrounded by a network of Au atoms and is related to the structure T1 with formula $Au_{10}Si_6Ti_9$. Furthermore, an oxygen-stabilized variant of Si_3Ti_5, Si_3Ti_5O, was discovered and characterized. It was also found that Ti may partially occupy the additional 2(*b*) site instead of oxygen. In the Au-Ni-Sn system, a superstructure of $(Au,Ni)_3Sn_2$ was synthesized and characterized as orthorhombic with space group *Pmma*. The presence of the superstructure in the ternary phase diagram was explored and the area added to the phase diagram.

Abstract (German)

Das Ziel der Diplomarbeit bestand darin, bisher nicht-charakterisierte Phasen in den ternären Systemen Al-Fe-Ge, Au-Si-Ti und Au-Ni-Sn zu synthetisieren und charakterisieren. Proben mit der oder nahe der Zusammensetzung der gewünschten Phase wurden eingewogen und bei erhöhter Temperatur geglüht um große Kristalle für die Einkristall-Analyse herzustellen. Des Weiteren wurden Pulver-Röntgendiffraktometrie, Rasterelektronenmikroskopie, optische Mikroskopie und Differenz-Thermoanalyse eingesetzt um die Phasen zu analysieren. Im Al-Fe-Ge System wurde die Phase $\tau 8$ synthetisiert und als orthorhombische Struktur der Raumgruppe *Fmm2* mit Zusammensetzung Al_7FeGe_2 charakterisiert. Die unterschiedlichen Besetzungsmöglichkeiten der Atompositionen erzeugen unterschiedliche lokale Koordinationen. Im Au-Si-Ti System wurde die Phase T2 synthetisiert und als kubische Struktur der Raumgruppe *I43d* mit Formel $Au_{8-x}Si_6Ti_9$ (x ~ 0.9) charakterisiert. Die Struktur besteht aus Si_6Ti_9 Clustern umgeben von Au Atomen und ähnelt der Struktur von T1 mit Formel $Au_{10}Si_6Ti_9$. Außerdem wurde eine Sauerstoff-stabilisierte Variante von Si_3Ti_5, Si_3Ti_5O, entdeckt und charakterisiert. Die zusätzliche 2(*b*) Punktlage kann auch mit Ti teilbesetzt sein, anstatt vollbesetzt mit Sauerstoff. Im Au-Ni-Sn System wurde eine Überstruktur von $(Au,Ni)_3Sn_2$ synthetisiert und als orthorhombische Struktur der Raumgruppe *Pmma* charakterisiert. Das Vorhandensein der Überstruktur im ternären Phasendiagramm wurde untersucht und ihre Ausdehnung im Phasendiagramm eingezeichnet.

Acknowledgements

I would like to thank my supervisor Prof. Dr. Klaus Richter for his time and support during the diploma thesis. Furthermore, I would like to thank Prof. Dr. Effenberger for the single-crystal X-ray diffraction measurements. Finally, I would like to thank my family and friends for their love and support.

1. Introduction

1.1. Soldering, brazing and ternary intermetallic compounds

In soldering, materials are connected by melting a filler material called a solder, usually a metal or intermetallic formulation, which forms stable intermetallic bonds at the interface. The ideal solder is a eutectic alloy with a sharp and low melting point that forms a strong connection. In non-eutectic alloys the phases crystallize at different temperatures and hence exert plasticity, which can lead to cracks (1). Brazing is the same process as soldering, yet melting of the filler material occurs at higher temperatures. Eutectic alloys which melt at temperatures above 450 °C are preferentially used for brazing instead of soldering, such as Ag-Cu-Ti alloys (2). On the other hand, lead-tin solders are ideal for soldering due to the low eutectic melting point of 184 °C (3). However, due to environmental and health concerns they are prohibited in the European Union in consumer electronics (4) and in the United States for plumbing applications (5). Alternative lead-free solders are often brittle and form whiskers, which reduces stability (6) and can cause short circuits (7) respectively. For example, the ternary eutectic alloy of Ag-Cu-Sn has a melting point of 217 °C (8) and formulations can be used for soldering (9). Yet, interfacial crystallization of Ag_3Sn whiskers weaken the solder connection (10), even if Ag_3Sn whiskers can be reduced by doping the formulation with Ni (11) or increasing cooling speed and decreasing Ag content (12). New intermetallic formulations can have superior properties for soldering, such as strength and wettability (13), low melting point (11), reduced creeping (11), resistance against corrosion (14) and superconductivity (15), depending on the application. For example, the Ag-Cu-Sn eutectic alloy has a higher corrosion resistance to NaCl than Pb-Sn due to the corrosion resistance of intermetallic ε-Ag_3Sn and η-Cu_6Sn_5 phases (14). Therefore, exploration of phase diagrams and containing low melting elements in combinations with different alloying metals is of interest in determining the properties of phases and intermetallic compounds that can affect solder joints. Furthermore, characterizing new compounds and investigation of phase diagrams adds new knowledge for future applications.

1.2. Al-Fe-Ge systems

Due to its similarity to the Al-Fe-Si system, which is used for the creation of eutectic alloys (16), the Al-Fe-Ge system has grown in importance. For example, the intermetallic compound Al_4Ge_2Fe is isostructural to Al_4Si_2Fe (17) and opens the possibility to exchange Si for Ge in semiconductor and soldering applications (18,19). The ternary Al-Fe-Ge system has also shown superior properties compared to its binary systems. For example, addition of Ge to Fe-Al increases hardness (20). Furthermore, the passivation layer of Al 25 at. % Fe 70 at. % and Ge 5 at.% has a higher resistance to sulfuric acid corrosion than Al 25 at. % Fe 75 at. %. (21). Al-Fe-Ge formulations can form amorphous alloys (22–24) or crystalline phases, such as $Al_7Fe_9Ge_5$ (τ3) and $Al_2Fe_6Ge_3$ (τ4) (19,25). Crystalline Al-Fe-Ge phases can have interesting tuneable properties, such as magnetization at low temperatures that increases with increasing Fe content (24). Eight ternary compounds in the Al-Fe-Ge system, τ1 – τ8, have been discovered, out of which six have been characterized structurally (18). Only small amounts of τ6 and τ8 were found at 400 °C and hence could not be characterized regarding their crystal structure (18), but will be investigated in this thesis. The partial phase diagrams of Al-Fe-Ge at 400 °C and at 800 °C are shown in Figure 1.1 and Figure 1.2 respectively. At 400 °C, phase τ6 has tie lines connecting to Al, $Al_{13}Fe_4$, Ge, τ7 and τ8. Phase τ8 has tie lines connecting to Al, $Al_{13}Fe_4$ and τ6. Phases τ6 and τ8 are suggested to be almost stoichiometric phases (18). Both τ8 and τ6 are stable at 400 °C and were also found in small amounts from samples annealed at 800 °C, not stable, but formed out of the liquid during quenching (19). Preliminary investigations of τ6 and τ8 indicated a non-cubic structure, as microscopic analyses with cross-polarized light showed anisotropic properties for both structures (18). τ8 was suggested to be of body-centred orthorhombic structure containing lattice parameters a = 6.89 Å, b = 7.95 Å and c = 8.77 Å (18). Phases in the Al-Fe-Ge system relevant to the current thesis are given in Table 1.1.

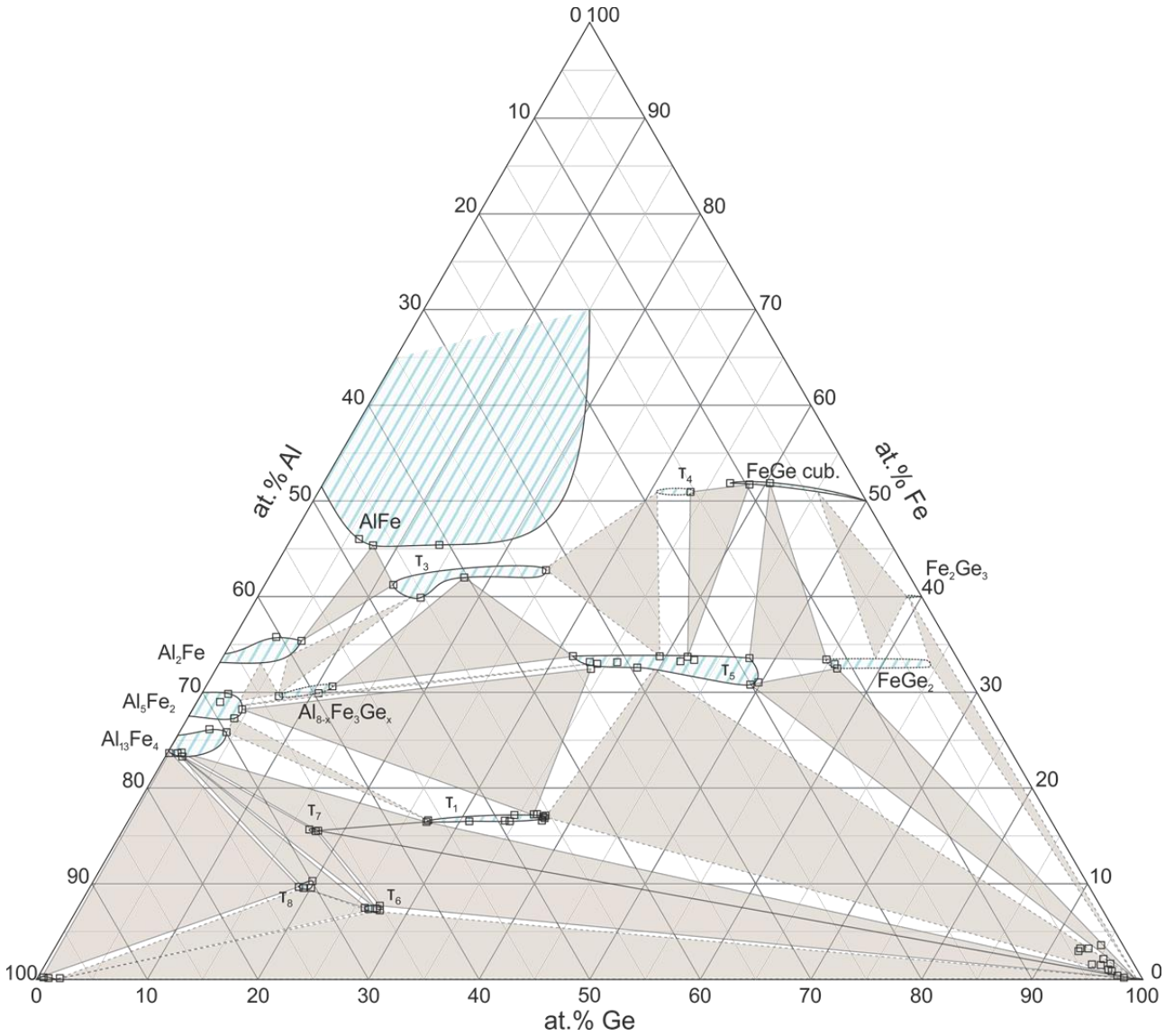

Figure 1.2.1 – Partial phase diagram of Al-Fe-Ge at 400 °C. Striped blue: singe-phase fields (18)

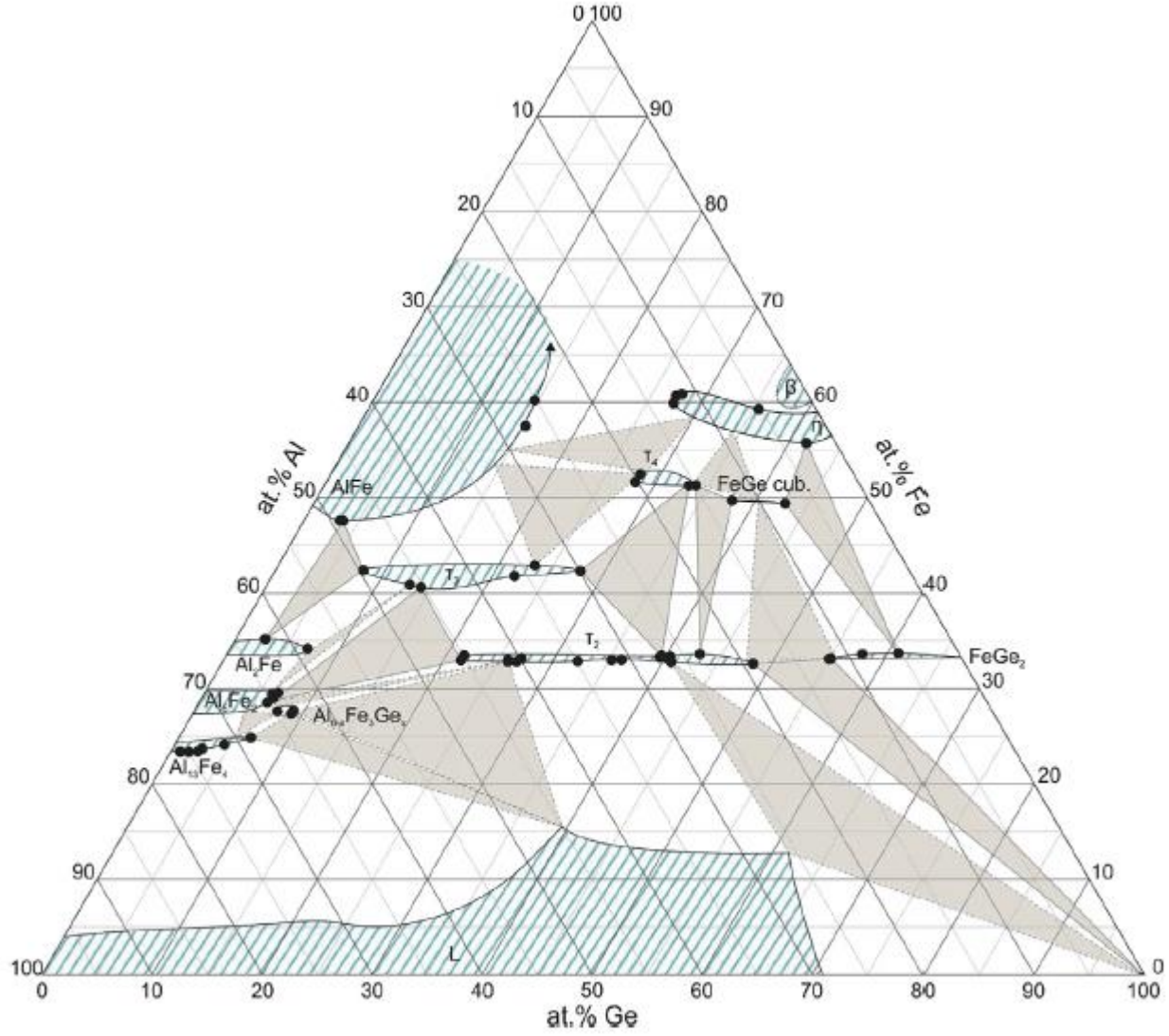

Figure 1.2.2 – Partial phase diagram of Al-Fe-Ge at 800 °C. Striped blue: singe-phase fields (19)

Table 1.2.1 – Phases in the Al-Fe-Ge system relevant to the current thesis

Phase	Structure type	Crystal system	Space group	Literature
τ1 ($Al_{3-x}FeGe_{2+x}$)	Ga_5Pd	tetragonal	*I4/mcm*	(19)
τ2 ($Al_{1+x}FeGe_{1-x}$)	$CuMg_2$	orthorhombic	*Fddd*	(19)
τ3 ($Al_7Fe_9Ge_5$)	Fe_3Ga_4	monoclinic	*C2/m*	(25)
τ4 ($Al_2Fe_6Ge_3$)	$Al_2Fe_6Ge_3$	orthorhombic	$Cmc2_1$	(25)
τ5 ($Al_{1-x}FeGe_{1+x}$)	Own, ternary La_2Sb-variant	tetragonal	*I4/mmm*	(18)
τ6 (Al67Fe7Ge26)	unknown	unknown	unknown	(18)
τ7 ($Al_{4.5-x}FeGe_{1+x}$)	own	orthorhombic	*Cmce*	(18)
τ8 (Al_7FeGe_2)	unknown	orthorhombic	*I*	(18)
Al	Cu	cubic	$Fm\bar{3}m$	(3)
Ge	C (diamond)	cubic	$Fd\bar{3}m$	(3)
$Al_{13}Fe_4$	$Al_{13}Fe_4$	monoclinic	*C2/m*	(3)

Boundary Al-Ge and Fe-Ge phases have also been shown to exert magnetostriction and magnetoelasticity (26) and are likely to form in the ternary Al-Fe-Ge system due to exothermic enthalpies of mixing that increase with Fe content (27,28). Indeed, interactions between boundary Al-Fe and Fe-Ge systems affect the formation and order of ternary phases (29). The binary phase diagrams of Al-Fe, Al-Ge and Fe-Ge are shown in Figures 1.3, 1.4 and 1.5.

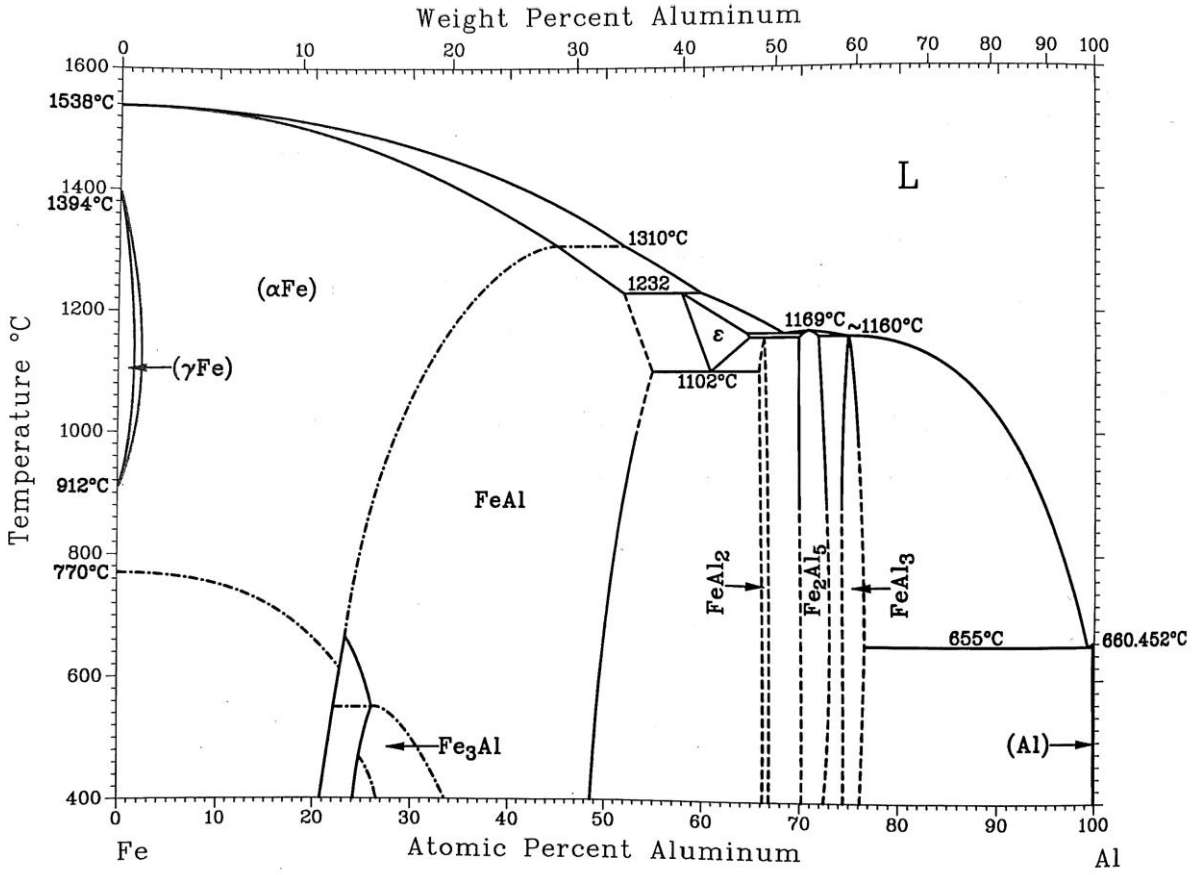

Figure 1.2.3 – Al-Fe phase diagram (3)

Six intermetallic phases and liquid are present in the Al-Fe phase diagram. In the Al-rich part, three intermetallic phases, Al_2Fe, Al_5Fe_2 and $Al_{13}Fe_4$ (noted as $FeAl_3$ in Figure 1.2.3), form at similar melting points. Al-Fe occupies a relatively large single-phase field in the Al-Fe-Ge phase diagram. For this investigation, $Al_{13}Fe_4$ is of importance, as it might be in equilibrium with $\tau 8$. $Al_{13}Fe_4$ forms from liquid at 1160 °C and takes part in the eutectic reaction at 655 °C (3).

$$L \rightleftharpoons (Al) + Al_{13}Fe_4$$

Reaction 1.2.1 –Al-Fe eutectic reaction (3)

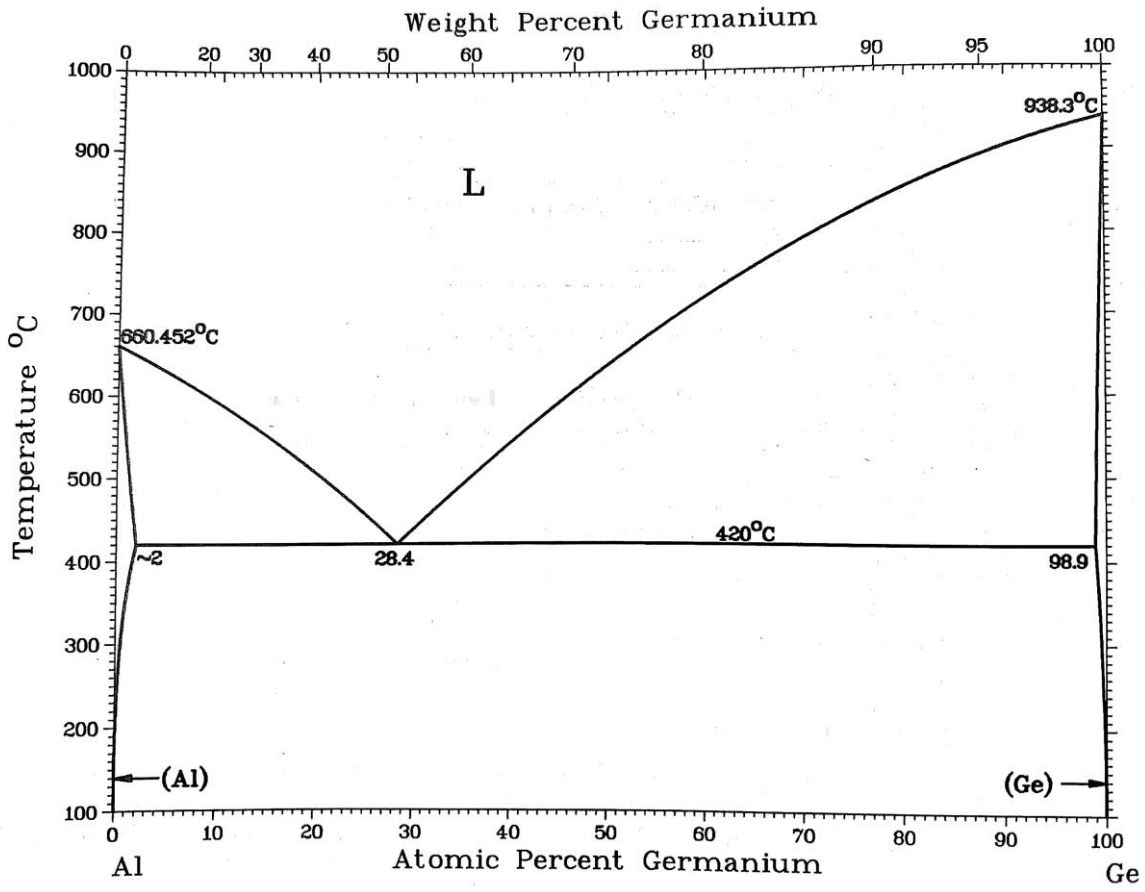

Figure 1.2.4 – Al-Ge phase diagram (3)

Two solid phases and liquid are present in the Al-Ge phase diagram. A eutectic reaction at 420 °C and 28.4 at. % Ge forms a solid mixture of Al and Ge from liquid (3).

$$L \rightleftharpoons (Al) + (Ge)$$

Reaction 1.2.2 – Al-Ge eutectic reaction (3)

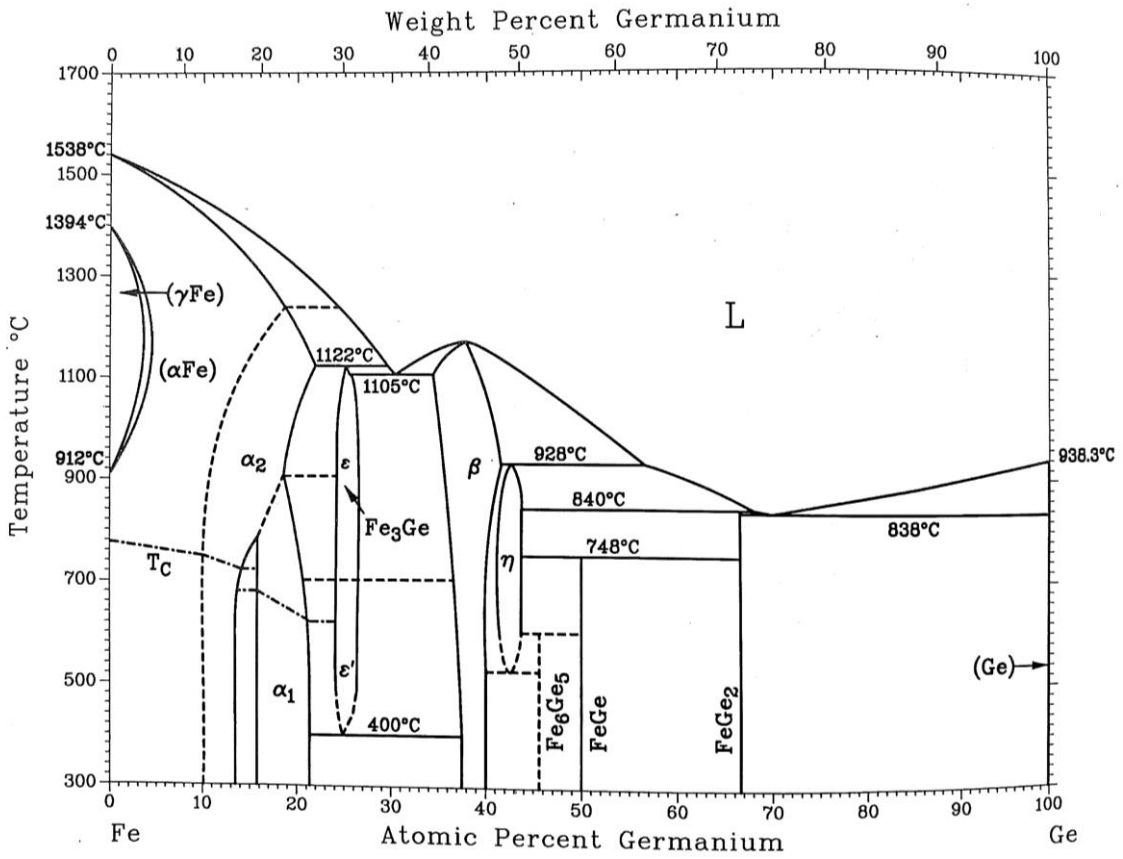

Figure 1.2.5 – Fe-Ge phase diagram (3)

Nine intermetallic phases are present in the Fe-Ge phase diagram. FeGe, $FeGe_2$, β (Fe_2Ge) and η ($Fe_{13}Ge_8$) were identified in the ternary Al-Fe-Ge system at 400 °C.

1.3. Au-Si-Ti systems

Due to the high melting temperature of Ti, soldering of Ti requires plating with another metal (30) and brazing of Ti (31) requires special conditions (32) or filler metals. Therefore, investigation of the Au-Si-Ti system could open new possibilities for soldering and brazing applications. Until now, the system Au-Si-Ti has only been investigated in a diploma thesis from 2019 (33). The Si-rich side at 340 °C was investigated and an intermetallic phase T1 with composition $Au_{10}Si_6Ti_9$ discovered and characterized. T1 is of orthorhombic structure, containing 100 atoms in the unit cell and with lattice parameters *a* = 11.666 Å, *b* = 9.6503 Å and *c* = 14.231 Å (33). There are Si_6Ti_9 clusters in the unit cell of T1 which are identical to the clusters in the binary phase Si_4Ti_5. The Si-rich side of Au-Si-Ti was also investigated at 600 °C, where T1 was also present (33). Furthermore, the Ti-rich side at 900 °C was investigated and ternary compound discovered, T2, with composition Au34 Si25 Ti42 at. % (33). The powder diffractogram of T2 was different than that of T1, yet the crystal structure could not be determined, as the phase could not be synthesized in pure (33). The partial ternary phase diagram at 900 °C is shown in Figure 1.3. Phases relevant to the current thesis are listed in Table 1.3.1.

Table 1.3.1 – Phases in the Au-Si-Ti system relevant to the current thesis

Phase	Structure type	Crystal system	Space group	Literature
$Au_{10}Si_6Ti_9$ (T1)	own	orthorhombic	*Cmce*	(33)
T2	unknown	unknown	*unknown*	(33)
Au_2Ti	$MoSi_2$	tetragonal	*I4/mmm*	(3)
Si_3Ti_5	Mn_5Si_3	hexagonal	*P63/mcm*	(3)
Si_4Ti_5	Si_4Zr_5	tetragonal	$P4_12_12$	(3)

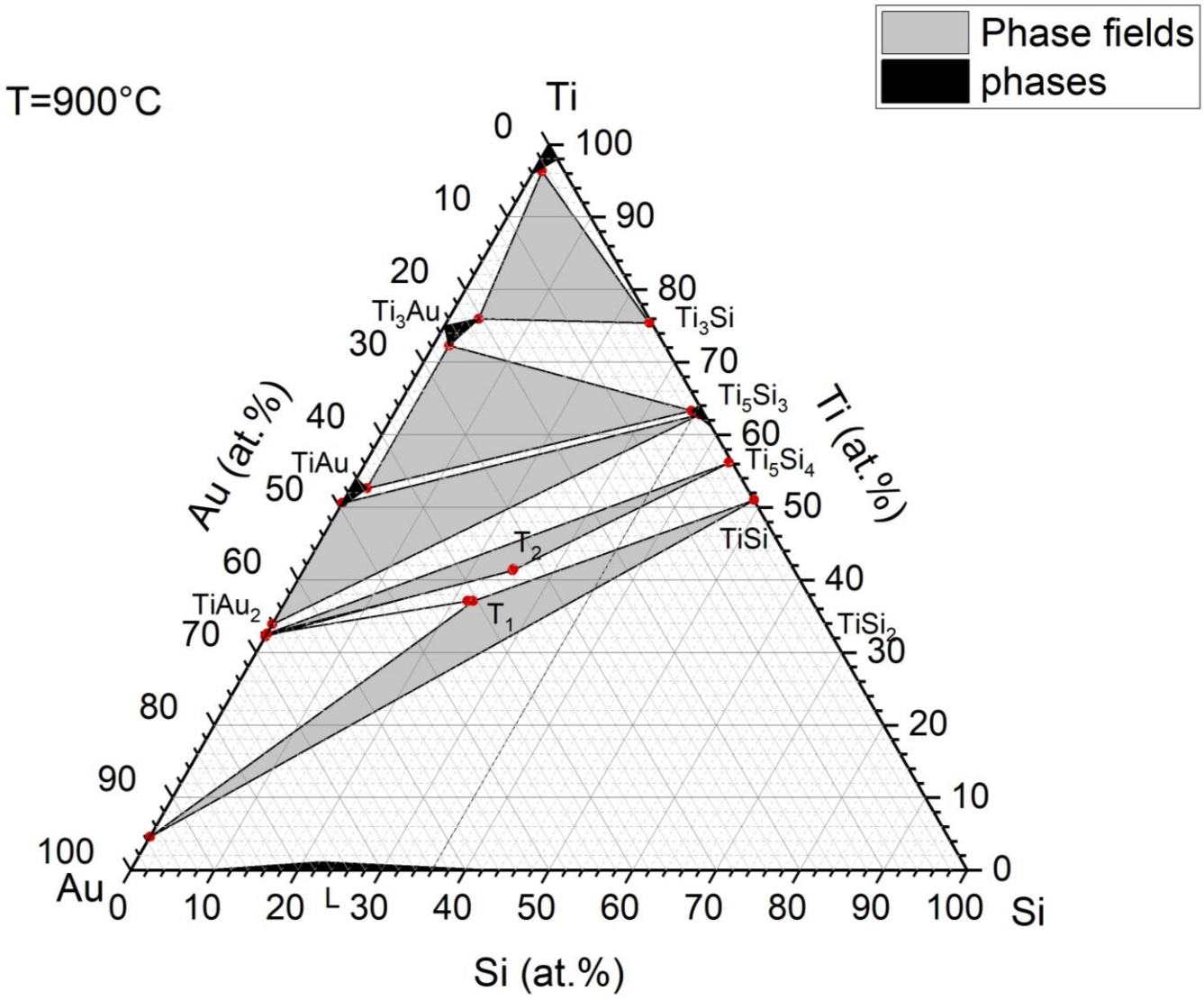

Figure 1.3.1 – Partial phase diagram of Au-Si-Ti at 900 °C (33)

At 900 °C, T1 has tie lines to TiSi and Au with corresponding adjacent three-phase fields. T2 has tie lines connecting to $AuTi_2$ and Si_4Ti_5 with corresponding adjacent three-phase fields. The tie-triangles connecting T1 and T2 have not been clarified up to now. The phase diagrams of boundary binary systems are shown in Figures 1.3.2 – 1.3.4.

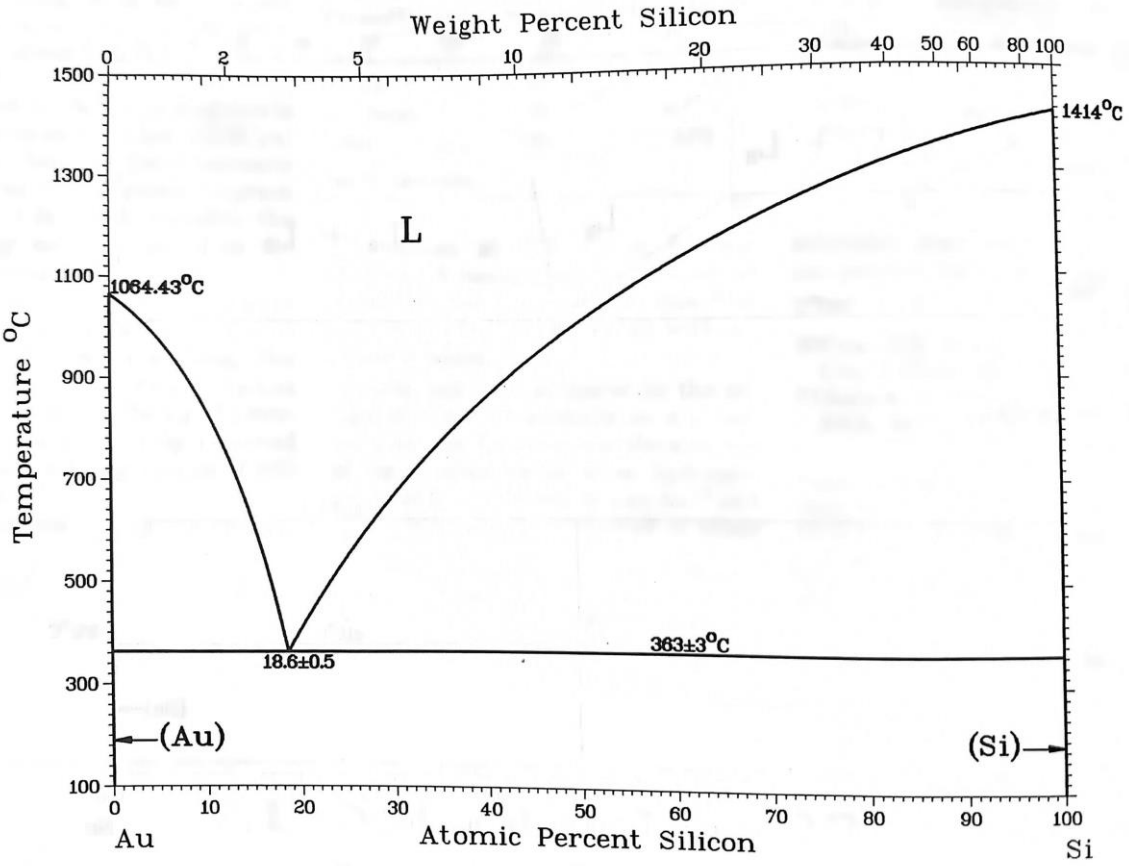

Figure 1.3.2 – Au-Si phase diagram (3)

Au-Si can be used as solder, as it has a low eutectic temperature of 363 °C at 18.6 at. % Si (34,35). The solders form strong connections (34–36) that can be used for low temperature applications (37). However, they are insufficient for electronics operated at high temperature (38). At 900 °C there are two-phase fields of Au + L and Si + L, as well as the unary phase field of L. For the current investigation, T2 in equilibrium with the ternary liquid phase could be exploited to grow larger crystals of T2 for characterization.

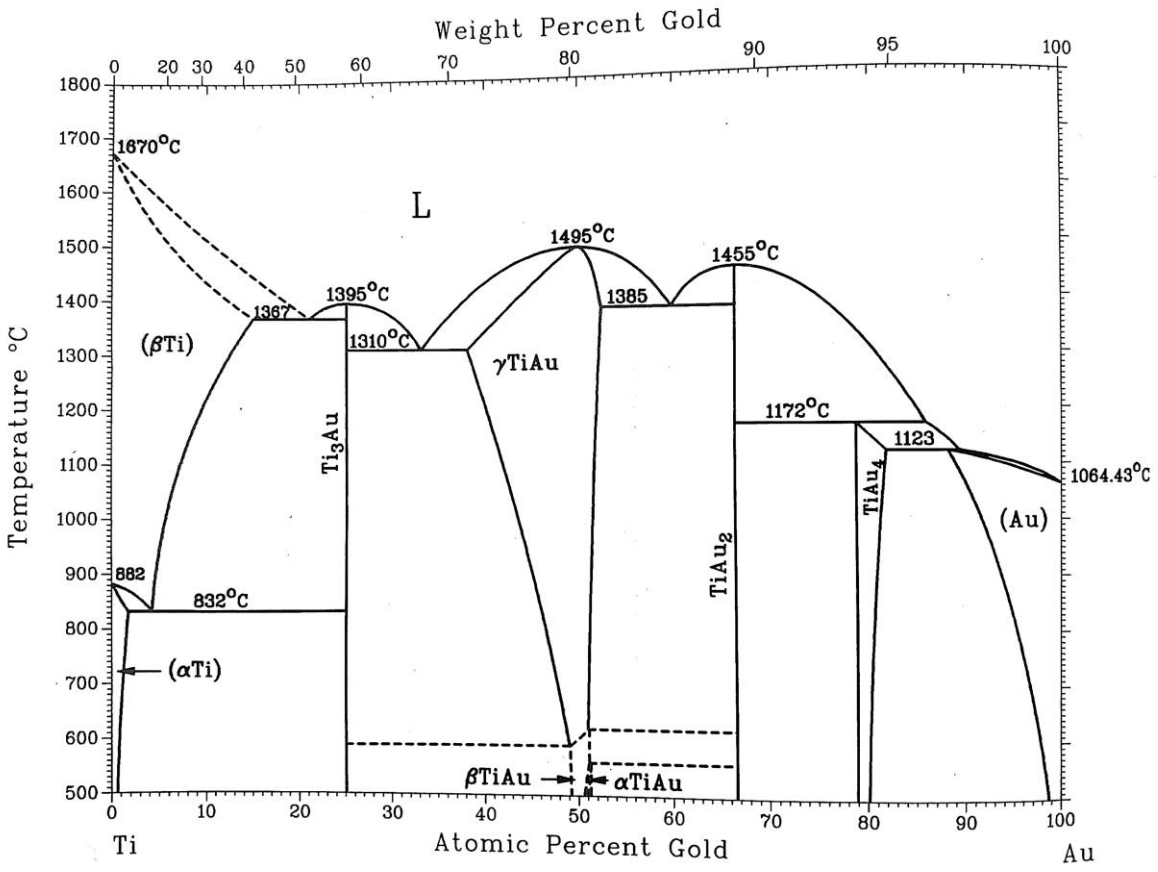

Figure 1.3.3 – Au-Ti phase diagram (3)

The eutectic reactions in the Au-Ti phase diagram are all above 900 °C. There is an eutectoid reaction at 832 °C and 4.2 at. % Ti:

$$(\beta Ti) \rightleftharpoons (\alpha Ti) + AuTi_3$$

Reaction 1.3.1 – Eutectoid reaction in Au-Ti (3)

Soldering below the (βTi) / (αTi) transition temperature leads to improved mechanical properties, such as fatigue and ductility (39). In the ternary phase diagram (Figure 1.3.1), the tie line connecting T1 to 96 at. % Au just borders the binary phase field Au and $TiAu_4$, which is present from 81 to 95 at. % Au in the binary Au-Ti phase diagram (Figure 1.3.3). Hence Au and $TiAu_4$ are likely to form when synthesizing T1.

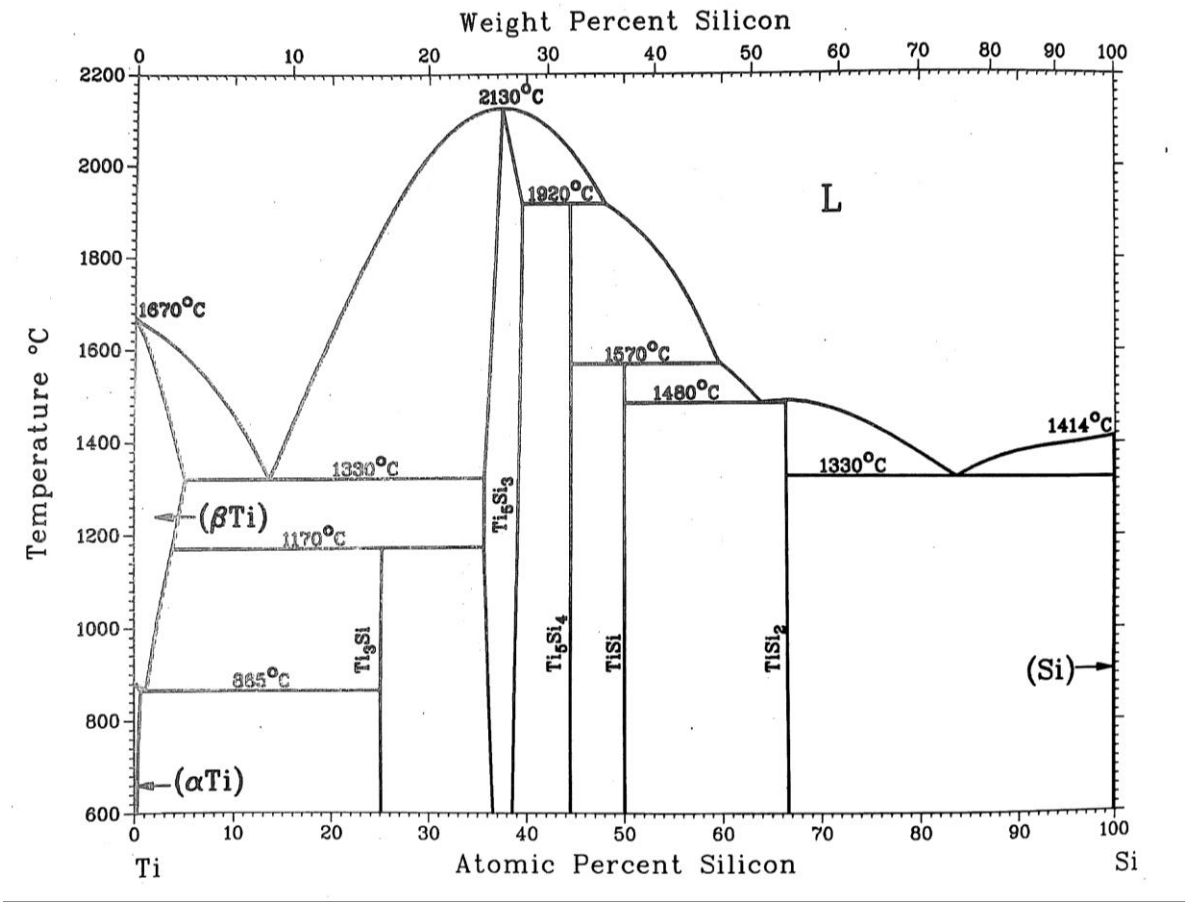

Figure 1.3.4 – Si-Ti phase diagram (3)

Similar to the Au-Ti phase diagram, all eutectic reactions are above 900 °C in the Si-Ti phase diagram. There is an eutectoid reaction at 865 °C and 1.2 at. % Si:

$$(\beta Ti) \rightleftharpoons (\alpha Ti) + SiTi_3$$

Reaction 1.3.2 – Eutectoid reaction in Si-Ti (3)

As in the Au-Ti phase diagram, the transition from (βTi) to (αTi) involves a structural change, as (βTi) is cubic with space group *Im*$\bar{3}$*m* and (αTi) is hexagonal with space group *P63*/*mmc* (3).

1.4. Au-Ni-Sn systems

The first ternary intermetallic structure of Au-Ni-Sn was reported in 1962 (40). Lattice spacings of the binary hexagonal Au-Sn ζ structure with added nickel were examined and a hexagonal structure of Au 0.825 Ni 0.045 Sn 0.13 determined. In 1995 the structure of the ternary compound $AuNi_2Sn_4$ was determined as trigonal with space group $R\bar{3}m$ and lattice parameters a = 42.26 Å and c = 26.57 Å (41). In 2005 the structure of $AuNiSn_2$ was determined as trigonal with space group $P\bar{3}m1$ and lattice parameters a = 4.12 Å and c = 5.29 Å (42). The ternary phase diagram has been explored and a Ni_3Sn_2 superstructure discovered and is characterized as a vacancy variant of the hexagonal NiAs–Ni_2In-type (43). Superstructures of NiAs–Ni_2In-types are well documented (44), yet further details on the Ni_3Sn_2 superstructure were not published (43). A $(Au,Ni)_3Sn_2$ superstructure was detected in our internal lab course and a model of the crystal structure created by Hans Flandorfer and Klaus Richter (unpublished results) (45). However, this model could not be verified, as the samples containing the superstructure were not pure. Phases relevant to the current thesis are listed in Table 1.4.1. The partial Au-Ni-Sn phase diagram is shown in Figure 1.4.1 and the binary phase diagrams of Au-Ni, Au-Sn and Ni-Sn are shown in Figures 1.4.2 – 1.4.4 respectively. Three single-phase fields, (Au,Ni)Sn, $AuNiSn_2$ and $(Au,Ni)_3Sn_2$, are present in the ternary phase diagram of Au-Ni-Sn. Phases ζ, AuSn, Ni_3Sn_4, Ni_3Sn_2 and Ni_3Sn are present at the binary borders.

Table 1.4.1 – Phases in the Au-Ni-Sn system relevant to the current thesis

Phase	Structure type	Crystal system	Space group	Literature
$AuNiSn_2$	$AuNiSn_2$	trigonal	*$P\bar{3}m1$*	(42)
AuSn (δ) / (Au,Ni)Sn	NiAs	hexagonal	*P63/mmc*	(3)
ζ	Mg	hexagonal	*P63/mmc*	(3)
Ni_3Sn	Mg_3Cd	hexagonal	*P63/mmc*	(46)
Ni_3Sn_2 (HT) / $(Au,Ni)_3Sn_2$	Ni_2In	hexagonal	*P63/mmc*	(47)
Ni_3Sn_4	Ni_3Sn_4	monoclinic	*C 1 2/m 1*	(48)
$(Au,Ni)_3Sn_2$ superstructure	unknown	unknown	*unknown*	-

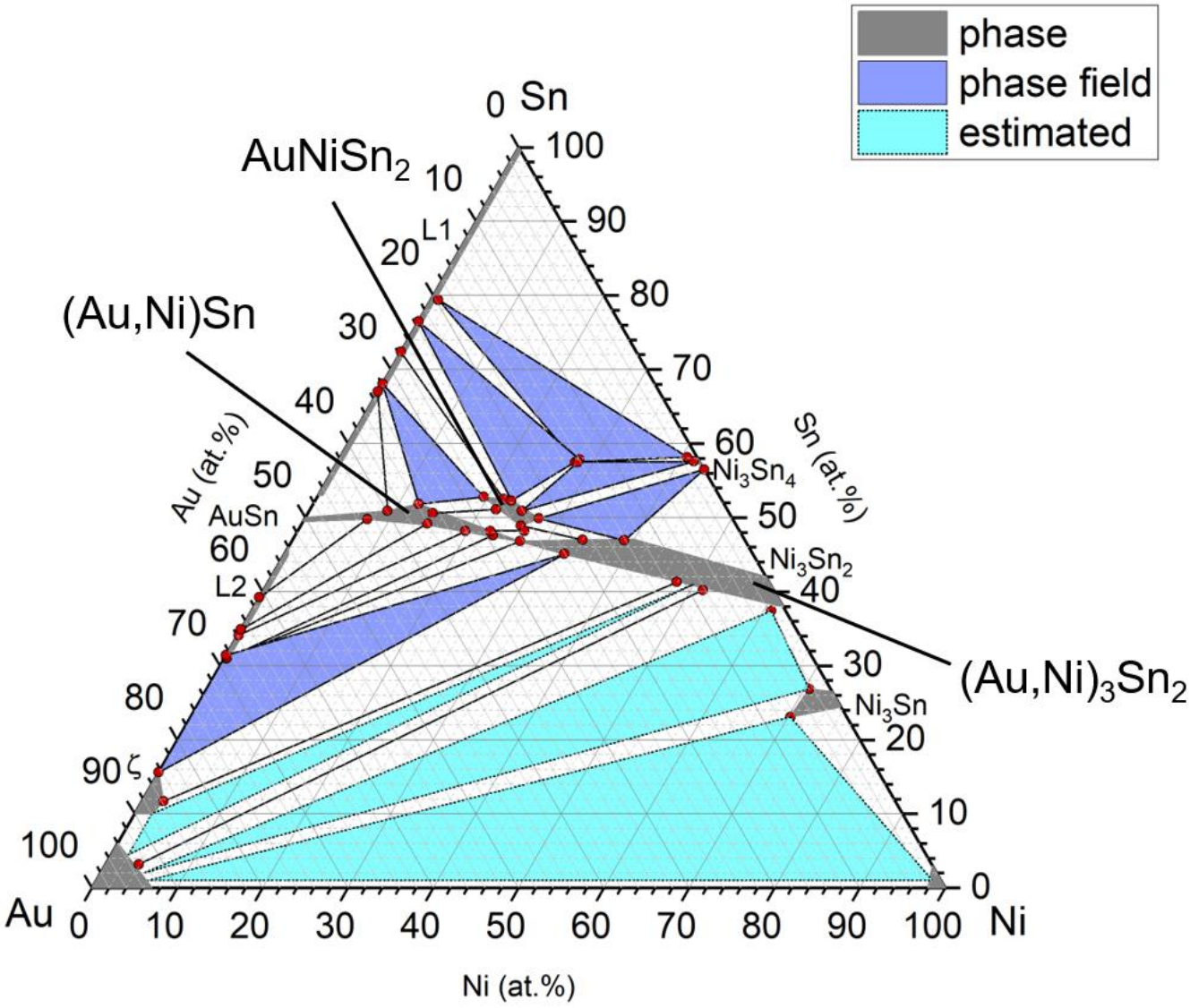

Figure 1.4.1 – Partial phase diagram of Au-Ni-Sn at 400 °C (45)

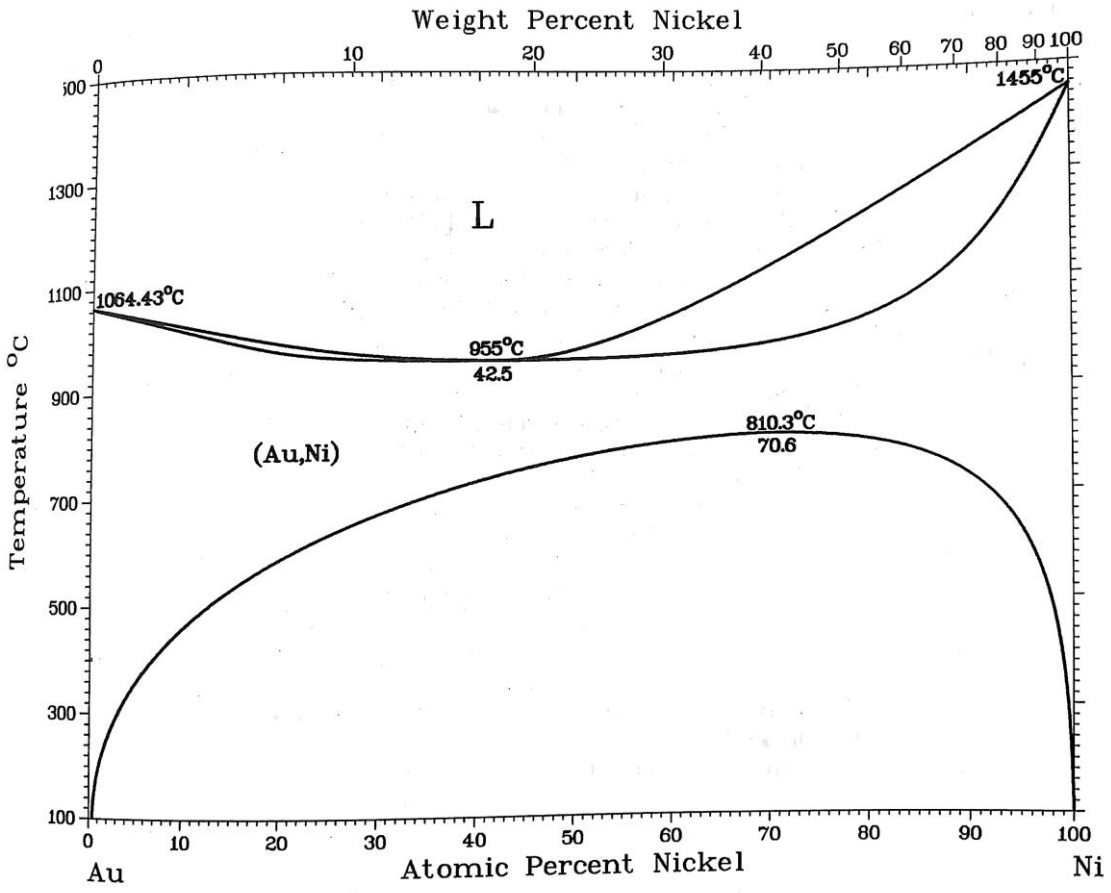

Figure 1.4.2 – Au-Ni phase diagram (3)

In the Au-Ni phase diagram there is the solid solution (Au,Ni) with a large miscibility gap, which is continuous between 810.3 °C to 942.5 °C.

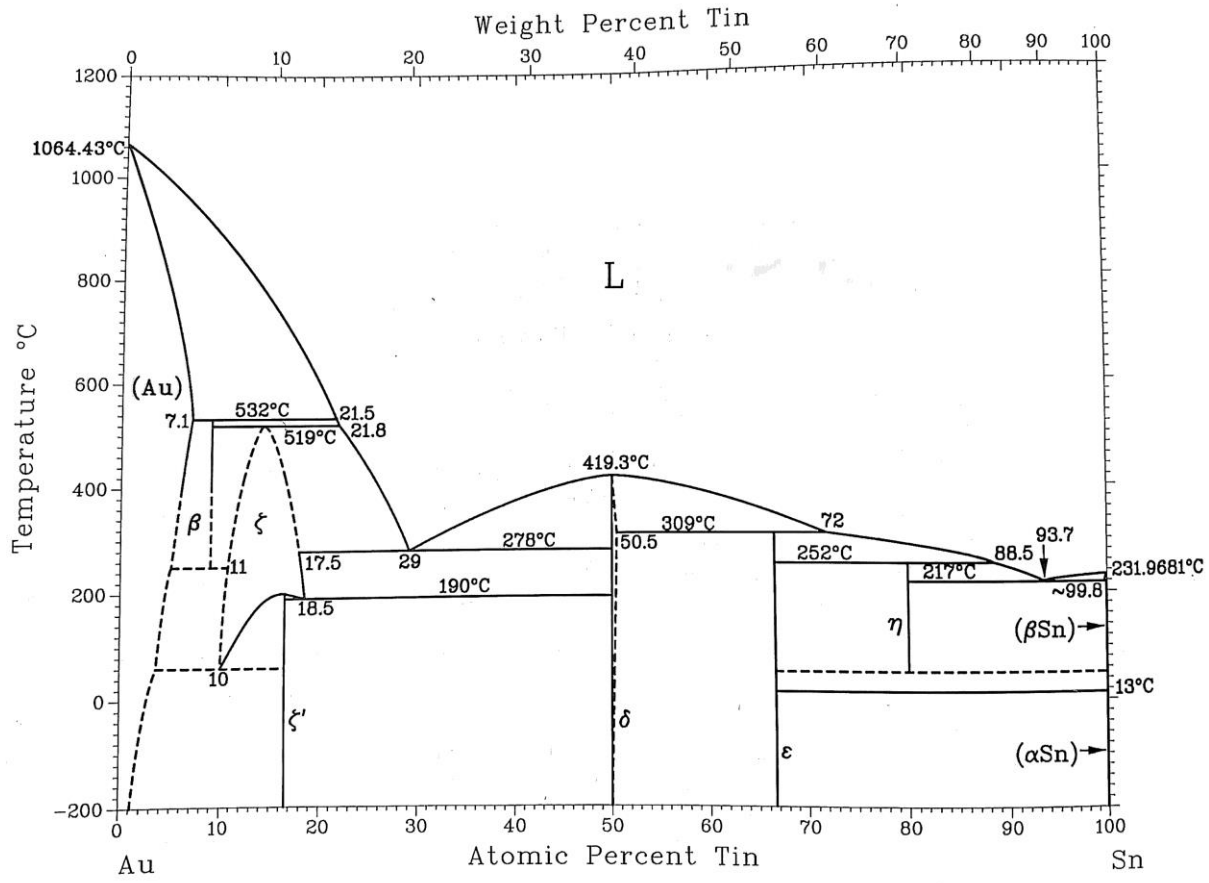

Figure 1.4.3 – Au-Sn phase diagram (3)

There are two peritectic reactions at 532 °C and 519 °C that form β ($Au_{10}Sn$) and ζ respectively. In a eutectic reaction at 232 °C liquid reacts to form η ($AuSn_4$) and (βSn). Furthermore, the eutectic reaction at 278 °C is often exploited for soldering applications (49,50):

$$L \rightleftharpoons \zeta + \delta$$

Reaction 1.4.1 – Eutectic reaction in Au-Sn at 278 °C (3)

Intermetallic phases ζ, δ (AuSn), ε ($AuSn_2$) and η have all been detected in soldering joints (49,50). Whilst ε and η are stoichiometric phases, ζ and δ have a composition range of 10 – 18.5 at. % Sn and 50 to 50.5 at. % Sn respectively. Phases ζ and δ also have a solubility for Ni of 1 at. % for ζ and more than 20 at. % for δ (49).

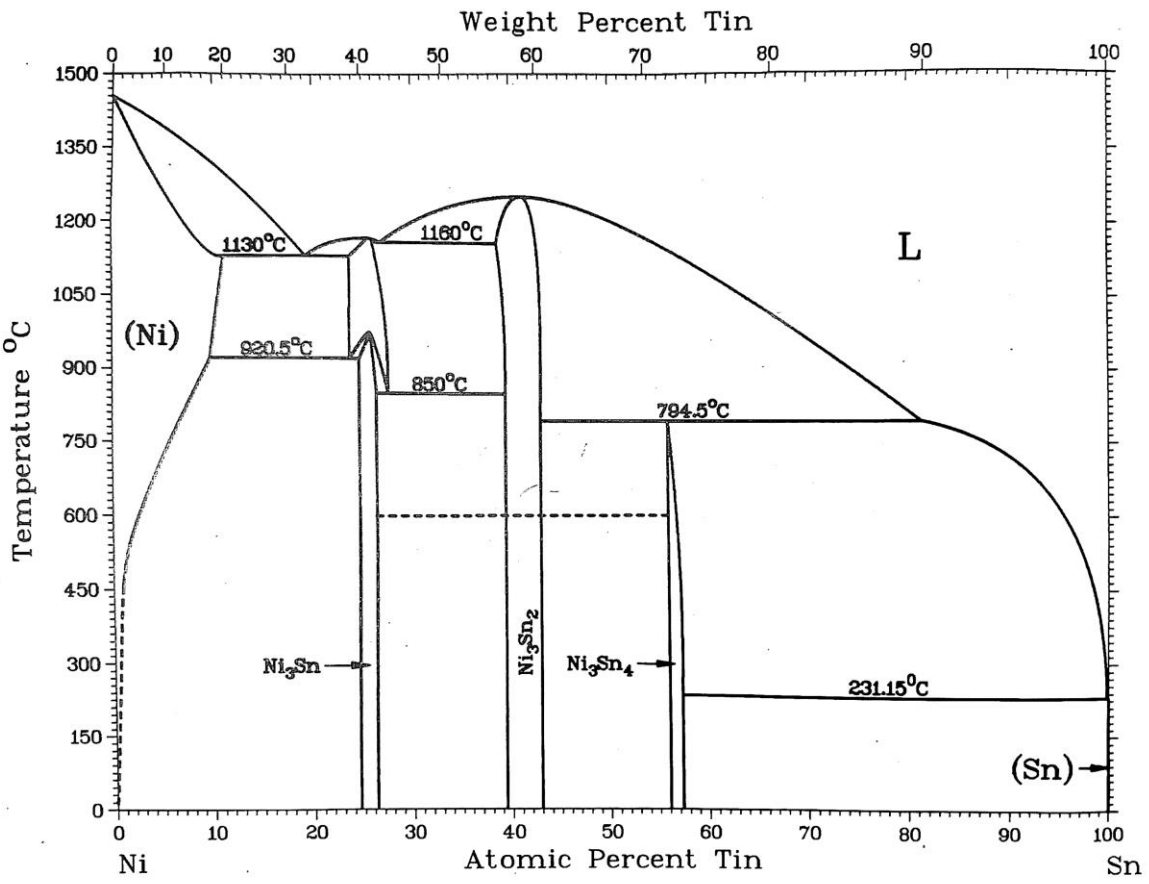

Figure 1.4.4 – Ni-Sn phase diagram (3)

There are eutectic reactions at 1160 °C, 1130 °C and 231.15 °C and a peritectic reaction at 794.5 °C. In eutectoid reactions at 920.5 °C and 850 °C, hexagonal Ni_3Sn_2 (HT) reacts to form orthorhombic Ni_3Sn_2 (LT) with space group *Pnma* (47). Furthermore, Ni_3Sn_2 (HT) shows solubility for Au and forms $(Au,Ni)_3Sn_2$ (51).

1.5. Experimental Methods

1.5.1. Powder X-ray diffraction

When electromagnetic waves hit atoms, part of the incoming intensity is scattered as spherical waves. According to Bragg's law, a constructive interference can occur if the angle between the incoming electromagnetic wave and the plane, θ, is a multiple of the wavelength, λ:

$$2dsin\theta = n\lambda$$

Equation 1.5.1.1 – Bragg's law

where d is the spacing between adjacent lattice planes. The wavelengths of X-rays range from 10 nm to 0.01 nm, which covers the size of bond lengths in crystals of 1-3 Å (0.1-0.3 nm). Therefore, when exposing crystals to X-rays, the constructive interference can provide information about the crystal structure, such as unit cell parameters and atomic positions. A method of analysis is powder X-ray diffraction (P-XRD), in which X-rays irradiate a polycrystalline powder sample and are reflected according to Bragg's law. The polycrystalline powder statistically exhibits all possible crystal orientations. Furthermore, the sample is rotated during analysis, which increases the number of orientations and enables the collection of a diffraction pattern at all angles. The powdered sample is placed in a diffractometer. The angle between the incoming X-ray and the sample is half the angle to the detector and is therefore noted as 2θ. This geometry is known as the Bragg-Brentano geometry. During analysis, tube and detector are rotated and a Bragg-Brentano θ-θ geometry can be used, where the detector and the source rotate around the sample at the same speed and the angle between the incoming X-ray and sample is θ. Compared to SC-XRD, not diffraction points, but diffraction rings are collected on a reflection plane. When Bragg's law is met, the intensity of rings emitted at specific angles are picked up by the detector and recorded to create a characteristic diffraction pattern. The diffractogram is a plot depicting intensity (y-axis) vs 2θ (x-axis) and can be used as a fingerprint to identify crystals. Powder-XRD can be used to qualitatively and semi-

quantitively analyse multiple phases in the same sample. However, crystals with low symmetry or large unit cells generate complex diffractograms that are difficult to evaluate. Furthermore, determination of unknown structures is difficult due to overlapping reflections. The Rietveld method is used to refine known and unknown structures, although it is necessary to have crystallographic information about the unknown structure, such as space group and unit cell parameters. With the Rietveld method a theoretical diffraction pattern is modelled and the R-factor represents the agreement between the crystallographic model and the diffractogram:

$$R_{wp} = \sqrt{\frac{\sum_{i=1}^{N} w_i \left(y_{obs,i} - y_{calc,i}(\mathbf{p})\right)^2}{\sum_{i=1}^{N} w_i y_{obs,i}^2}}$$

Equation 1.5.1.2 – R-factor for Rietveld refinement

where *y* is the intensity, *w* the weight factor and **p** the parameters vector to calculate the intensity by the refined parameters. The lower the R-factor, the better the agreement between the collected data and the crystallographic model (52).

1.5.2. Single-crystal X-ray diffraction

In single-crystal X-ray diffraction (SC-XRD), a single crystal is exposed to a monochromatic X-ray beam, which is diffracted by the crystal according to the Laue equations. A typical X-ray source is copper, which produces K_α and K_β emission lines. The wavelengths of emission lines are specific for the atomic composition of the source. For example, the K_α and K_β wavelengths of copper are 1.54 Å and 1.39 Å. For molybdenum the K_α and K_β wavelengths are 0.71 Å and 0.63 Å. To dissipate heat, the X-ray sources are cooled. By rotating the anode in so-called rotating-anode sources, additional cooling is achieved which can produce higher intensities. Before the X-rays strikes the crystal, they are filtered and collimated. This removes unwanted emission lines, such as the K_β emission line in copper, and aligns the waves to produce a monochromatic wave to irradiate the crystal. Filtering is usually achieved by placing

an element one atomic number lower than the source material in front of the path. For example, nickel has an absorption cut-off at 1.49 Å and when placed in front of copper, can absorb the K_β emission. Collimation is achieved by placing a collimator or curved mirrors into the path of the X-rays. From the substance to be analysed a crystal is then selected and placed on a goniometer. It is essential that the crystal is pure and of sufficient size. Even then, cracks and twinning can impede analyses. The monochromatic X-ray irradiates the crystal and the constructive waves are diffracted as discrete reflection points on a reflection plane. The goniometer slowly rotates the crystal so that the diffraction patterns of every crystal orientation are obtained. The data are collected and the structure modelled from the relative intensities of the peak using computational methods. As in P-XRD, the R-factor is used to compare the crystallographic model to the experimental data (52).

$$R = \frac{\sum\left||F_{obs}| - |F_{calc}|\right|}{\sum|F_{obs}|}$$

Equation 1.5.2.1 – R-factor for SC-XRD

where F is the structure factor, which is related to the peak intensities by

$$|F_{hkl}|^2 \propto I_{hkl}$$

Equation 1.5.2.2 – Structure factor for SC-XRD

1.5.3. Scanning electron microscopy

Scanning electron microscopy (SEM) uses an electron beam to produce magnified images of up to 1,000,000 times magnification. In an electron gun a cathode, usually of tungsten, is heated to produce electrons accelerated in an electric field and collimated. The collimated electron beam is focused by condenser lenses to a spot of 1 – 10 nm on the sample. The sample and aperture are under high vacuum, although low vacuum analysis is also possible for wet or non-conductive samples, which is known as environmental SEM. Scanning coils placed orthogonally to the electron

beam deflect the beam in the x- and y-directions, so that the beam spot is raster scanned over the sample. Different detectors collect the intensity of emitted signals. Commonly analysed emitted signals are secondary electrons, backscattered electrons and X-rays. Secondary electrons are emitted from atomic valence or conduction bands by inelastic scattering. A positively charged grid on the secondary-electron detector attracts secondary electrons, where they are accelerated towards a scintillator followed by a photomultiplier. As secondary electrons are low energy and originate from surface or near-surface regions, a topographic image according to the signal intensities is created. Each spot contributes to the generation of a rectangular image. The magnification can be increased by reducing the raster size, which is controlled by the scanning coils. Backscattered electrons are high-energy electrons elastically reflected from the surface. They originate from the interaction of the electron beam with atoms. A scintillator or semiconductor-type detector is placed concentrically around the incoming electron beam above the sample to collect the backscattered electrons. The intensity of backscattered electrons positively correlates with the atomic number. Therefore, the intensity of backscattered electrons can be used to map the chemical composition of the sample, where elements with higher atomic number will appear brighter due to the larger nucleus. Furthermore, backscattered electrons can also be used to obtain crystallographic information in a method called electron backscatter diffraction. X-rays are generated when the electron beam strikes the sample and electrons from inner orbitals are removed, leaving an unoccupied state. When the unoccupied state is filled by another electron in a higher orbital, characteristic X-rays, such as K_α and K_β lines, are emitted resulting from the energy difference between the orbitals. An X-ray detector inside the sample holder can collect these X-rays and be used to determine the elemental composition of the sample. Wavelength dispersive spectrometers (WDS) collect X-rays regarding their wavelength and energy dispersive spectrometers (EDS) collect X-rays regarding their energy. WDS analyse one specific wavelength and have a high resolution, good reproducibility and a low detection limit. EDS allows for fast elemental analysis of the entire periodic table (52).

1.5.4. Optical microscopy

In optical microscopy, visible light passes through condenser lenses and is reflected off a sample through an objective into an eyepiece or camera. In bright-field microscopy, an image is created depending on the attenuation of light in the sample. The reflected waves generate a magnified image of color and contrast. The amount of magnification is determined by the objective and the eyepiece, where usually depth of field decreases with increasing magnification. In dark-field microscopy, a phase ring blocks directly incoming light and directs light away from the sample. Light directed away from the sample passes through a condenser lens that focuses the beams onto the sample at an angle. When the light reaches the sample, it is scattered, reflected or transmitted, but only scattered light reaches the objective. The resulting image is usually a negative of the bright-field image. Compared to bright-field microscopy, the contrast is increased and objects smaller than the microscope resolution can be observed. In differential interreference contrast microscopy (DIC) light polarized at 45° passes through a Wollaston prism and is split into two orthogonally polarized beams, which are focused onto the sample by a condenser lens. The two beams are reflected and interfere based on the topography and refractive index of the sample. A 3D image is created. In cross-polarized light microscopy, cross-polarized light is focused onto the sample and the reflection generates an image that can be used to see isotropic, anisotropic and twinned crystals. Isotropic crystals reflect polarized light in the same orientation and no change of color is observed when rotating the sample. Anisotropic crystals reflect polarized light as two parallel polarized beams that can constructively or destructively interfere with each other. When the sample is turned, the interreference between the two parallel beams is seen as a color change in the image, showing maximal constructive or destructive interference every 90 °C. Twinned crystals have separate domains with distinct reflections of polarized light, which is observed as different colors in the image (52).

1.5.5. Differential thermal analysis

In differential thermal analysis (DTA), a sample is heated and cooled in an inert environment in reference to an inert reference material. Both sample and reference

are connected to a thermocouple. Exothermic and endothermic processes during heating and cooling are recorded, which provide information about melting points, crystallization points, sublimation points, hysteresis, stability of phases, formation of phases, transformation of phases, as well as invariant and non-invariant reactions. DTA is therefore an invaluable tool for the study and exploration of phase diagrams (53).

2. Experimental

2.1. Al-Fe-Ge

2.1.1. Sample compositions and annealing parameters

Aluminium (Al slug, 3.175 mm x 6.35 mm, 99.999 %, Alfa Aesar), iron (Fe sheet, 99.9 %, vacuum cast) and germanium (Ge pieces, 3 – 9 mm, 99.999 %, Alfa Aesar) were weighed in on a Sartorius research R200D weighing scale according to the compositions listed in Table 2.1.1.1 with an accuracy of ± 0.5 mg. Samples 1a, 1b, 3 and 4 correspond to the composition of τ6 and samples 2, 5 and 6 correspond to the composition of τ8. Sample 7 corresponds to τ8 in equilibrium with liquid in order to grow larger crystals. Samples Tau6.1, Tau6.2, Tau8.1 and Tau8.2 were prepared and analysed by Martin Marker (54).

Table 2.1.1.1 – Al-Fe-Ge samples

Sample	Composition (at. %)			Annealing temperature (°C)	Annealing time (days)
	Al	Fe	Ge		
Tau6.1	68.0	5.0	27.0	470	
Tau6.2	68.0	5.0	27.0	470	
Tau8.1	70.7	6.7	22.6	470	
Tau8.2	70.7	6.7	22.6	470	
1a	66.0	7.5	26.5	500	14
1b	66.0	7.5	26.5	500	14
2	71.0	9.5	19.5	500	14
3	65.6	7.4	27.0	520	14
4	66.4	7.2	26.4	520	14
5	71.6	9.7	18.7	520	14
6	71.2	9.4	19.4	520	14
7	73.3	6.7	20.0	520	14

Samples were molten three times under inert argon atmosphere (Ar Messer, Ar 5.0, >99.999 vol.%) in an arc furnace (Johanna Otto GmbH, MAM1) in the presence of a zirconium getter. The homogenized alloys were each placed separately in aluminium oxide crucibles and sealed in an evacuated quartz glass tube (9×10^{-6} bar). The aluminium oxide crucible was utilized to prevent the sample from reacting with quartz during annealing. Samples were annealed in a furnace (Nabertherm) at the designated temperature. Annealing was completed after 14 days for samples 1a – 7 and 18 days for samples 8-9 and the equilibrium state preserved by quenching the samples in cold water.

2.1.2. Embedding

Samples were crushed using a pestle and mortar and pieces selected for embedding in an electrically conducting resin (phenolic hot mounting resin with carbon filler, Struers, PolyFast). Embedding was achieved by heating pieces of sample with resin in a mounting press (Struers, LaboPress-1) at 180 °C and 20 kN for five and a half minutes, followed by cooling for three minutes.

2.1.3. Grinding and polishing

Embedded samples were fixed on a grinding and polishing system (Struers, LaboPol - 6). Samples were ground sequentially with 30 µm, 18 µm and 10 µm grain size SiC abrasive paper. Samples were polished sequentially with 1 µm and 0.3 µm grain size aluminium oxide powder (Buehler, Micropolish II).

2.1.4. Single-crystal X-ray diffraction

A single crystal of diameter 65 µm was selected with a stereo microscope (Zeiss Stemi 2000-C), attached to a glass capillary and mounted in a four-cycle single crystal diffractometer in kappa geometry (Nonius Kappa CCD). Single-crystals were irradiated by a collimated and monochrome Mo-K_α beam. 2θ reflections were detected

on a charge-coupled device detector and analysed with SHELX-97 software to determine the structure.

2.1.5. Powder X-ray diffraction

Samples were crushed to a fine powder with a pestle and mortar, distributed evenly on a petrolatum-covered Si single crystal sample holder and placed in a diffractometer (Bruker, D8 ADVANCE). Samples were irradiated with a monochrome Cu-K_α beam in Bragg-Brentano θ-2θ geometry for 2 hours at 40 kV / 40 mA.. Diffraction intensities were detected by an energy-dispersive detection system (Lynxeye). Diffraction patterns and Rietveld refinements were analyzed with Topas software (Bruker, Topas 7).

2.1.6. Scanning electron microscopy

Resin-embedded samples were placed and evacuated in the sample chamber of an environmental scanning electron microscope (Zeiss Supra 55 VP). Detection of backscattered electrons at different magnifications was used to create an image corresponding to the atomic number of phases. The atomic composition of phases was determined by irradiation with an electron beam (20 kV, 10 nA) and emitted lines detected by an EDS detector.

2.1.7. Optical microscopy

Resin-embedded samples were placed in the sample holder of an optical microscope (Zeiss, Axiotech 100) and images taken in bright-field and cross-polarized light mode.

2.1.8. Differential thermal analysis

In order to determine the melting points of $\tau 6$ and $\tau 8$, DTA of previously and newly prepared samples was carried out. For this, approximately 150 mg of sample were placed in an aluminium oxide crucible and heated for three cycles in an inert atmosphere (Argon, 20 ml / min) at a heating rate of 5 K / min in comparison to an inert silicon reference standard. The minimum and maximum temperature of the cycles for the measured samples is given in Table 2.1.8.1.

Table 2.1.8.1 - Minimum and maximum temperature of Al-Fe-Ge DTA cycles

Sample	T_{min} (° C)	T_{max} (° C)
Tau6.1	380	850
Tau6.2	360	850
Tau8.1	350	850
Tau8.2	350	850
AlFeGe 1a	360	850
AlFeGe 1b	360	850
AlFeGe 2	360	850

2.2. Au-Si-Ti

2.2.1. Sample compositions and annealing parameters

Gold (99,99 %, Ögussa), silicon (99,999 %, Alfa Aesar) and titanium (99,7 %, Alfa Aesar) were weighed in on a Sartorius research R200D weighing scale according to the compositions listed in Table 2.2.1.1 with an accuracy of ± 0.5 mg. All samples correspond to the composition of T2.

Table 2.2.1.1 – Au-Si-Ti samples

Sample	Composition (at. %)			Annealing temperature (°C)	Annealing time (days)
	Au	Si	Ti		
1a	35.0	24.5	40.5	900	9
1b	35.0	24.5	40.5	1000	9
1c	35.0	24.5	40.5	1100	9
3	33.0	26.0	41.0	1100	12
5	33.5	25.1	41.4	1100	14
6	33.2	25.3	41.5	1100	14

Samples were molten three times under inert argon atmosphere (Ar Messer, Ar 5.0, >99.999 vol.%) in an arc furnace (Johanna Otto GmbH, MAM1) in the presence of a zirconium getter. Each homogenized alloy was then wrapped in molybdenum foil and sealed in an evacuated quartz glass tube (9×10^{-6} bar), except for sample 6, which was placed in an aluminium oxide crucible before evacuation. Molybdenum foil and the aluminium oxide crucible were utilized to prevent reaction of the sample with quartz during annealing. Samples were then annealed in a furnace (Nabertherm) at the designated temperature. After annealing was completed, the equilibrium state was preserved by quenching the samples in cold water.

2.2.2. Embedding, grinding, polishing, SC-XRD, P-XRD, SEM, optical microscopy

Embedding, grinding, polishing, SC-XRD, P-XRD, SEM and optical microscopy were carried out as with Al-Fe-Ge. Crystals of dimensions 65 μm and 75 μm were used for SC-XRD.

2.2.3. Differential thermal analysis

In order to determine the melting point of T2, DTA of a newly prepared sample containing T2, AuSiTi 1a, was carried out. For this, approximately 150 mg of sample was placed in an aluminium oxide crucible and heated for three cycles in an inert atmosphere (Argon, 20 ml / min) at a heating rate of 5 K / min in comparison to an inert silicon reference standard. The minimum and maximum temperature of the cycle is given in Table 2.1.3.1.

Table 2.2.3.1 - Minimum and maximum temperature of Au-Si-Ti DTA cycles

Sample	T_{min} (° C)	T_{max} (° C)
AuSiTi 1a	900	1440

2.3. Au-Ni-Sn

2.3.1. Sample compositions and annealing parameters

Gold (99,99 %, Ögussa), nickel (Advent research, 99.99 %) and tin (Sn granulate, 99.999 %, smart elements) were weighed in on a Sartorius research R200D weighing scale according to the compositions listed in Table 2.3.1.1 with an accuracy of ± 0.5 mg. Positions of samples in the Au-Ni-Sn phase diagram are shown in Figure 2.3.1.1.

Table 2.3.1.1 – Au-Ni-Sn samples

Sample	Composition (at. %)			Annealing temperature (°C)	Annealing time (days)
	Au	Ni	Sn		
10	21.0	34.5	44.5	400	14
11	18.0	38.5	43.5	400	14
12	14.0	43.5	42.5	400	14
13	28.0	32.0	40.0	550	14
14	24.0	38.0	38.0	550	14
15	9.5	47.5	43.0	550	16
20	5.5	54.5	40.0	550	16

Samples were molten three times under inert argon atmosphere (Ar Messer, Ar 5.0, >99.999 vol.%) in an arc furnace (Johanna Otto GmbH, MAM1) in the presence of a zirconium getter. After melting, samples 10 - 12 and 15-20 were crushed into a fine powder and pressed into pellets with a hydraulic press (Larzep, EC10.13) at 20 kN. With powder pellets more homogenous equilibration is attained during annealing, albeit compromising growth of large crystals. Each sample was sealed in an evacuated quartz glass tube (9×10^{-6} bar). Samples were then annealed in a furnace (Nabertherm) at the designated temperature. After annealing was completed, the equilibrium state was preserved by quenching the samples in cold water.

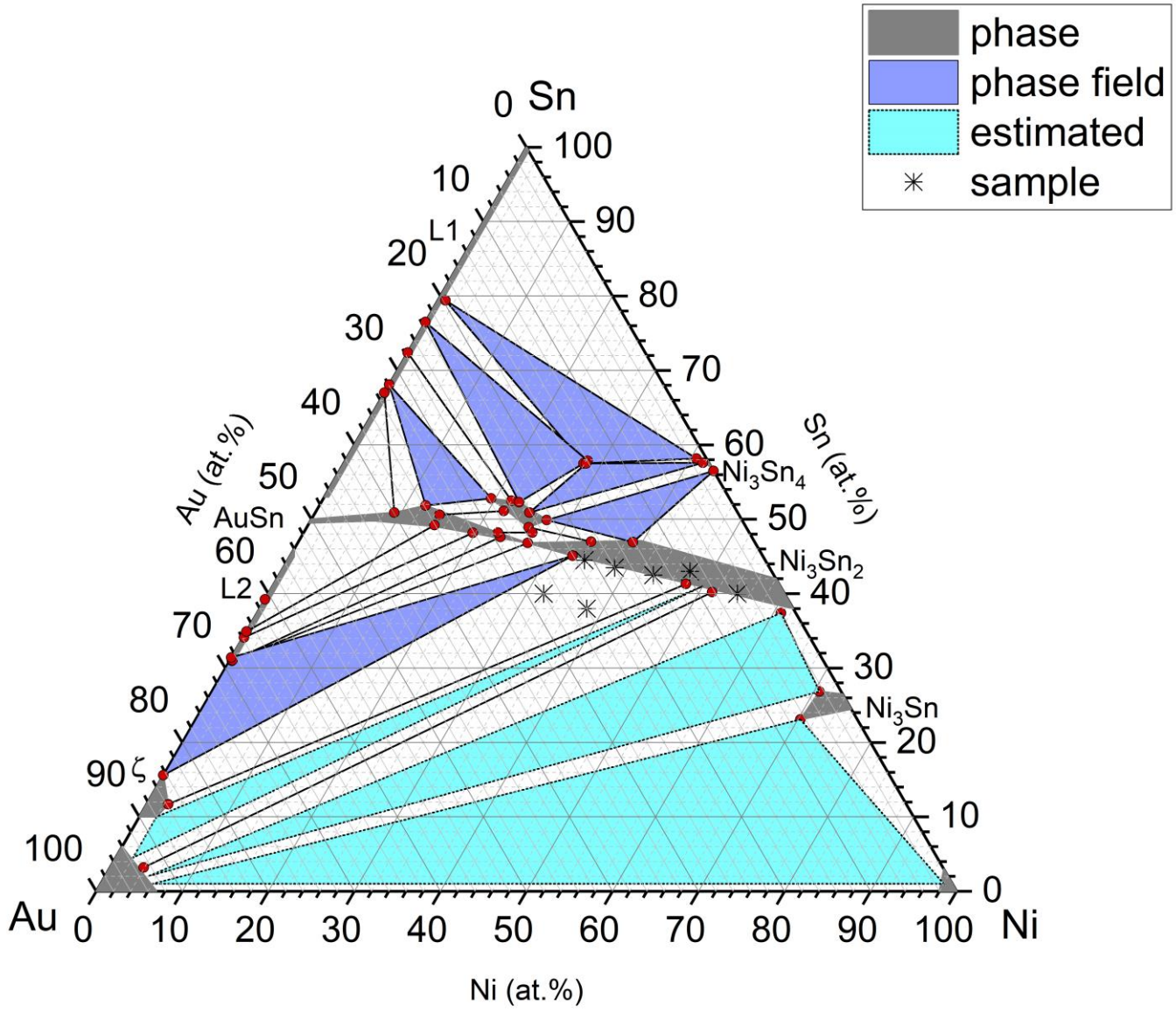

Figure 2.3.1.1 – Au-Ni-Sn phase diagram (45) with sample positions

2.3.2. Embedding, grinding, polishing, P-XRD, SEM, optical microscopy

Embedding, grinding, polishing, P-XRD, SEM and optical microscopy were carried out as with Al-Fe-Ge. SC-XRD was not utilized. For samples 10-12 and 15-20 grinding was omitted due to the fragility of the embedded powder.

3. Results

3.1. Al-Fe-Ge

The prepared samples, their phases, lattice parameters as well as compositions determined by P-XRD and SEM are listed in Table 3.1.1. Samples corresponding to the exact compositions of $\tau 6$ and $\tau 8$ contained the desired phase, as seen in SEM images in Figures 3.1.1 and 3.1.2. However, crystals of $\tau 6$ and $\tau 8$ were too small for SC-XRD. Therefore, samples in equilibrium with the liquid phase were prepared to grow larger crystals of $\tau 6$ and $\tau 8$ (samples AlFeGe 7, 8 and 9), which was successful for $\tau 8$. Large crystals of can be seen when comparing sample AlFeGe 7 with AlFeGe 2 and AlFeGe 6 in Figures 3.1.1. and 3.1.2.

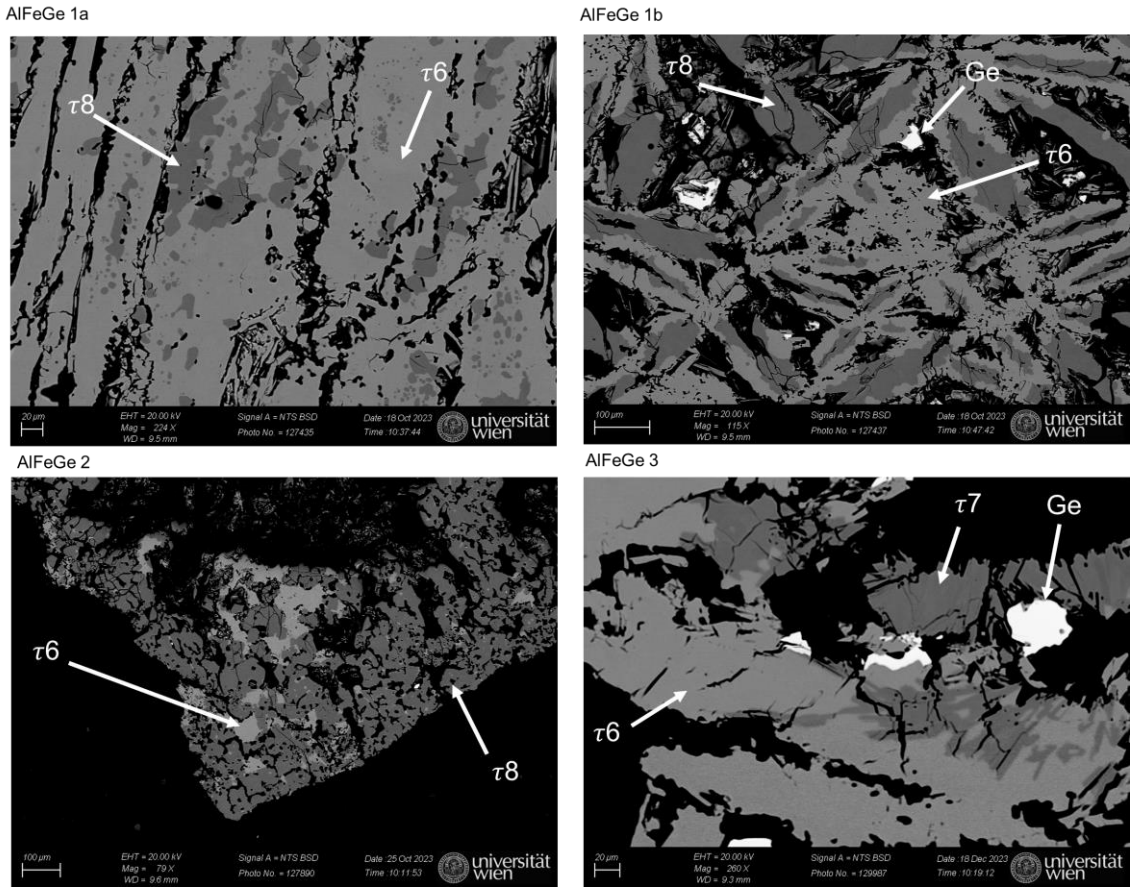

Figure 3.1.1 – SEM images of samples AlFeGe 1a-3

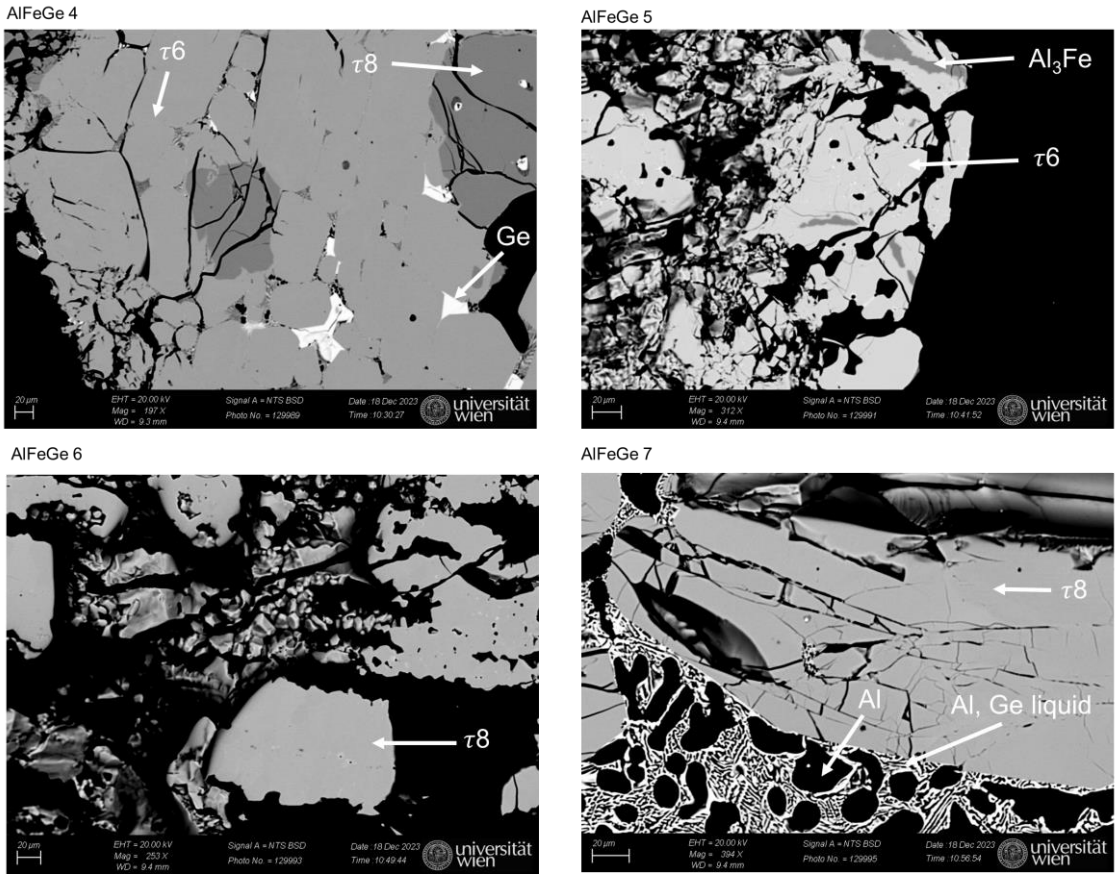

Figure 3.1.2 – SEM images of samples AlFeGe 4-7

A cross-polarized light microscopy image of AlFeGe 6 in Figure 3.1.3 shows crystals of τ8 smaller than 20 μm with domains of different orientation. The cross-polarized light image of AlFeGe 7 shows crystals of τ8 larger than 60 μm with a single domain.

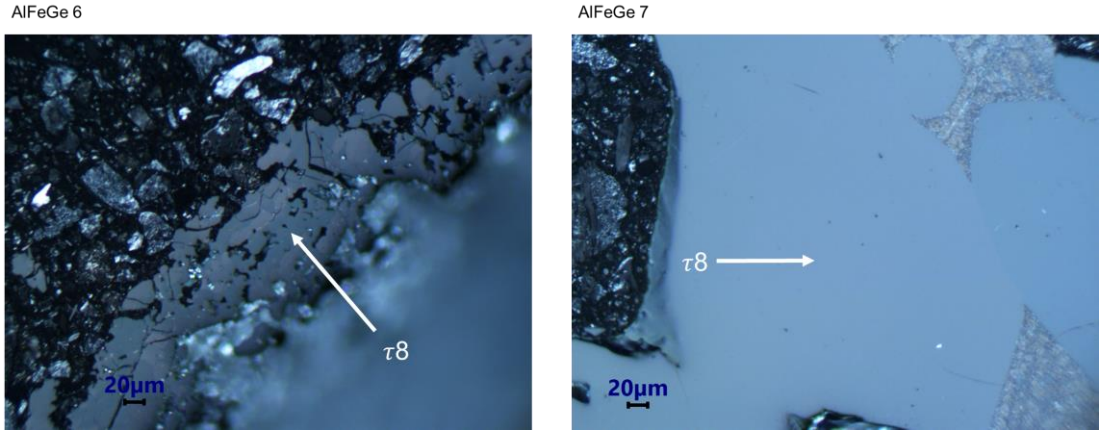

Figure 3.1.3 – Cross-polarized light microscopy images of samples AlFeGe 6 and AlFeGe 7 at x20 magnification

Table 3.1.1 - Al-Fe-Ge samples, their phases, lattice parameters and compositions determined by P-XRD and SEM

							Composition from P-XRD or SC-XRD if unchanged (at. %)			Composition from SEM (at. %)		
Sample	(Al/Fe/Ge)	Phase	Fraction (%)	a (Å)	b (Å)	c (Å)	Al	Fe	Ge	Al	Fe	Ge
1a	(66.0/7.5/26.5)	τ6	-	-	-	-	-	-	-	66.76 ± 0.02	7.12 ± 0.08	26.13 ± 0.09
		τ8	-	-	-	-	-	-	-	70.97 ± 0.14	9.27 ± 0.06	19.76 ± 0.08
1b	(66.0/7.5/26.5)	τ6	-	-	-	-	-	-	-	65.89 ± 0.18	7.17 ± 0.11	26.94 ± 0.07
		τ8	-	-	-	-	-	-	-	69.89 ± 0.18	9.44 ± 0.10	20.67 ± 0.27
2	(71.0/9.5/19.5)	τ6	-	-	-	-	-	-	-	66.49 ± 0.24	7.30 ± 0.07	26.33 ± 0.19
		τ8	-	18.117	23.189	13.386	71	10	19	70.60 ± 0.30	9.52 ± 0.16	19.89 ± 0.22
3	(65.6/7.4/27.0)	τ6	-	-	-	-	-	-	-	65.69 ± 0.18	7.12 ± 0.10	27.16 ± 0.24
		τ7	-	20.994	6.281	6.324	66	16	18	66.96 ± 0.24	15.16 ± 0.05	17.87 ± 0.21
		Ge	-	5.668	-	-	-	-	100	4.37 ± 1.28	1.31 ± 0.67	94.32 ± 1.30
4	(66.4/7.2/26.4)	τ6	-	-	-	-	-	-	-	66.13 ± 0.17	7.09 ± 0.07	26.79 ± 0.16

Table 3.1.1 (continued) - Al-Fe-Ge samples, their phases, lattice parameters and compositions determined by P-XRD and SEM

							Composition from P-XRD or SC-XRD if unchanged (at. %)			Composition from SEM (at. %)		
Sample	(Al/Fe/Ge)	Phase	Fraction (%)	a (Å)	b (Å)	c (Å)	Al	Fe	Ge	Al	Fe	Ge
		$\tau 8$	-	18.108	23.211	13.364	71	9	20	70.27 ± 0.04	9.50 ± 0.04	20.23 ± 0.04
		Ge	-	5.675	-	-	-	-	100	4.47 ± 0.12	0.95 ± 0.09	94.58 ± 0.13
5	(71.6/9.7/18.7)	$\tau 8$	93	18.152	23.185	13.385	71	10	19	70.91 ± 0.40	9.62 ± 0.23	19.46 ± 0.20
		Al_3Fe	7	15.484	8.099	12.184	76	24	-	75.62 ± 0.05	23.07 ± 0.21	1.31 ± 0.16
6	(71.1/9.4/19.4)	$\tau 8$	100	18.149	23.182	13.383	71	10	19	71.45 ± 0.54	9.45 ± 0.10	19.09 ± 0.44
7	(73.3/6.7/20.0)	$\tau 8$	75	18.104	23.201	13.393	71	10	19	71.25 ± 0.36	9.40 ± 0.16	19.35 ± 0.24
		Al	15	4.052	-	-	100	-	-	96.91 ± 0.09	-	3.09 ± 0.09
		Ge	10	5.671	-	-	-	-	100	-	-	-

In order to determine the melting points of $\tau 6$ and $\tau 8$, DTA measurements were performed with samples AlFeGe 1a, AlFeGe 1b and AlFeGe 2. The first DTA cycle of samples AlFeGe 1a and AlFeGe 1b, shown in Figures 3.1.4 and 3.1.7, revealed one invariant melting point at mean onset value of 522.35 °C. The second peak at 579 °C is not incongruent. The first DTA cycle of sample AlFeGe 2, which predominantly contains $\tau 8$, revealed one incongruent melting point at 537.1 °C, shown in Figure 3.1.10. The second and third DTA cycles, shown in Figures 3.1.5, 3.1.6, 3.1.8, 3.1.9, 3.1.11 and 3.1.12, that $\tau 6$ and $\tau 8$ are still present, so they crystallize again during cooling. Furthermore, new peaks reveal that equilibrium is not fully recovered during cooling. The predicted reactions are as follows:

$$L \rightleftharpoons \tau 6 + Al + Ge$$

Reaction 3.1.1 - $\tau 6$ ternary eutectic reaction at 416 °C

$$L + \tau 8 \rightleftharpoons \tau 6 + Al$$

Reaction 3.1.2 - Transition reaction at 460 °C

$$Al_{13}Fe_4 + Ge + L \rightleftharpoons \tau 8$$

Reaction 3.1.3 - $\tau 8$ peritectic reaction at 532 °C

$$\tau 8 + L + Ge \rightleftharpoons \tau 6$$

Reaction 3.1.4 - $\tau 6$ ternary peritectoid reaction at 522 °C

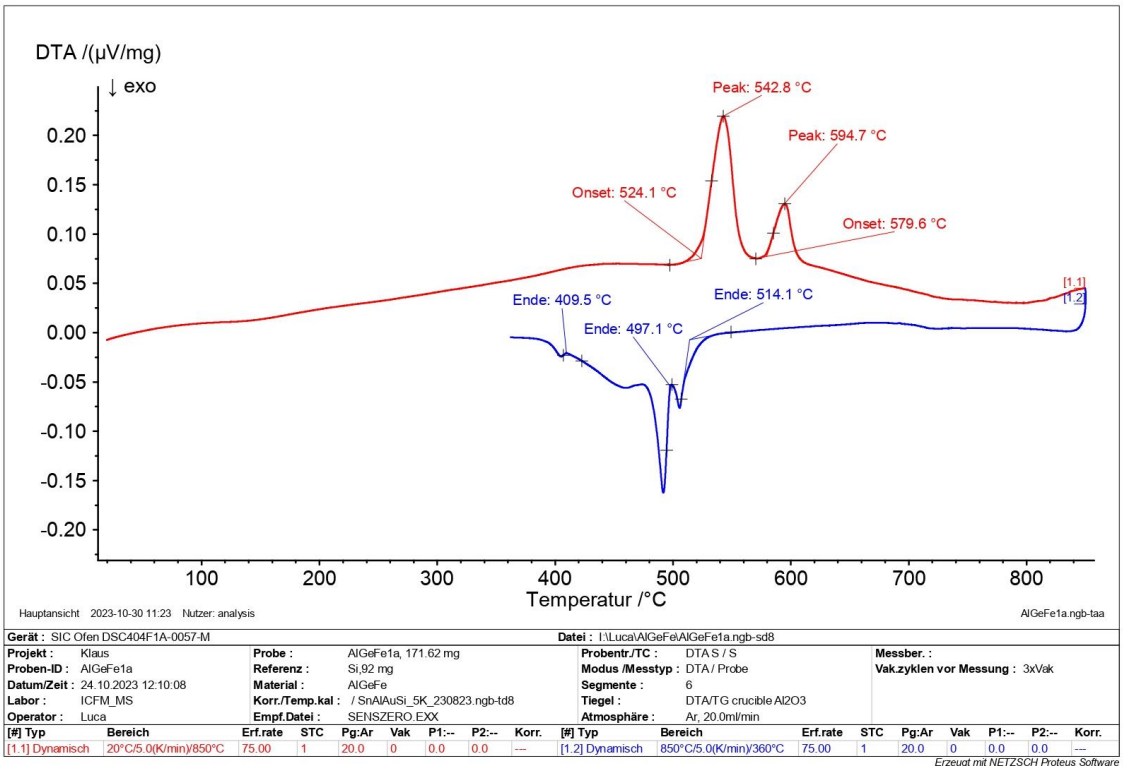

Figure 3.1.4 – DTA cycle 1 of sample AlFeGe 1a

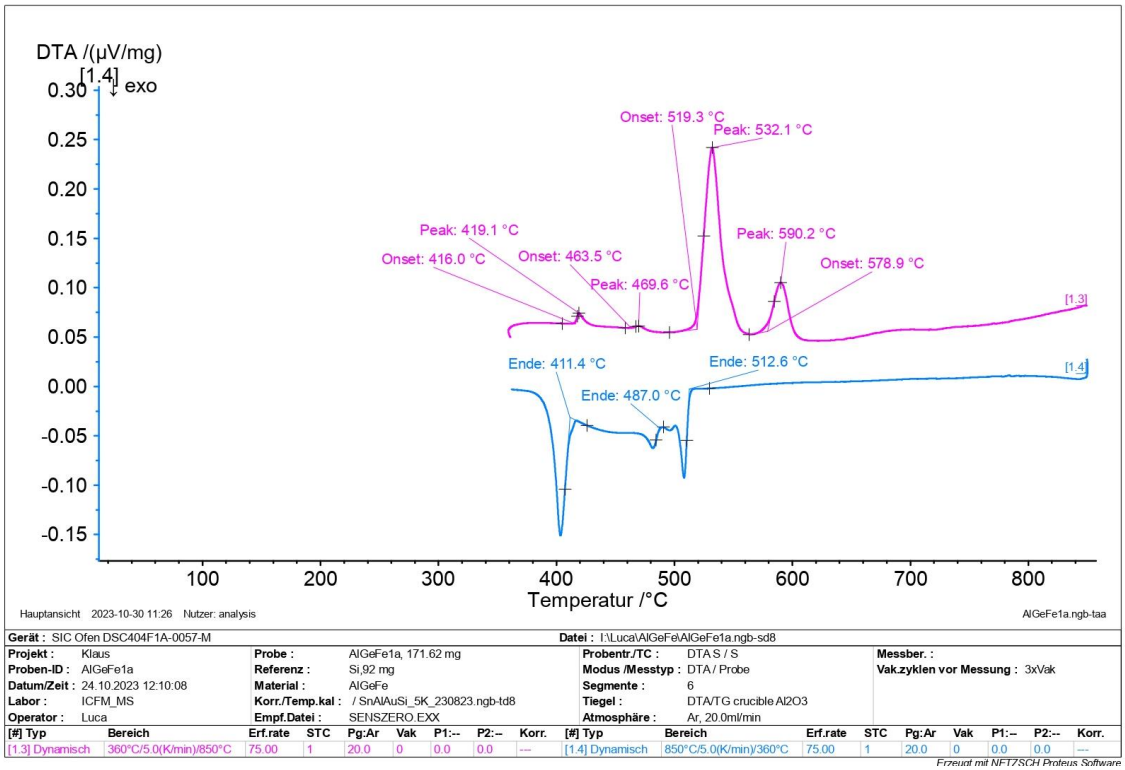

Figure 3.1.5 – DTA cycle 2 of sample AlFeGe 1a

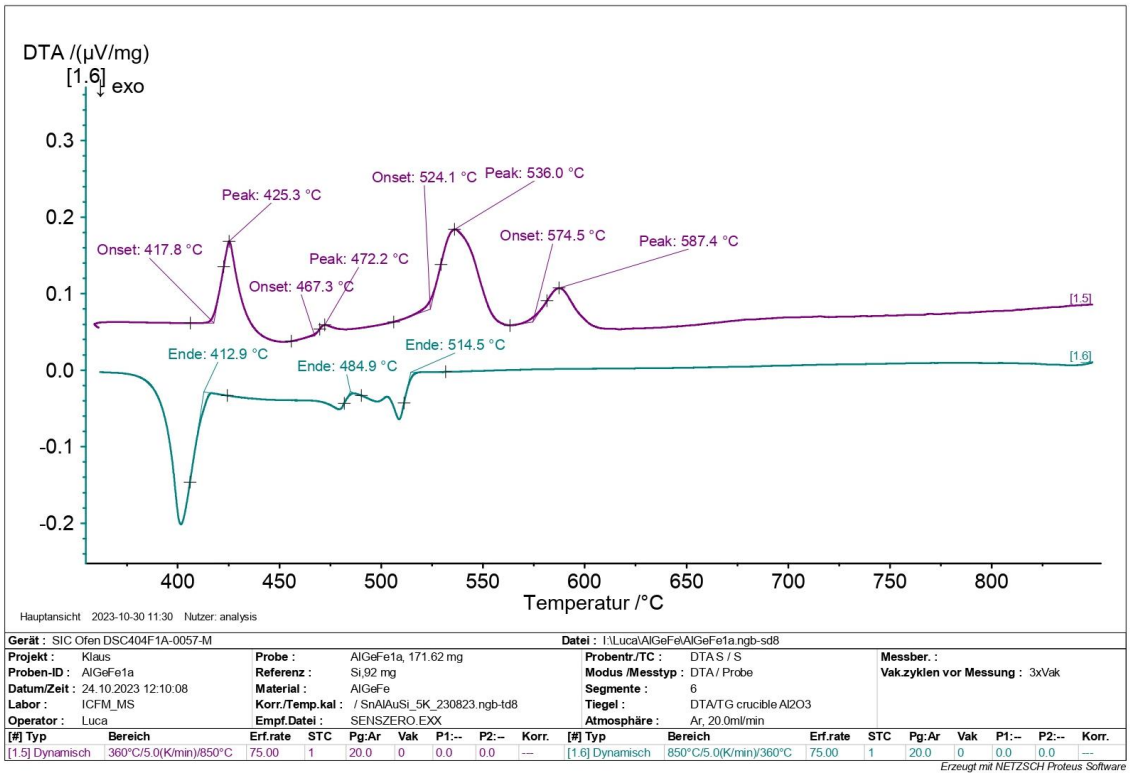

Figure 3.1.6 – DTA cycle 3 of sample AlFeGe 1a

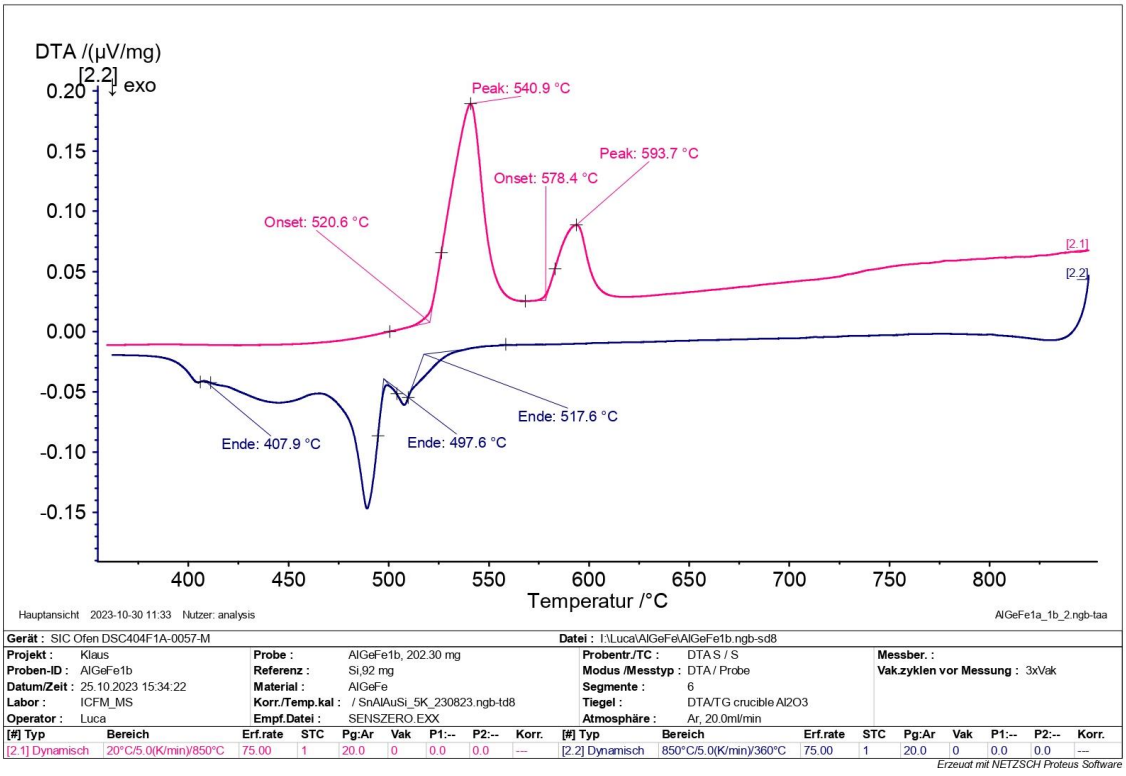

Figure 3.1.7 – DTA cycle 1 of sample AlFeGe 1b

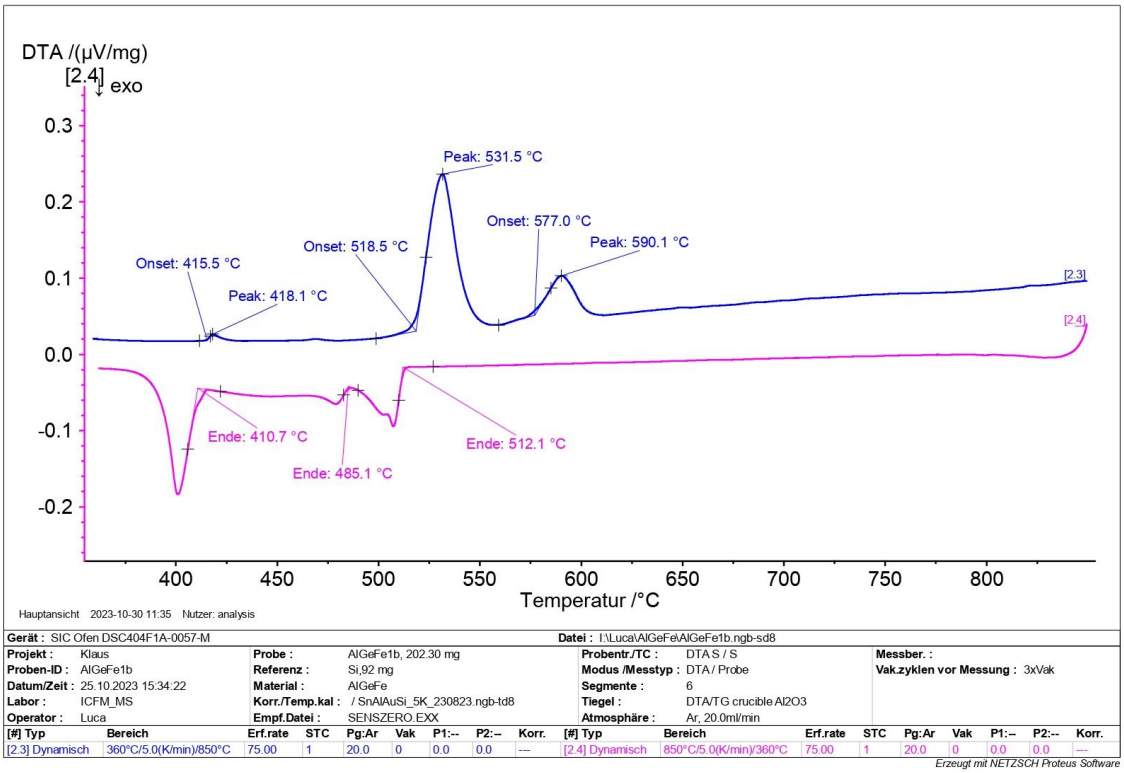

Figure 3.1.8 – DTA cycle 2 of sample AlFeGe 1b

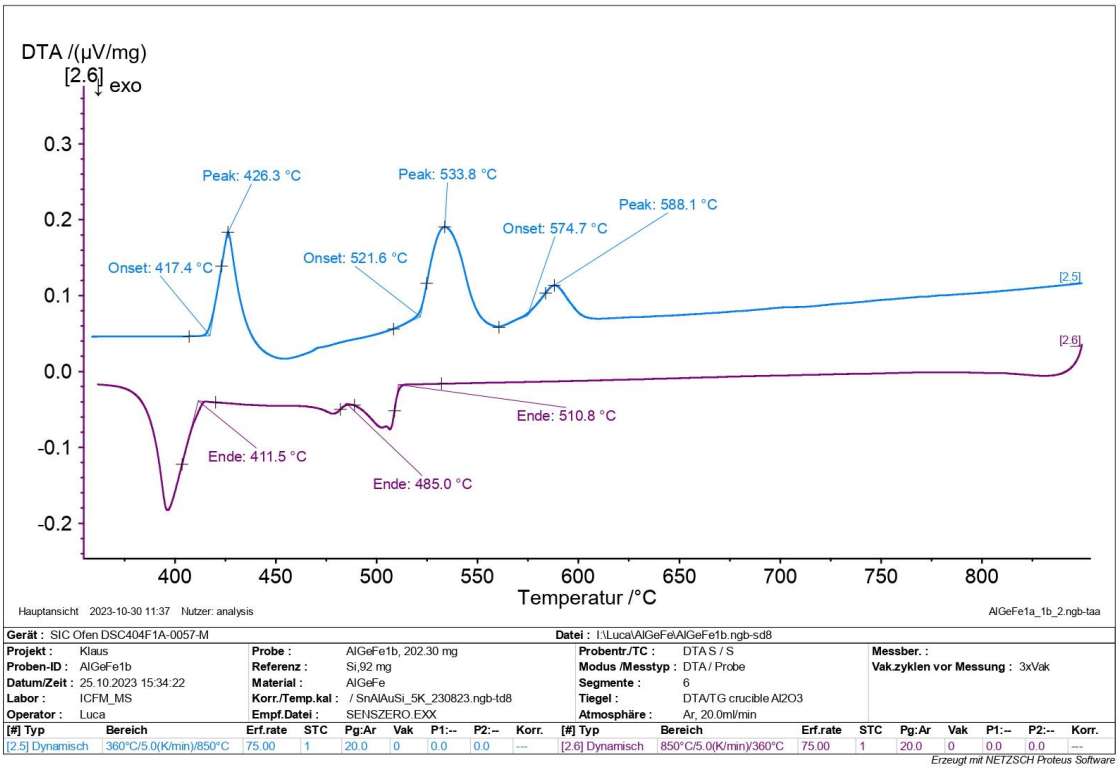

Figure 3.1.9 – DTA cycle 3 of sample AlFeGe 1b

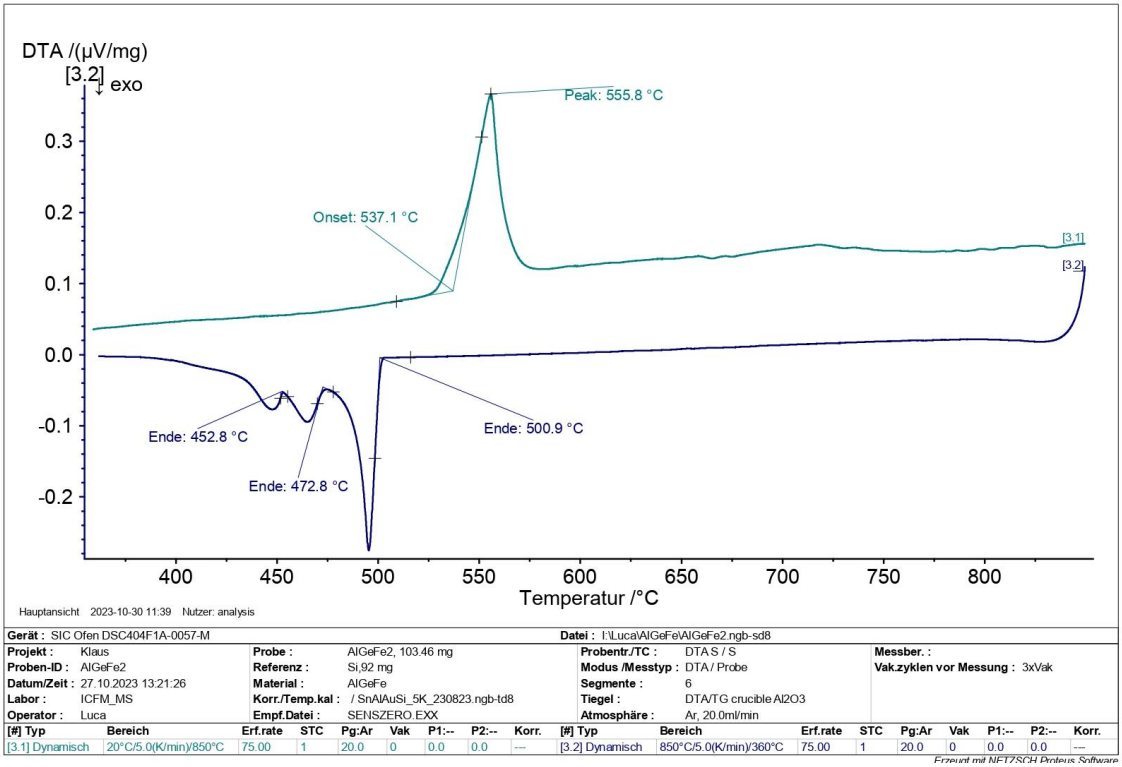

Figure 3.1.10 – DTA cycle 1 of sample AlFeGe 2

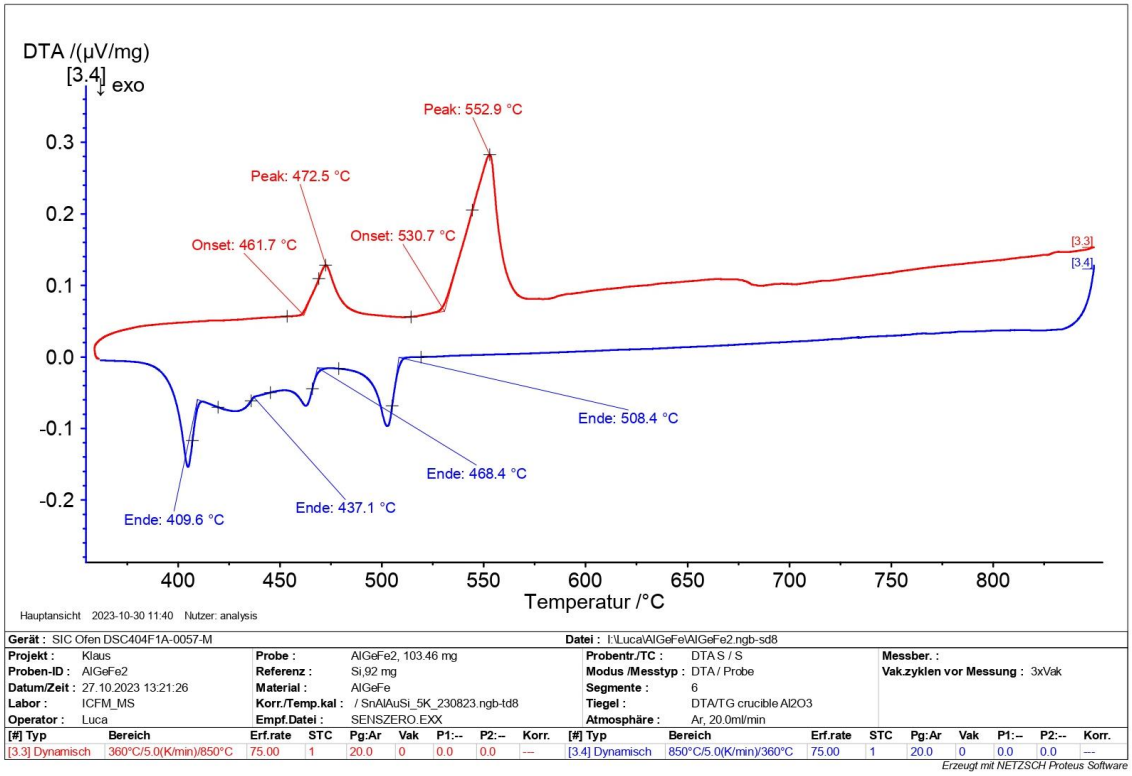

Figure 3.1.11 – DTA cycle 2 of sample AlFeGe 2

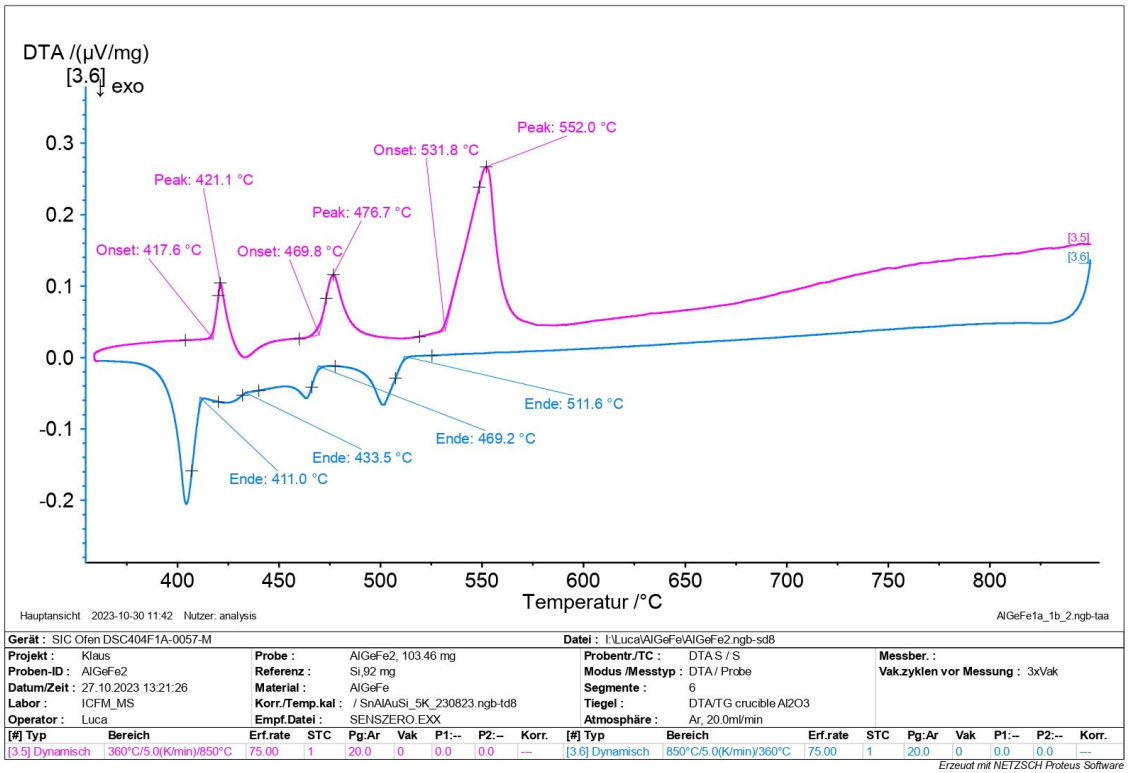

Figure 3.1.12 – DTA cycle 3 of sample AlFeGe 2

To determine the crystal structure, a crystal of $\tau 8$ with 65 µm size was selected from sample AlFeGe 7 for SC-XRD. The SC-XRD data of $\tau 8$ are listed in Tables 3.1.2 to 3.1.4. Unfortunately, it was not possible to determine the structure of $\tau 6$.

Table 3.1.2 – SC-XRD data of τ8

Sample	AlFeGe 7
Phase notation	$\tau 8$
Compound	Al_7FeGe_2
Structure type	own
Pearson symbol	*oF*373
a (Å)	13.40 (9)
b (Å)	18.11 (2)
c (Å)	23.11 (2)
Space group	*Fmm2*
V (Å^3) / Z	5634 (3)
ρ_{calc} (g cm^{-3}) / μ(Mo K$_\alpha$) (mm^{-1})	3.82 /11.4
Crystal dimensions (μm)	6 x 7 x 65
Range of data collection (±h ±k ±l) (°)	3 < 2θ < 80
Measured reflections	20368
Unique reflections (n) / reflections with $F_o > 4\sigma(F_o)$	9394 / 4226
$R_{int} = \sum\lvert F_o^2 - F_o^2(mean)\rvert \,/\, \sum F_o^2$	0.065
Extinction parameter k $F_c^* = F_c k[1 + 0.001F_c^2\lambda^3 \,/\, \sin 2\theta]^{-\frac{1}{4}}$	0.000087 (4)
$R1 = \sum\left(\lvert\lvert F_0^2\rvert - \lvert F_c^2\rvert\rvert\right)^2 \,/\, \sum F_o$ (observed / all reflections)	0.087 / 0.040
$\omega R2 = [\sum \omega\,(F_0^2 - F_c^2)^2 \,/\, \sum \omega F_0^4]^{\frac{1}{2}}$	0.069
$GooF = [\sum \omega\,(F_0^2 - F_c^2)^2 \,/\, (n-p)]^{\frac{1}{2}}$	1.01
Variable parameters / weighting parameter *a*, *b*	243 / 0.02, 0.00
Final difference Fourier map (eÅ^{-3})	-1.52 to +1.44

Table 3.1.3 - Sites, occupation, multiplicity and coordinates of $\tau 8$

Atom	Occ.	Wyckoff letter	Site symmetry	*x*	*y*	*z*	U_{equiv}	U_{11}	U_{22}	U_{33}	U_{23}	U_{13}	U_{12}
Fe1	Fe_1	8(*d*)	.*m*.	0.13176(4)	0	0.50616(7)	0.00974(16)	0.0141(4)	0.0059(3)	0.0091(4)	0	-0.0058(3)	0
Fe2	Fe_1	8(*d*)	.*m*.	0.12917(4)	0	0.00692(7)	0.00650(15	0.0077(3)	0.0061(3)	0.0057(4)	0	-0.0009(3)	0
Fe3	Fe_1	16(*e*)	1	0.12737(3)	0.25091(2)	0.24732(6)	0.00685(11)	0.0079(2)	0.0063(2)	0.0064(3)	-0.00041(19)	-0.0005(2)	0.0003(2)
Ge1	Ge_1	8(*c*)	*m*..	0	0.16678(2)	0	0.01091(11)	0.0122(3)	0.0104(3)	0.0101(3)	-0.0007(3)	0	0
Ge2	Ge_1	8(*c*)	*m*..	0	0.08739(2)	0.75626(6)	0.01176(13)	0.0111(3)	0.0112(3)	0.0130(3)	0.0015(3)	0	0
Ge3	Ge_1	8(*c*)	*m*..	0	0.32698(2)	0.00073(6)	0.01296(12)	0.0092(3)	0.0184(3)	0.0112(3)	0.0001(3)	0	0
Ge4	Ge_1	8(*c*)	*m*..	0	0.08249(3)	0.25214(7)	0.02663(18)	0.0099(3)	0.0203(4)	0.0497(5)	-0.0198(3)	0	0
Ge5	Ge_1	16(*e*)	1	0.24572(2)	0.667430(15)	0.00329(5)	0.01033(9)	0.01224(19)	0.00984(18)	0.0089(2)	-0.00072(18)	0.00036(18)	0.00004(15)
Ge6	Ge_1	16(*e*)	1	0.24892(2)	0.083874(15)	0.24898(5)	0.01157(9)	0.0150(2)	0.00972(18)	0.00998(19)	-0.00040(18)	0.00074(17)	0.00031(17)
Al1	Al_1	8(*c*)	*m*..	0	0.20799(8)	0.81870(15)	0.0200(4)	0.0107(9)	0.0325(10)	0.0168(9)	0.0080(8)	0	0
Al2	Al_1	8(*c*)	*m*..	0	0.23351(8)	0.15709(16)	0.0219(4)	0.0135(9)	0.0316(11)	0.0206(9)	-0.0112(8)	0	0
Al3	Al_1	8(*d*)	.*m*.	0.15588(10)	0	0.68483(14)	0.0173(4)	0.0168(9)	0.0263(10)	0.0089(8)	0	0.0013(7)	0
Al4	Al_1	8(*d*)	.*m*.	0.07448(9)	0	0.84274(14)	0.0113(3)	0.0089(8)	0.0183(9)	0.0068(7)	0	-0.0001(6)	0
Al5	Al_1	8(*d*)	.*m*.	0.22867(10)	0	0.87668(15)	0.0150(4)	0.0196(10)	0.0113(8)	0.0140(9)	0	0.0071(7)	0
Al6	Al_1	8(*b*)	1	1/4	1/4	0.14678(14)	0.0148(4)	0.0115(8)	0.0181(9)	0.0149(8)	0	0	-0.0028(7)
Al7	Al_1	16(*e*)	1	0.25225(7)	0.05808(5)	0.05305(12)	0.0175(3)	0.0249(7)	0.0120(6)	0.0155(6)	0.0000(5)	-0.0056(6)	0.0014(5)
Al8	Al_1	16(*e*)	1	0.23011(7)	0.19013(5)	0.31529(12)	0.0186(3)	0.0254(7)	0.0170(6)	0.0133(6)	-0.0029(5)	-0.0053(5)	0.0080(5)
Al9	Al_1	16(*e*)	1	0.08055(7)	0.08936(5)	0.57853(14)	0.0229(3)	0.0174(7)	0.0177(6)	0.0337(8)	-0.0129(6)	-0.0095(6)	0.0056(5)
Al10	Al_1	16(*e*)	1	0.13551(7)	0.27804(6)	0.42103(11)	0.0152(3)	0.0186(7)	0.0174(6)	0.0095(6)	-0.0016(5)	-0.0005(5)	-0.0024(5)
Al11	Al_1	16(*e*)	1	0.13194(7)	0.17475(5)	0.12369(12)	0.0166(3)	0.0192(7)	0.0137(6)	0.0168(6)	-0.0055(5)	0.0027(5)	-0.0018(5)
Al12	Al_1	16(*e*)	1	0.12770(6)	0.35638(5)	0.25727(12)	0.0139(2)	0.0155(6)	0.0101(5)	0.0162(6)	0.0016(5)	-0.0021(5)	-0.0004(5)
Al13	Al_1	16(*e*)	1	0.12512(8)	0.09959(6)	0.95331(12)	0.0227(3)	0.0417(9)	0.0093(6)	0.0171(6)	0.0029(5)	-0.0028(6)	0.0017(6)
Al14	Al_1	16(*e*)	1	0.12067(7)	0.05923(5)	0.15694(13)	0.0190(3)	0.0320(8)	0.0134(6)	0.0114(6)	-0.0039(5)	0.0074(6)	-0.0036(5)
Al15	Al_1	16(*e*)	1	0.12091(6)	0.29594(5)	0.08300(11)	0.0145(3)	0.0152(6)	0.0173(6)	0.0109(6)	0.0019(5)	0.0007(5)	0.0019(5)
Al16	Al_1	16(*e*)	1	0.07635(6)	0.16935(5)	0.33252(12)	0.0138(2)	0.0125(6)	0.0114(6)	0.0175(6)	0.0028(5)	0.0025(5)	-0.0010(4)
Al17*a*	$Al_{0.466(8)}$	16(*e*)	1	0.1343(2)	0.0655(2)	0.3726(3)	0.0188(13)	0.0133(19)	0.021(2)	0.0218(19)	0.0100(16)	0.0058(15)	0.0060(16)
Al17*b*	$Al_{0.534(8)}$	16(*e*)	1	0.16088(19)	0.08822(15)	0.4038(2)	0.0127(9)	0.0120(15)	0.0119(15)	0.0142(14)	0.0036(11)	0.0000(11)	0.0000(11)
Al18*a*	$Al_{0.485(9)}$	4(*a*)	*mm*2	0	0	0.4134(4)	0.0192(18)	0.014(3)	0.022(3)	0.021(3)	0	0	0
Al18*b*	$Al_{0.564(9)}$	4(*a*)	*mm*2	0	0	0.5035(3)	0.0104(13)	0.008(2)	0.010(2)	0.014(2)	0	0	0
Al18*c*	$Al_{0.432(8)}$	4(*a*)	*mm*2	0	0	0.6127(4)	0.0159(18)	0.023(4)	0.012(3)	0.012(3)	0	0	0
Al18*d*	$Al_{0.560(5)}$	8(*d*)	.*m*.	0.07572(16)	0	0.3287(2)	0.0130(9)	0.0112(16)	0.0189(17)	0.0087(15)	0	-0.0002(12)	0
Al19*a*	$Al_{0.696(6)}$	8(*c*)	*m*..	0	0.05497(11)	0.0334(2)	0.0169(8)	0.0098(13)	0.0118(14)	0.0292(16)	0.0025(10)	0	0
Al19*b*	$Al_{0.285(9)}$	4(*a*)	*mm*2	0	0	0.0265(6)	0.015(3)	0.005(4)	0.026(6)	0.014(5)	0	0	0

Table 3.1.4 – Bond lengths of τ8

Bond	Distance (Å)	Multiplicity
Fe1−Al17*a*	2.3471(3)	2x
Fe1−Al18*b*	2.3878(8)	
Fe1−Al3	2.431(2)	
Fe1−Al9	2.4703(13)	2x
Fe1−Al17*b*	2.520(3)	2x
Fe1−Al7	2.5748(14)	2x
Fe1−Al18*d*	2.584(3)	
Fe1−Al18*a*	2.691(3)	
Fe1−Al18*c*	2.781(3)	
Fe2−Al19*b*	2.3551(12)	
Fe2−Al4	2.411(2)	
Fe2−Al13	2.4218(14)	2x
Fe2−Al14	2.4387(17)	2x
Fe2−Al5	2.5081(19)	
Fe2−Al7	2.6782(14)	2x
Fe2−Al19*a*	2.6891(14)	2x
Fe3−Al16	2.3960(13)	
Fe3−Al10	2.4137(17)	
Fe3−Al11	2.4231(15)	
Fe3−Al15	2.4381(16)	
Fe3−Al12	2.4520(13)	
Fe3−Al8	2.5068(13)	
Fe3−Al6	2.5979(12)	
Fe3−Al2	2.6361(12)	
Fe3−Al1	2.6740(11)	
Ge1−Al1	2.609(2)	
Ge1−Al2	2.612(2)	
Ge1−Al19*a*	2.634(3)	
Ge1−Al13	2.8220(14)	2x

Table 3.1.4 (continued) – Bond lengths of $\tau 8$

Bond	Distance (Å)	Multiplicity
Ge1−Al11	2.9140(14)	2x
Ge1−Al10	2.9643(13)	2x
Ge2−Al12	2.6567(12)	2x
Ge2−Al4	2.6976(12)	2x
Ge2−Al9	2.7915(17)	2x
Ge2−Al18*c*	2.794(4)	
Ge2−Al1	2.922(2)	
Ge3−Al15	2.5557(12)	2x
Ge3−Al9	2.6433(14)	2x
Ge3−Al16	2.6441(15)	2x
Ge4−Al18*d*	2.569(2)	2x
Ge4−Al14	2.5878(14)	
Ge4−Al14	2.5877(15)	
Ge4−Al16	2.6715(13)	2x
Ge4−Al18*a*	2.886(4)	
Ge4−Al17*a*	2.946(5)	2x
Ge4−Al19*a*	2.998(3)	
Ge5−Al8	2.5866(16)	
Ge5−Al7	2.6246(13)	
Ge5−Al15	2.6414(13)	
Ge5−Al6	2.7147(14)	
Ge5−Al10	2.7287(13)	
Ge5−Al17*b*	2.742(5)	
Ge5−Al11	2.7460(14)	
Ge5−Al13	2.8990(15)	
Ge6−Al17b	2.618(3)	
Ge6−Al5	2.6225(13)	
Ge6−Al12	2.6332(12)	
Ge6− Al8	2.6436(13)	
Ge6−Al17*a*	2.690(3)	

Table 3.1.4 (continued) – Bond lengths of $\tau 8$

Bond	Distance (Å)	Multiplicity
Ge6−Al7	2.6909(15)	
Ge6−Al14	2.6918(15)	
Ge6−Al3	2.7394(13)	
Al1−Al2	2.554(3)	
Al1−Ge1	2.609(2)	
Al1−Fe3	2.6740(11)	2x
Al1−Al10	2.8303(15)	2x
Al1−Al12	2.8747(16)	2x
Al1−Ge2	2.922(2)	
Al2−Al1	2.554(3)	
Al2−Ge1	2.612(2)	
Al2−Fe3	2.6361(12)	2x
Al2−Al11	2.7886(15)	2x
Al2−Al15	2.8077(17)	2x
Al3−Fe	2.431(2)	
Al3−Al4	2.578(2)	
Al3−Ge6	2.7394(13)	2x
Al3−Al7	2.7751(19)	2x
Al4−Fe2	2.411(2)	
Al4−Al3	2.578(2)	
Al4−Ge2	2.6976(12)	2x
Al4−Al4	2.699(3)	
Al4−Al19*b*	2.805(7)	
Al4−Al5	2.831(2)	
Al4−Al13	2.8944(17)	2x
Al5−Fe2	2.5081(19)	
Al5−Ge6	2.6225(13)	2x
Al5−Al7	2.7522(18)	2x
Al5−Al4	2.831(2)	
Al5−A17	2.887(3)	2x

Table 3.1.4 (continued) – Bond lengths of $\tau 8$

Bond	Distance (Å)	Multiplicity
Al5−Al3	2.887(2)	
Al5−Al17*a*	2.912(3)	2x
Al6−Fe3	2.5979(12)	
Al6−Al8	2.6739(19)	2x
Al6−Al15	2.7088(13)	2x
Al6−Ge5	2.7147(14)	2x
Al6−Al11	2.7791(12)	2x
Al7−Fe1	2.5748(14)	
Al7−Ge5	2.6246(13)	
Al7−Al17*b*	2.638(3)	
Al7−Fe2	2.6782(14)	
Al7−Ge6	2.6909(15)	
Al7−Al7	2.697(2)	
Al7−Al5	2.7522(18)	
Al7−Al14	2.7603(19)	
Al7−Al3	2.7751(19)	
Al7−Al13	2.8314(18)	
Al8−Fe3	2.5068(13)	
Al8−Ge5	2.5866(16)	
Al8−Ge6	2.6436(13)	
Al8−Al6	2.6739(19	
Al8−Al16	2.8371(17)	
Al8−Al8	2.872(2)	
Al8−Al12	2.8996(17)	
Al8−Al10	2.9118(17)	
Al8−Al17*b*	2.928(4)	
Al9−Fe1	2.4703(13)	
Al9−Al18*c*	2.5774(16)	
Al9−Ge3	2.6433(14)	
Al9−Al18*b*	2.7278(19)	

Table 3.1.4 (continued) – Bond lengths of $\tau 8$

Bond	Distance (Å)	Multiplicity
Al9−Al17*b*	2.755(3)	
Al9−Al15	2.7620(17)	
Al9−Ge2	2.7915(17)	
Al9−Al12	2.8356(18)	
Al9−Al3	2.8619(17)	
Al9−Al9	2.919(2)	
Al9−Al17*a*	2.975(4)	
Al10−Fe3	2.4137(17)	
Al10−Ge5	2.7287(13)	
Al10−Al15	2.7785(17)	
Al10−Al1	2.8303(15)	
Al10−Al12	2.8518(17)	
Al10−Al13	2.8794(18)	
Al10−Al8	2.9118(17)	
Al10−Al11	2.9265(18)	
Al10−Ge1	2.9643(13)	
Al10−Al16	2.9866(17)	
Al10−Al8	3.0178(17)	
Al11−Fe3	2.4231(15)	
Al11−Al14	2.7259(18)	
Al11−Ge5	2.7460(14)	
Al11−Al6	2.7791(12)	
Al11−Al2	2.7886(15)	
Al11−Al15	2.8725(17)	
Al11−Al13	2.8742(19)	
Al11−Ge1	2.9140(14)	
Al11−Al10	2.9265(18)	
Al11−Al16	2.9739(18)	
Al12−Fe3	2.4520(13)	
Al12−Ge6	2.6332(12)	

Table 3.1.4 (continued) – Bond lengths of τ8

Bond	Distance (Å)	Multiplicity
Al12−Ge2	2.6567(12)	
Al12−Al15	2.7251(17)	
Al12−Al13	2.8165(19)	
Al12−Al9	2.8356(18)	
Al12−Al10	2.8518(17)	
Al12−Al1	2.8747(16)	
Al12−Al8	2.8996(17)	
Al13−Fe2	2.4218(14)	
Al13−Al19*a*	2.713(2)	
Al13−Al12	2.8165(19)	
Al13−Ge1	2.8220(14)	
Al13−Al7	2.8314(18)	
Al13−Al11	2.8742(19)	
Al13−Al10	2.8794(18)	
Al13−Al14	2.8834(19)	
Al13−Al4	2.8944(17)	
Al13−Ge5	2.8990(15)	
Al14−Fe2	2.4387(17)	
Al14−Ge4	2.5877(14)	
Al14−Ge6	2.6918(15)	
Al14−Al11	2.7259(18)	
Al14−Al19*a*	2.744(2)	
Al14−Al14	2.750(3)	
Al14−Al7	2.7603(19)	
Al14−Al18*d*	2.800(3)	
Al14−Al13	2.8834(19)	
Al14−Al17*a*	2.902(6)	
Al15−Fe3	2.4381(16)	
Al15−Ge3	2.5557(12)	
Al15−Ge5	2.6414(13)	

Table 3.1.4 (continued) – Bond lengths of $\tau 8$

Bond	Distance (Å)	Multiplicity
Al15−Al6	2.7088(13)	
Al15−Al12	2.7251(17)	
Al15−Al9	2.7619(17)	
Al15−Al10	2.7785(17)	
Al15−Al2	2.8077(17)	
Al15−Al11	2.8725(17)	
Al16−Fe3	2.3960(13)	
Al16−Al17*b*	2.609(3)	
Al16−Ge3	2.6441(15)	
Al16−Ge4	2.6715(13)	
Al16−A17*a*	2.684(3)	
Al16−Al1	2.7667(23)	
Al16−Al8	2.8371(17)	
Al16−Al11	2.9739(18)	
Al16−Al10	2.9866(17)	
Al17A−Fe1	2.347(3)	
Al17A−Al16	2.684(3)	
Al17A−Ge6	2.690(3)	
Al17A−Al14	2.902(5)	
Al17A−Al5	2.912(3)	
Al17A−Al18*a*	2.921(5)	
Al17A−Ge4	2.946(5)	
Al17A−Al9	2.975(4)	
Al17B− Fe1	2.520(3)	
Al17B−Al16	2.609(3)	
Al17B−Ge6	2.618(3)	
Al17B−Al7	2.638(3)	
Al17B−Ge5	2.742(5)	
Al17B−Al18*d*	2.754(5)	
Al17B−Al9	2.755(3)	

Table 3.1.4 (continued) – Bond lengths of $\tau 8$

Bond	Distance (Å)	Multiplicity
Al17B−Al5	2.887(3)	
Al17B−Al8	2.928(4)	
Al18A−Al18*c*	2.668(8)	
Al18A−Fe1	2.691(3)	2x
Al18A−Ge4	2.886(4)	2x
Al18A−Al17*a*	2.921(5)	4x
Al18B− Fe1	2.3878(8)	2x
Al18B−Al18*d*	2.713(5)	2x
Al18B−Al9	2.7278(19)	4x
Al18C−Al9	2.5774(16)	2x
Al18C−Al9	2.5774(16)	2x
Al18C−Al18*a*	2.668(8)	
Al18C−Fe1	2.781(3)	2x
Al18C−Ge2	2.794(4)	2x
Al18C−Al3	2.985(3)	2x
Al18D−Ge4	2.569(2)	2x
Al18D−Fe1	2.584(3)	
Al18D−A18*b*	2.713(5)	
Al18D−Al18*d*	2.744(6)	
Al18D−Al17*b*	2.754(5)	2x
Al18D−Al14	2.800(3)	2x
Al19A−Al19*a*	2.552(5)	
Al19A−Ge1	2.634(3)	
Al19A−Fe2	2.6891(14)	2x
Al19A−Al13	2.713(2)	2x
Al19A−Al14	2.744(2)	2x
Al19B−Fe2	2.3551(12)	2x
Al19B−Al4	2.805(7)	

Phase $\tau 8$ is orthorhombic of structure type *Fmm2* and the formula of $\tau 8$ was determined to be Al_7FeGe_2. There are 372.59 atoms in the unit cell, of which 32 are Fe, 64 are Ge and 276.59 are Al. The structure of $\tau 8$ is best described as chains of Fe and Ge surrounded by Al atoms. There are 33 independent atomic positions, four with Fe, six with Ge and 23 with Al. In the overall structure, there are differences in occupations in positions Al17a – Al19b. However, locally these positions contain specific atoms. In Table 3.1.3, the occupancy of positions Al17a and Al17b adds up to 1 and the occupancy of positions Al19a and Al19b adds up to 0.981. The occupancy of positions 18a – 18d adds up to 2.041. Due to the partial occupations of positions Al17a-b, Al18a-d and Al19a-d, different structural models are possible in the independent positions. Consequently, coordination models were generated where atoms were removed that were too near to each other and hence occupied positions that were impossible in reality i.e. had overlapping interatomic distances according to the covalent radii of Al (1.25 Å), Fe (1.16 Å) and Ge (1.22 Å) (55). The following simultaneous occupation of atomic positions are impossible due to too short distances:

Table 3.1.5 – Overlapping interatomic distances in $\tau 8$

Atomic positions	Distance (Å)	Min. distance required (Å)
Al17a - Al17b	0.827	2.42
Al17a - Al18d	1.946	2.42
Al18a - Al18b	1.207	2.42
Al18a - Al18d	1.780	2.42
Al18b - Al18c	1.461	2.42
Al19a - Al19b	1.279	2.42

Accordingly, the following occupation equations are established:

$$Al19a + Al19b \leq 1$$
$$Al17a + A17b \leq 1$$
$$Al17a + Al18d \leq 1$$

Positions Al18a and Al18c do not overlap, as well as positions Al18b and Al18d. Therefore, these positions can exist simultaneously in the structure models. For a

realistic structural model, the occupations of overlapping Al18a-d positions should be equal to or less than 1. Using SC-XRD occupations from Table 3.1.2, this is the case for positions Al18b + Al18c and Al18c + Al18d:

$$Al18b + Al18c = 0.564 + 0.432 = 0.996$$
$$Al18c + Al18d = 0.432 + 0.560 = 0.992$$

Using SC-XRD occupations from Table 3.1.2, this is not the case for Al18a + Al18b and Al18a + Al18d:

$$Al18a + Al18b = 0.485 + 0.564 = 1.049$$
$$Al18a + Al18d = 0.485 + 0.560 = 1.045$$

Position Al18a is involved in both equations that generate an occupancy greater than 1. Therefore, Al in Al18a was substituted for Ge to create a new structural model using P-XRD date of sample AlFeGe6 with more realistic occupations. Without changing the occupations, this did not improve the R-factor of the Rietveld refinement. On the contrary: it increased from 2.804 to 2.854. However, refining the occupation of position 18a generates an R-factor of 2.804 and the refined occupation of Ge at position 18a is 0.208. Although the R-factor is not improved compared to the positioning of Al, it does enable more realistic occupations, as the occupations of overlapping positions are less than one:

$$Ge18a + Al18b = 0.208 + 0.564 = 0.772$$
$$Ge18a + Al18d = 0.208 + 0.560 = 0.768$$

Overall, the occupation of positions 18a-d would decrease from 2.041 to 1.764 with Ge in position 18a. The calculated composition with Al on position 18a is Al71.53 Fe9.49 Ge18.98 and with Ge on position 18a is Al71.18 Fe9.52 Ge19.30. The model with Ge on position 18a fits better to the mean composition of Al70.76 Fe9.46 Ge19.78 determined by SEM and hence was used for the P-XRD refinements in Table 3.1.1. The refined P-XRD pattern of $\tau 8$ in sample AlFeGe 6 is shown in Figure 3.1.13.

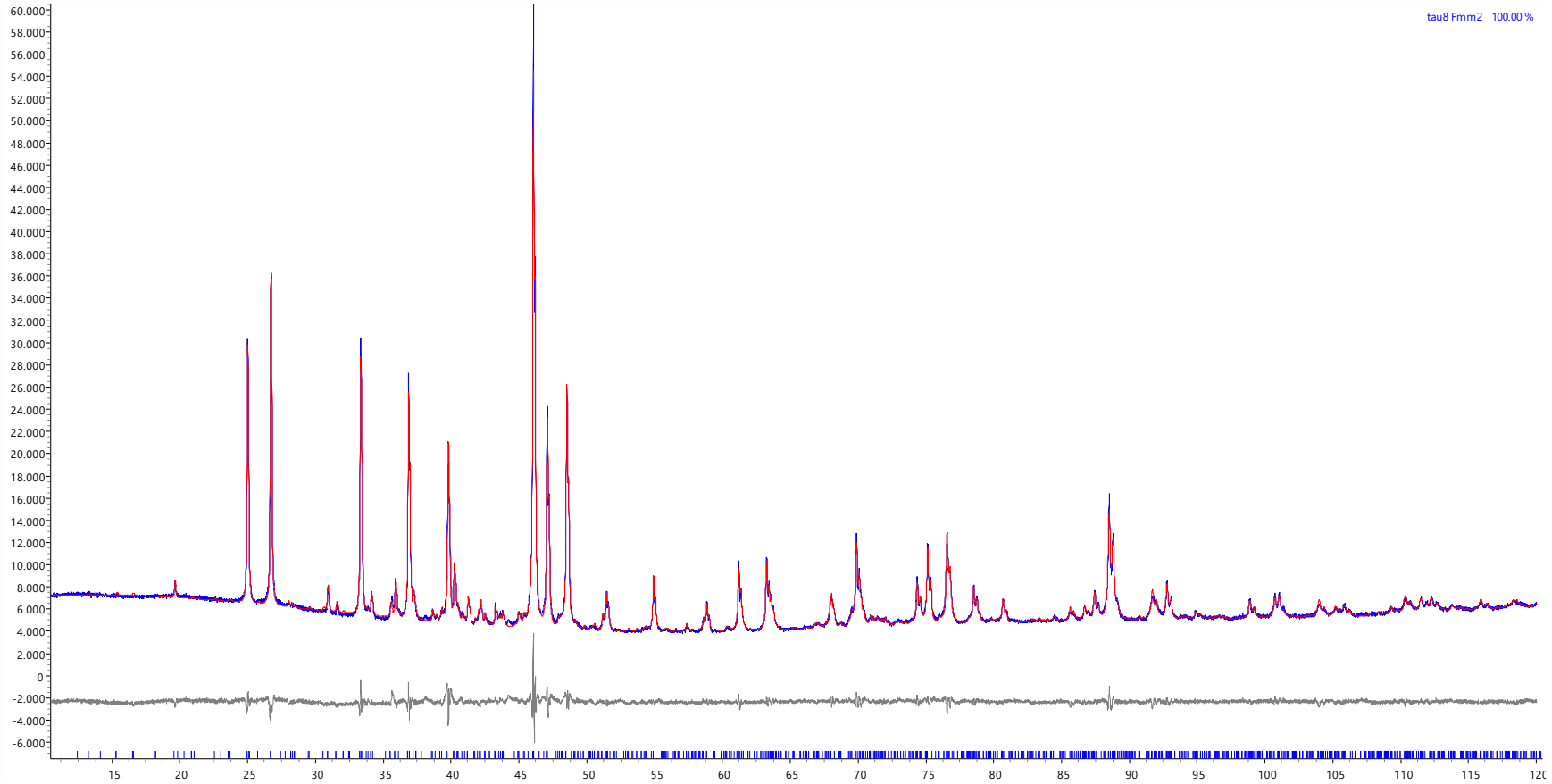

Figure 3.1.13 - Refined P-XRD pattern of sample AlFeGe 6

The coordination models of each atomic position in $\tau 8$ with Ge on position 18a are shown in Figure 3.1.14:

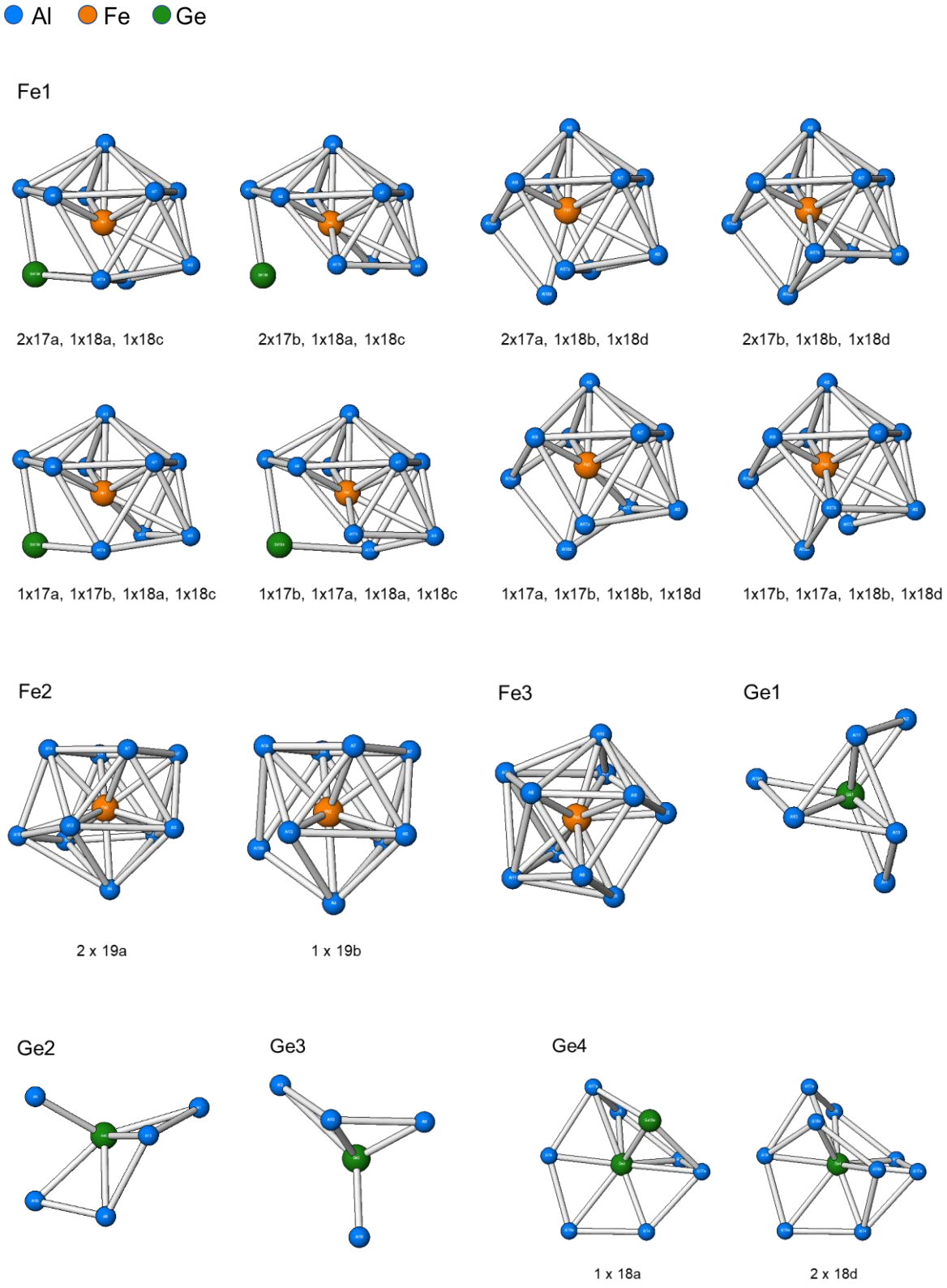

Ge5

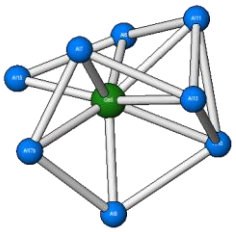

Ge6

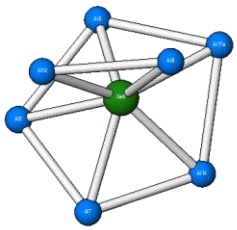

1 x 17a

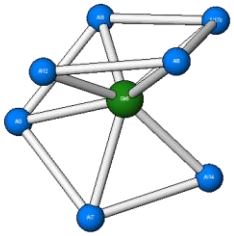

1 x 17b

Al1

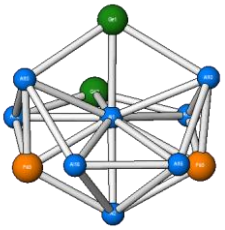

Al2

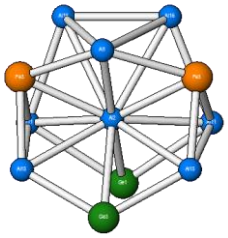

Al3

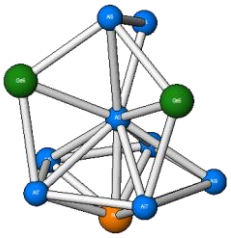

Al4

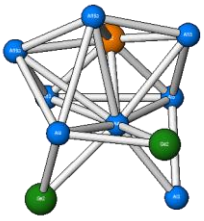

2 x 19a

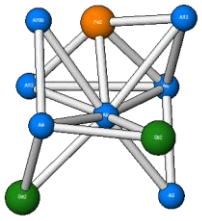

1 x 19b

Al5

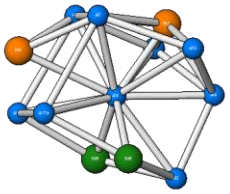

2 x 17a

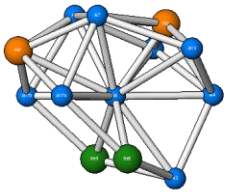

2 x 17b

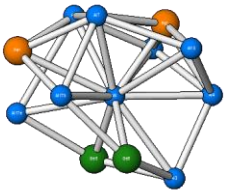

1 x 17a, 1 x 17b

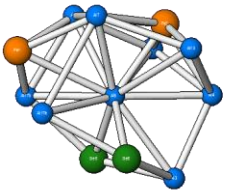

1x 17b, 1x 17a

Al6

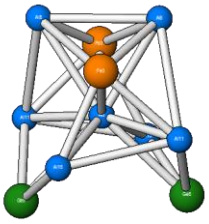

Al7

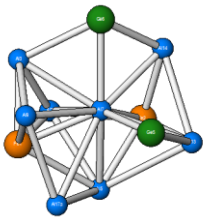

1 x 17a

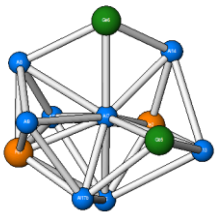

1 x 17b

Al8

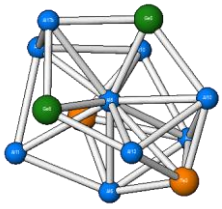

Al9

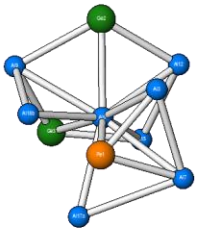

1 x 17a, 1 x 18b

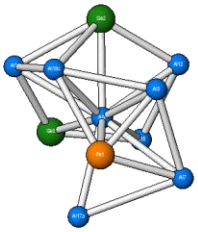

1 x 17a, 1 x 18c

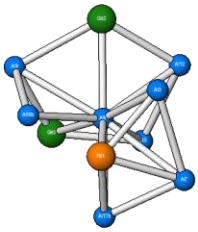

1 x 17b, 1 x 18b

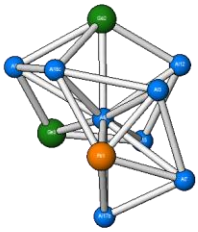

1 x 17b, 1 x 18c

Al10

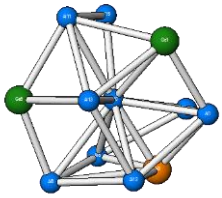

Al11

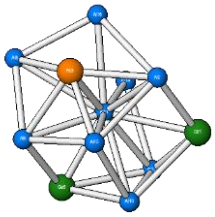

Al12

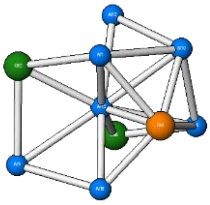

Al13

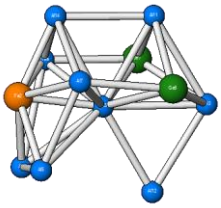

Al14

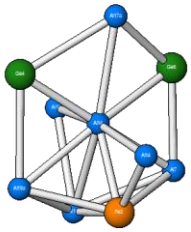

1 x 17a, 1 x 19a

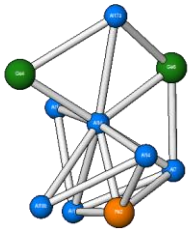

1 x 17a, 1 x 19b

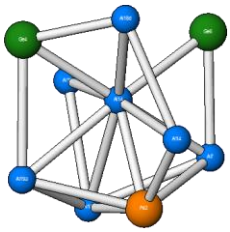

1 x 18d, 1 x 19a

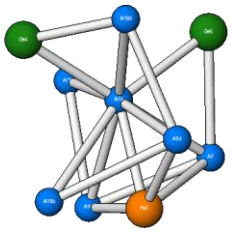

1 x 18d, 1 x 19b

Al15

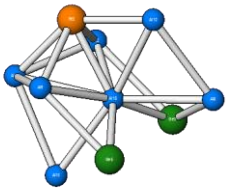

Al16

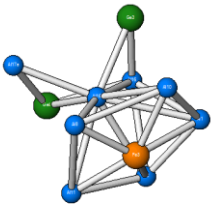

1 x 17a

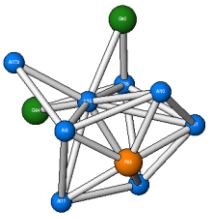

1 x 17b

Al17a

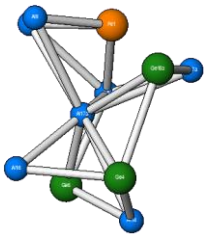

Minus 1 x 17b, 1 x 18d

Al17b

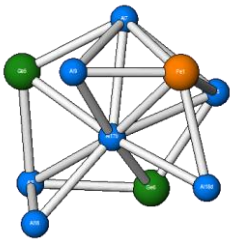

Minus 1 x 17a

Ge18a

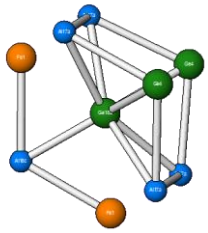

Minus 1 x 18b, 2 x 18d

Al18b

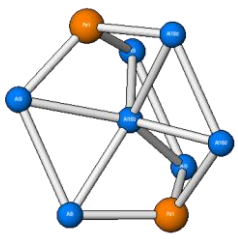

Minus 1 x 18a, 1 x 18c

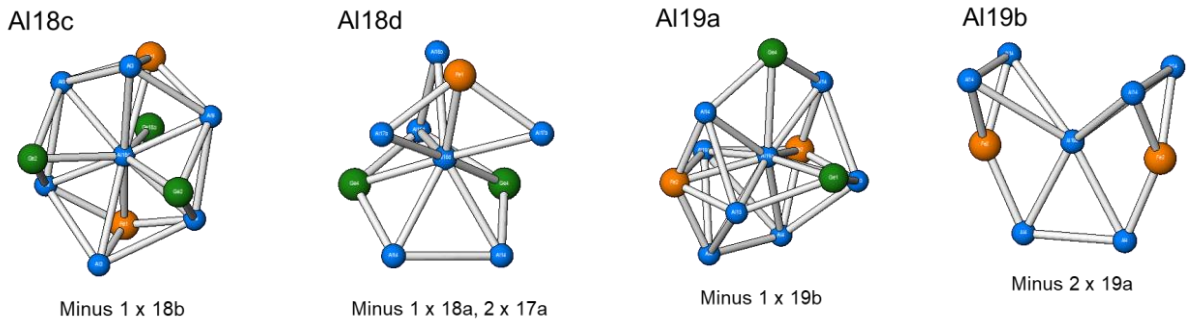

Figure 3.1.14 - Coordination models of atomic positions in τ8 with Ge on position 18a

The possible occupations of atoms in positions Al17a – Al19b influences the structure of certain independent atomic positions. In positions Fe2 and Al4 the occupation of Al19a and Al19b influences the coordination number, where it can be nine or ten. Some independent positions retain the same structure regardless of the variations in Al17a – Al19b occupations, while the structure of other independent positions vary depending on the occupation of positions Al17a – 19b. Position Fe1 with eight structural variations is influenced the most by variations in Al17a – Al19b occupation. In short-range order, it is possible to determine the structure in the independent atomic positions. For example, occupation of Al17a must result in structures containing Al17a in the coordination polyhedrons of positions Ge6, Al5, Al7 and Al16. The unit cell of τ8 is shown in Figure 3.1.15:

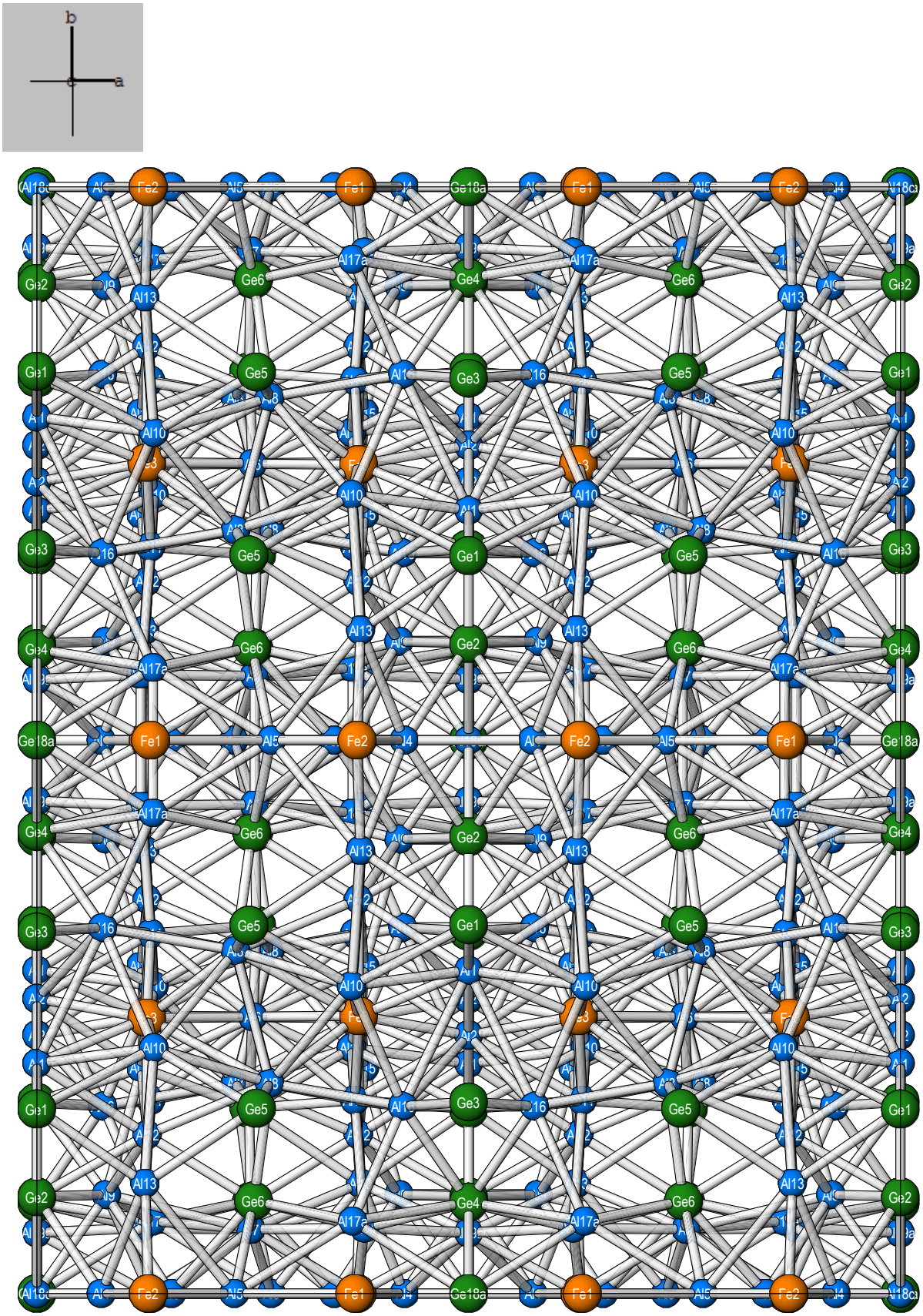

Figure 3.1.15 – Unit cell of $\tau 8$

3.2. Au-Si-Ti

The prepared samples, their phases, lattice parameters as well as compositions determined by P-XRD and SEM are listed in Table 3.2.1. The melting temperature of T2 was determined to be 1164.8 °C by DTA using sample AuSiTi1 a, shown in the first cycle in Figure 3.2.1. Therefore, subsequent samples were annealed at 1100 °C, as close to the melting point as possible.

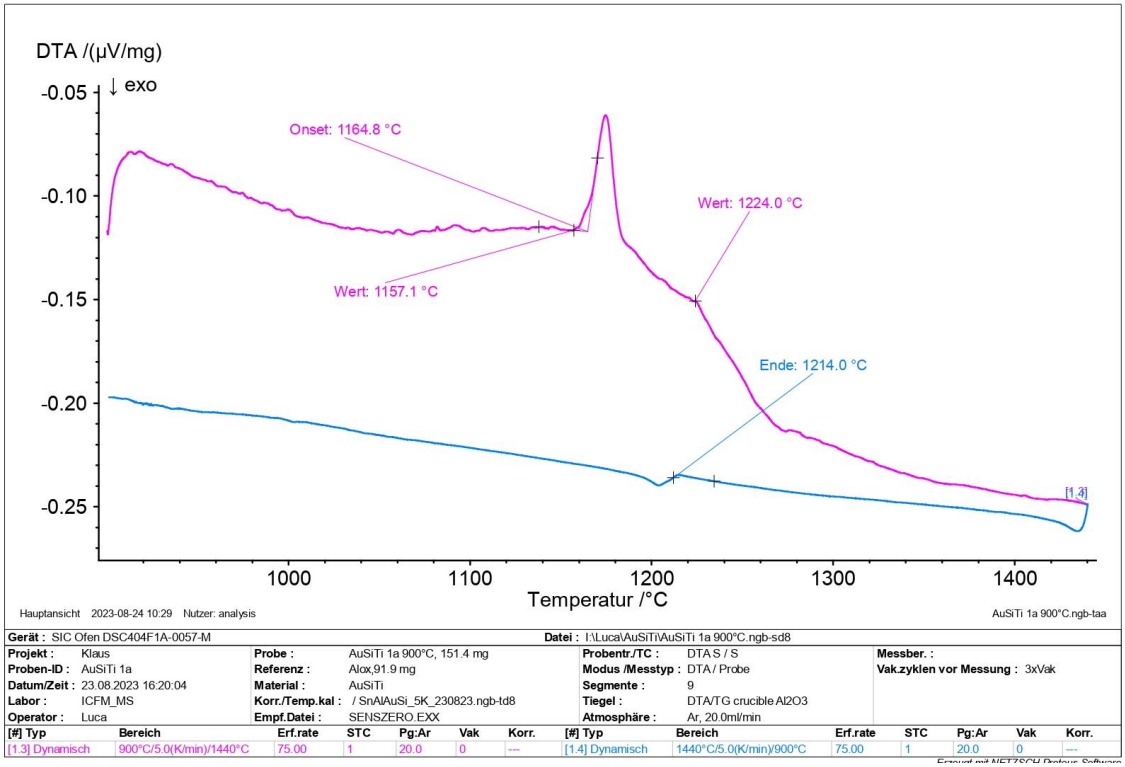

Figure 3.2.1 –DTA cycle 1 of sample AuSiTi 1a

The SEM images are shown in Figures 3.2.2 and 3.2.3. A crystal of size 65 µm from sample AuSiTi 3 was selected for SC-XRD and the collected data are listed in Tables 3.2.2 – 3.2.4. The refined P-XRD pattern of sample 3 is shown in Figure 3.2.4.

Table 3.2.1 – Au-Si-Ti samples, their phases, lattice parameters and compositions determined by P-XRD and SEM

							Composition from P-XRD (at. %)				Composition from SEM (at. %)		
Sample	(Au/Si/Ti)	Phase	Fraction (%)	a (Å)	b (Å)	c (Å)	Au	O	Si	Ti	Au	Si	Ti
3	(33.0/26.0/41.0)	Au_2Ti	4	3.419	-	8.521	67	-	-	33	67.76 ± 1.15	-	32.24 ± 1.15
		T2	96	16.177	-	-	32	-	29	39	33.54 ± 0.91	25.13 ± 0.46	41.34 ± 0.45
5	(33.5/25.1/41.4)	Au_2Ti	25	3.421	-	8.514	67	-	-	33	67.28 ± 0.60	-	32.72 ± 0.60
		Si_4Ti_5	37	6.713	-	12.196	-	-	44	56	0.14 ± 0.04	44.18 ± 0.04	55.67 ± 0.08
		T2	38	16.179	-	-	32	-	29	39	32.93 ± 0.09	25.47 ± 0.16	41.60 ± 0.25
6	(33.2/25.3/41.5)	Au	21	4.076	-	-	100	-	-	-	-	-	-
		Au_4Ti	13	6.285	-	3.968	80	-	-	20	81.21 ± 0.44	-	18.79 ± 0.44
		Si	1	5.946	-	-	-	-	100	-	-	-	-
		Si_3Ti_5O	42	7.423	-	5.156	-	11	33	56	-	37.66 ± 0.59	62.34 ± 0.59
		T1	16	11.620	9.670	14.139	40	-	24	36	43.70 ± 1.72	21.59 ± 0.86	34.71 ± 0.89
		T2	7	16.176	-	-	32	-	29	39	34.00 ± 0.53	25.80 ± 0.24	40.20 ± 0.77

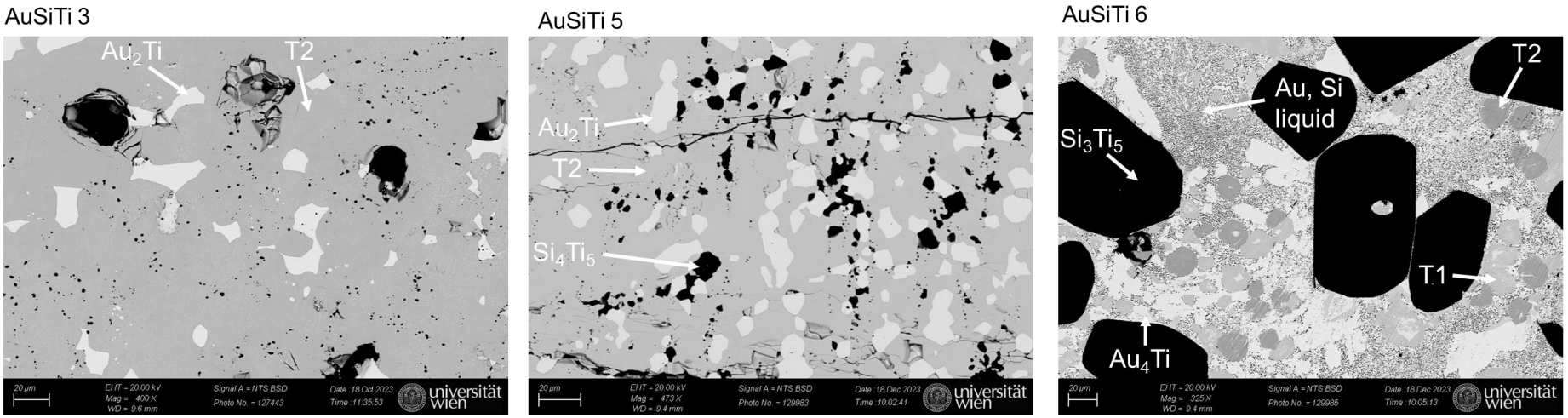

Figure 3.2.2 – SEM images of samples AuSiTi 3,5 and 6

Table 3.2.2 - Sites, occupation, multiplicity and coordinates of T2

Atom	Occ.	Wyckoff letter	Site symmetry	*x*	*y*	*z*	U_{equiv}	U_{11}	U_{22}	U_{33}	U_{23}	U_{13}	U_{12}
Au1	$Au_{0.8662(16)}$	16(*c*)	.3.	0.259786(17)	= *x*	= *x*	0.00563(10)	0.00563(10)	= U_{11}	= U_{11}	0.00101(8)	= U_{23}	= U_{23}
Au2	Au_1	24(*d*)	2..	0.277800(18)	0	1/4	0.00717(6)	0.00960(13)	0.00657(13)	0.00533(14)	-0.00137(14)	0	0
Au3	Au_1	48(*e*)	1	0.126801(15)	0.121220(13)	0.247413(15)	0.00751(5)	0.00658(9)	0.00823(9)	0.00772(10)	0.00129(10)	-0.00079(9)	-0.00140(8)
Ti1	Ti_1	12(*b*)	$\bar{4}$..	7/8	0	1/4	0.0044(3)	0.0042(7)	0.0045(4)	= U_{11}	0	0	0
Ti2	Ti_1	48(*e*)	1	0.01577(7)	0.38836(7)	0.14672(7)	0.00672(19)	0.0079(5)	0.0067(5)	0.0056(4)	0.0001(3)	0.0010(4)	-0.0002(4)
Ti3	Ti_1	48(*e*)	1	0.01867(7)	0.39678(7)	0.36152(7)	0.00526(18)	0.0057(5)	0.0049(5)	0.0051(5)	-0.0006(3)	-0.0004(3)	0.0004(3)
Si1	Si_1	24(*d*)	2..	0.03707(13)	0	1/4	0.0050(3)	0.0040(9)	0.0057(10)	0.0052(9)	0.0007(10)	0	0
Si2	Si_1	48(*e*)	1	0.12528(10)	0.33849(9)	0.25861(11)	0.0048(3)	0.0042(6)	0.0044(6)	0.0058(7)	-0.0001(6)	0.0000(6)	-0.0007(6)

Table 3.2.3 – Bond lengths of T2

Bond	Distance (Å)	Multiplicity
Au1−Si2	2.5191(16)	3x
Au1−Ti2	2.7891(11)	3x
Au1−Ti3	2.8061(10)	3x
Au1−Au3	3.1106(5)	3x
Au1−Ti2	3.1340(13)	1x
Au1−Si2	3.5165(15)	1x
Au2−Si2	2.4982(16)	2x
Au2−Ti3	2.7477(11)	2x
Au2−Au3	2.9621(2)	2x
Au2−Ti3	2.9865(13)	2x
Au2−Ti2	3.0910(11)	2x
Au2−Au3	3.1299(3)	2x
Au2−Au2	3.1422(6)	1x
Au3−Si1	2.4379(13)	1x
Au3−Si2	2.5906(17)	1x
Au3−Au3	2.8229(4)	2x
Au3−Ti2	2.8254(11)	1x
Au3−Ti2	2.8633(11)	1x
Au3−Ti3	2.9103(11)	1x
Au3−Au2	2.9621(2)	1x
Au3−Ti3	3.0024(11)	1x
Au3−Au1	3.1105(5)	1x
Au3−Au2	3.1299(3)	1x
Si1−Au3	2.4379(13)	2x
Si1−Ti2	2.6023(13)	2x
Si1−Ti3	2.6162(14)	2x
Si1−Ti1	2.620(2)	1x
Si1−Ti2	2.8647(17)	2x
Si2−Au2	2.4982(16)	1x
Si2−Au1	2.5191(16)	1x
Si2−Ti3	2.573(2)	1x
Si2−Au3	2.5906(17)	1x
Si2−Ti2	2.600(2)	1x
Si2−Ti1	2.6141(15)	1x
Si2−Ti3	2.619(2)	1x
Si2−Ti2	2.656(2)	1x
Si2−Ti3	2.743(2)	1x
Ti1−Si2	2.6141(15)	4x
Ti1−Si1	2.620(2)	2x
Ti1−Ti3	2.9977(13)	4x
Ti1−Si2	3.0264(13)	4x
Ti2−Si2	2.600(2)	1x

Table 3.1.2 (continued) – Bond lengths of T2

Bond	Distance (Å)	Multiplicity
Ti2−Si1	2.6023(13)	1x
Ti2−Si2	2.656(2)	1x
Ti2−Au1	2.7891(11)	1x
Ti2−Au3	2.8254(11)	1x
Ti2−Au3	2.8633(11)	1x
Ti2−Si1	2.8647(17)	1x
Ti2−Ti1	3.0264(13)	1x
Ti2−Ti3	3.0549(16)	1x
Ti2−Au2	3.0910(11)	1x
Ti2−Au3	3.1340(13)	1x
Ti2−Ti2	3.385(2)	2x
Ti2−Ti3	3.4747(13)	1x
Ti2−Ti3	3.4756(14)	1x
Ti2−Ti3	3.4840(13)	1x
Ti3−Si2	2.573(2)	1x
Ti3−Si1	2.6162(14)	1x
Ti3−Si2	2.619(2)	1x
Ti3−Si2	2.743(2)	1x
Ti3−Au2	2.7477(11)	1x
Ti3−Au1	2.8061(10)	1x
Ti3−Au3	2.9103(11)	1x
Ti3−Au2	2.9865(13)	1x
Ti3−Ti1	2.9977(13)	1x
Ti3−Au3	3.0024(11)	1x
Ti3−Ti2	3.0549(16)	1x
Ti3−Ti3	3.4099(18)	2x
Ti3−Ti2	3.4747(13)	1x
Ti3−Ti2	3.4756(14)	1x
Ti3−Ti2	3.4840(13)	1x

Table 3.2.4 – SC-XRD data of T2

Sample	AuSiTi 3
Phase notation	T2
Compound	$Au_{8-x}Si_6Ti_9$ (x ~ 0.9)
Structure type	own
Pearson symbol	*cI*268
a (Å)	16.16 (2)
b (Å)	-
c (Å)	-
Space group	$I\bar{4}3d$
V (Å^3) / Z	4222 (2) / 12
ρ_{calc} (g cm^{-3}) / μ(Mo Kα) (mm^{-1})	9.49 / 80
Crystal dimensions (μm)	6 x 7 x 65
Range of data collection (±h ±k ±l) (°)	3 < 2θ < 70
Number of images / rotation angle per image (°)	1407 / 0.5
Scans / scan time (s / °)	16 / 10
Measured reflections	87377
Unique reflections (n) / reflections with $F_o > 4\sigma(F_o)$	1561 / 1432
$R_{int} = \sum\lvert F_o^2 - F_o^2(mean)\rvert \,/\, \sum F_o^2$	0.110
Extinction parameter k $F_c^* = F_c k[1 + 0.001F_c^2\lambda^3 \,/\, \sin 2\theta]^{-\frac{1}{4}}$	0.0000266 (10)
$R1 = \sum\left(\lvert\lvert F_0^2\rvert - \lvert F_c^2\rvert\rvert\right)^2 \,/\, \sum F_o$ (observed / all reflections)	0.0253 / 0.0188
$\omega R2 = [\sum \omega\,(F_0^2 - F_c^2)^2 \,/\, \sum \omega F_0^4]^{\frac{1}{2}}$	0.033
$GooF = [\sum \omega\,(F_0^2 - F_c^2)^2 \,/\, (n-p)]^{\frac{1}{2}}$	1.09
Variable parameters / weighting parameter *a*, *b*	55 / 0.0071, 55.6
Final difference Fourier map (eÅ^{-3})	-1.20 to +1.89

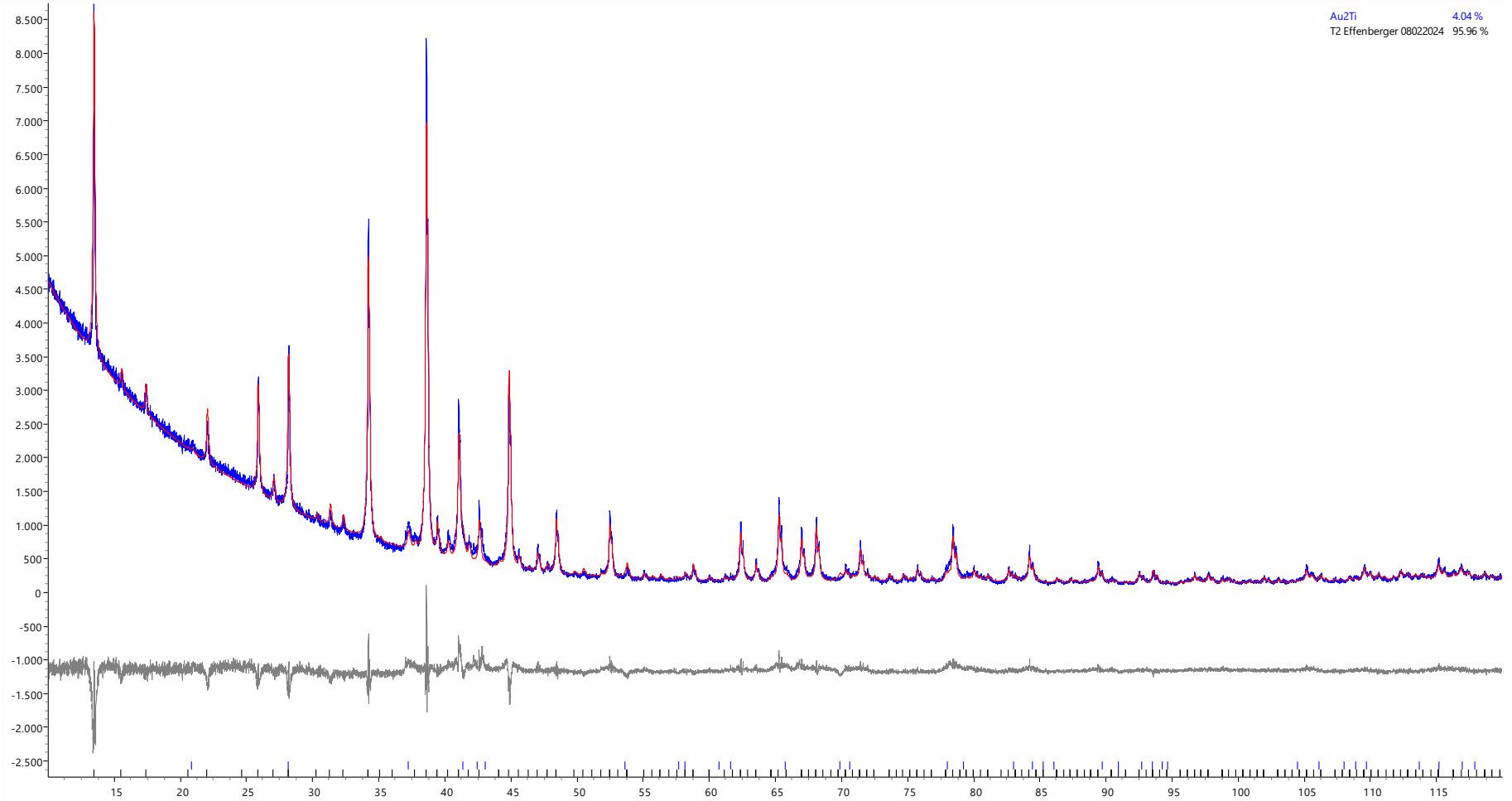

Figure 3.2.4 - Refined P-XRD pattern of sample AuSiTi3

Phase T2 is cubic of structure type *I43d* and the formula of T2 is $Au_{8-x}Si_6Ti_9$ (x ~ 0.9). The unit cell of T2 consists of 88 Au atoms, 72 Si atoms and 108 Ti atoms, totalling 268 atoms in the unit cell. There are 8 independent atomic positions and the coordination models of the independent positions are shown in Figure 3.2.5:

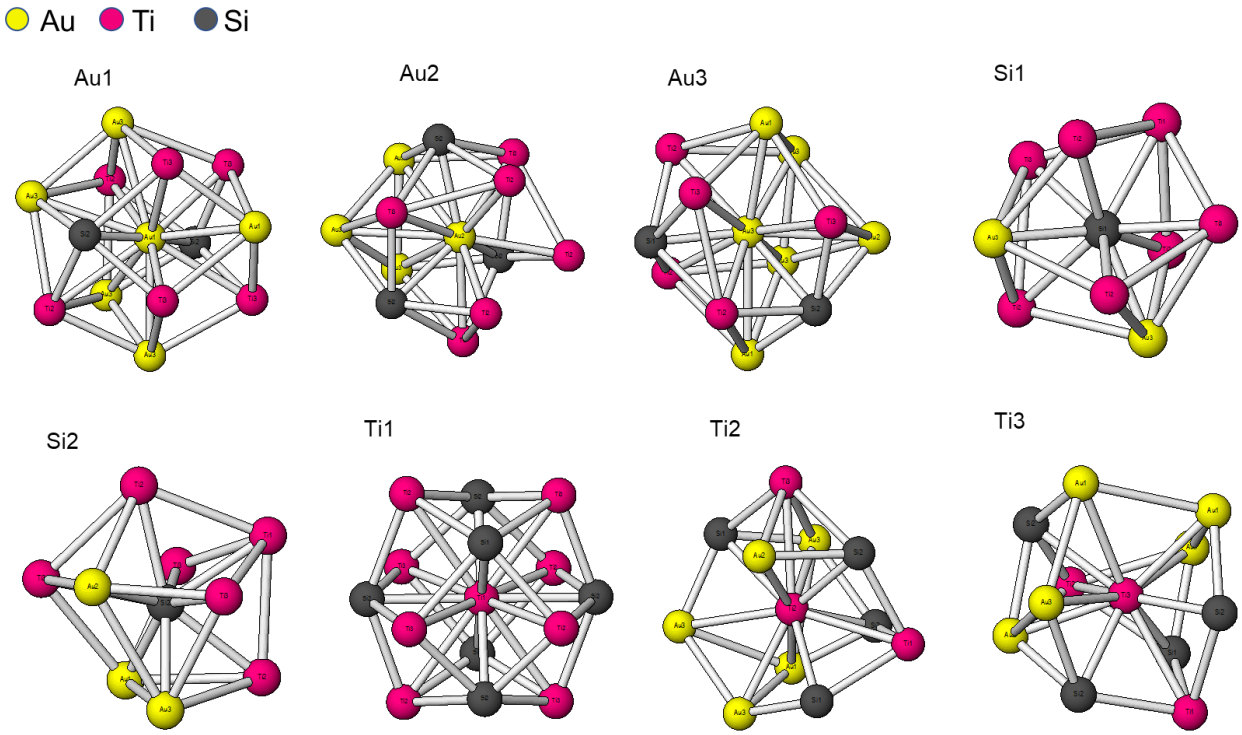

Figure 3.2.5 – Coordination models of atomic positions in T2

In comparison, structure T1 has 9 independent atomic positions, shown in Figure 3.2.6.

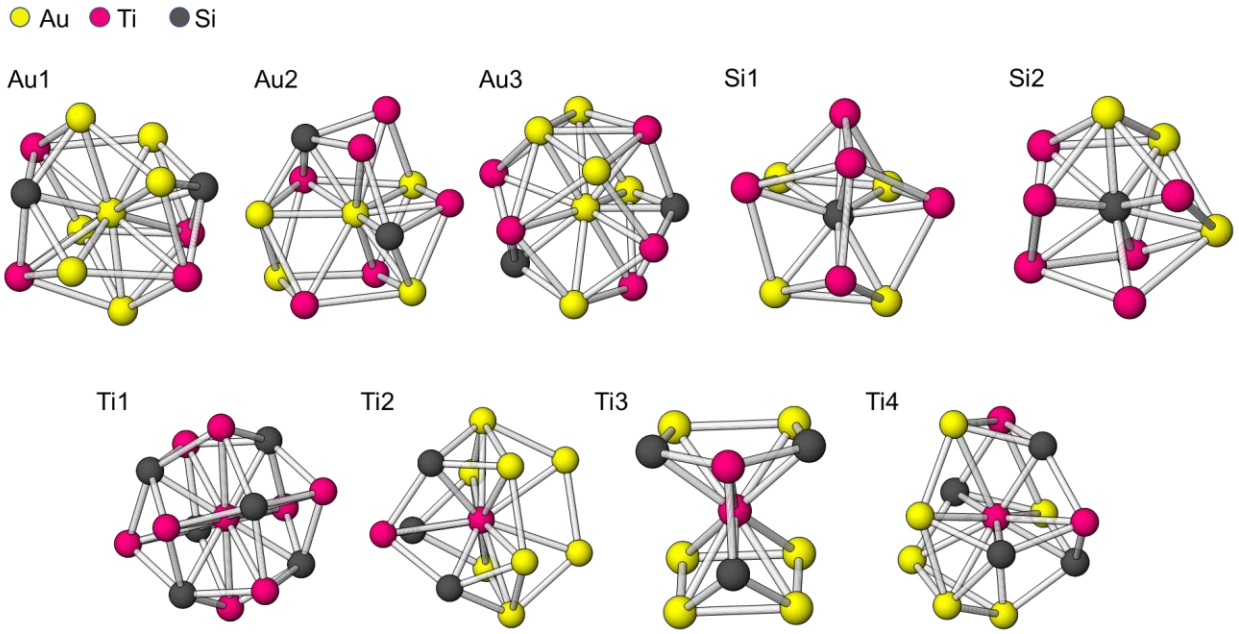

Figure 3.2.6 – Coordination models of atomic positions in T1

Phase T1 has formula $Au_{10}Si_6Ti_9$ and the unit cell consists of 40 Au, 24 Si and 36 Ti atoms (33). The polyhedrons in position Ti1 is identical in phases T1 and T2. As in T1, the T2 structure contains Ti1 polyhedrons surrounded by a network of Au atoms. A structure of the polyhedron in position Ti1 shown in Figure 3.2.7:

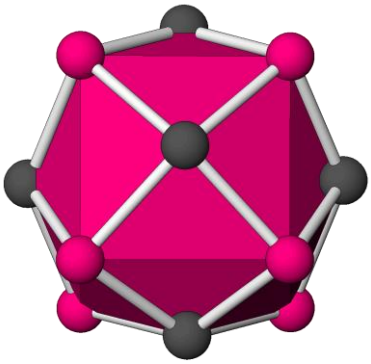

Figure 3.2.7 – Polyhedron in position Ti1

The bond lengths in the polyhedron are between 2.5659 Å (Si2 to Ti3) and 3.0235 Å (Ti1 to Ti2) in T2, compared to between 2.56 Å and 3.00 Å in T1 (33). The polyhedrons are distributed orderly throughout the T2 structure, shown in Figure 3.2.8:

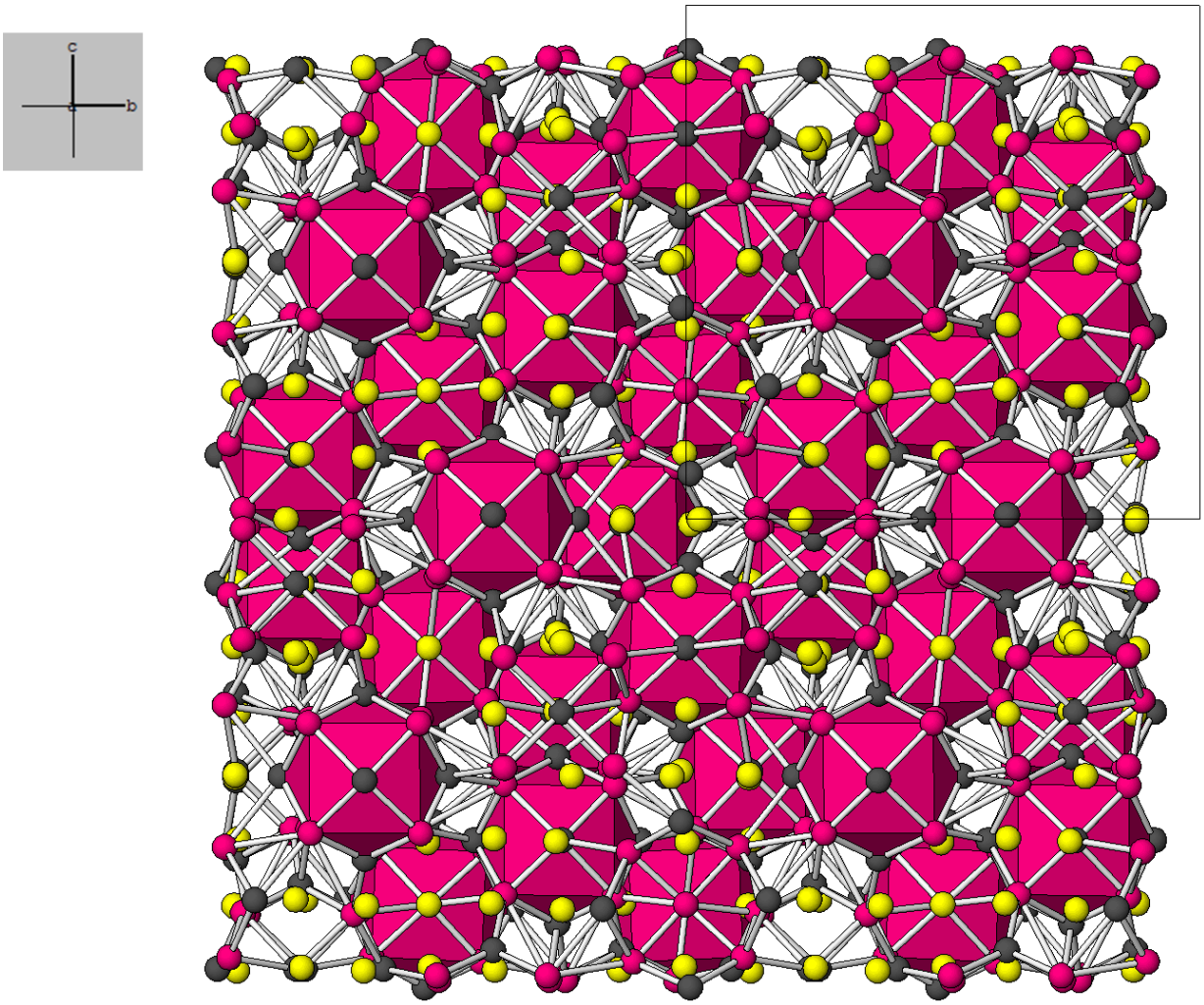

Figure 3.2.8 – Structure of T2

In T1 the polyhedrons are not connected (33), whereas in T2 they are connected between Si1-Ti2 and Si2-Ti3. The different bond lengths were calculated using ATOMS V6.3.4 © by Shape Software and are presented in Table 3.2.5. The average distance between the Au atoms in T2 is about 3.034 Å (using bond lengths from Table 3.2.5) compared to about 2.80 Å in T1 (33). This also leads to a denser arrangement of Si-Ti polyhedrons in T2 compared to T1.

Additional to structure T2, an oxygen-stabilized variation of Si_3Ti_5 with formula Si_3Ti_5O was discovered in sample AuSiTi6 using SC-XRD. The phase is hexagonal of structure type *P63/mcm*. The bond lengths of Si_3Ti_5O are listed in Table 3.2.6. The sites, occupation, multiplicity and fractional occupation parameters are listed in Table 3.2.7. Refined P-XRD patterns are shown in Figures 3.2.9 and 3.2.10.

Table 3.2.6 – Bond lengths of Si_3Ti_5O

Bond	Distance (Å)	Multiplicity
Ti1−Ti1	2.5715(3)	2x
Ti1−Si	2.5963(2)	6x
Ti1−Ti2	3.1749(3)	6x
Ti2−O	2.1821(3)	2x
Ti2−Si	2.6310(4)	2x
Ti2−Si	2.6479(5)	1x
Ti2−Si	2.8641(3)	2x
Ti2−Si	3.0537(5)	2x
Ti2−Ti2	3.1178(3)	4x
Ti2−Ti1	3.1749(3)	4x
Si−Ti1	2.5963(2)	4x
Si−Ti2	2.6310(4)	2x
Si−Ti2	2.6479(5)	1x
Si−Ti1	2.8641(3)	2x
Si−Si	2.9216(5)	2x
Si−O	3.2862(5)	2x
O−Ti2	2.1821(3)	6x
O−O	2.5715(3)	2x
O−Si	3.2862(5)	6x

Table 3.2.7 - Sites, occupation, multiplicity and coordinates of Si_3Ti_5O

Atom	Occupation	Wyckoff letter	Site symmetry	*x*	*y*	*z*	U_{equiv}	U_{11}	U_{22}	U_{33}	U_{23}	U_{13}	U_{12}
Ti1	1	4(*d*)	3.2	1/3	2/3	0	0.00582(7)	0.00616(11)	= U_{11}	0.00513(11)	0	0	= 0.5 * U_{11}
Ti2	1	6(*g*)	*m2m*	0.23709(5)	0	1/4	0.00628(7)	0.00583(8)	0.00571(10)	0.00724(10)	0	0	= 0.5 * U_{22}
Si	1	6(*g*)	*m2m*	0.59325(5)	0	1/4	0.00693(8)	0.00580(12)	0.00537(15)	0.00950(14)	0	0	= 0.5 * U_{22}
O	0.961(4)	2(*b*)	$\bar{3}.m$	0	0	0	0.0071(3)	0.0073(4)	= U_{11}	0.0065(6)	0	0	= 0.5 * U_{22}

Table 3.2.7 – SC-XRD data of Si_3Ti_5O

Sample	AuSiTi 6
Phase notation	Si_3Ti_5O
Compound	Si_3Ti_5O
Structure type	own
Pearson symbol	*hP*38
a (Å)	7.44 (8)
b (Å)	-
c (Å)	5.14 (6)
Space group	*P63/mcm*
V (Å^3) / Z	246.2 (2) / 2
ρ_{calc} (g cm^{-3}) / μ(Mo K$_\alpha$) (mm^{-1})	4.58 / 8.3
Crystal dimensions (μm)	6 x 75 x 75
Range of data collection (±h ±k ±l) (°)	3 < 2θ < 80
Number of images / rotation angle per image (°)	544 / 2
Scans / scan time (s / °)	10 / 110
Measured reflections	2028
Unique reflections (n) / reflections with $F_o > 4\sigma(F_o)$	310 / 286
$R_{int} = \sum\lvert F_o^2 - F_o^2(mean)\rvert \,/\, \sum F_o^2$	0.031
Extinction parameter k $F_c^* = F_c k[1 + 0.001F_c^2\lambda^3 \,/\, \sin 2\theta]^{-\frac{1}{4}}$	0.029 (3)
$R1 = \sum\left(\lvert\lvert F_0^2\rvert - \lvert F_c^2\rvert\rvert\right)^2 \,/\, \sum F_o$ (observed / all reflections)	0.0156 / 0.0140
$\omega R2 = [\sum \omega\,(F_0^2 - F_c^2)^2 \,/\, \sum \omega F_0^4]^{\frac{1}{2}}$	0.0337
$GooF = [\sum \omega\,(F_0^2 - F_c^2)^2 \,/\, (n-p)]^{\frac{1}{2}}$	1.05
Variable parameters / weighting parameters *a*, *b*	15 / 0.023, 0.00
Final difference Fourier map (eÅ^{-3})	-0.48 to +0.47

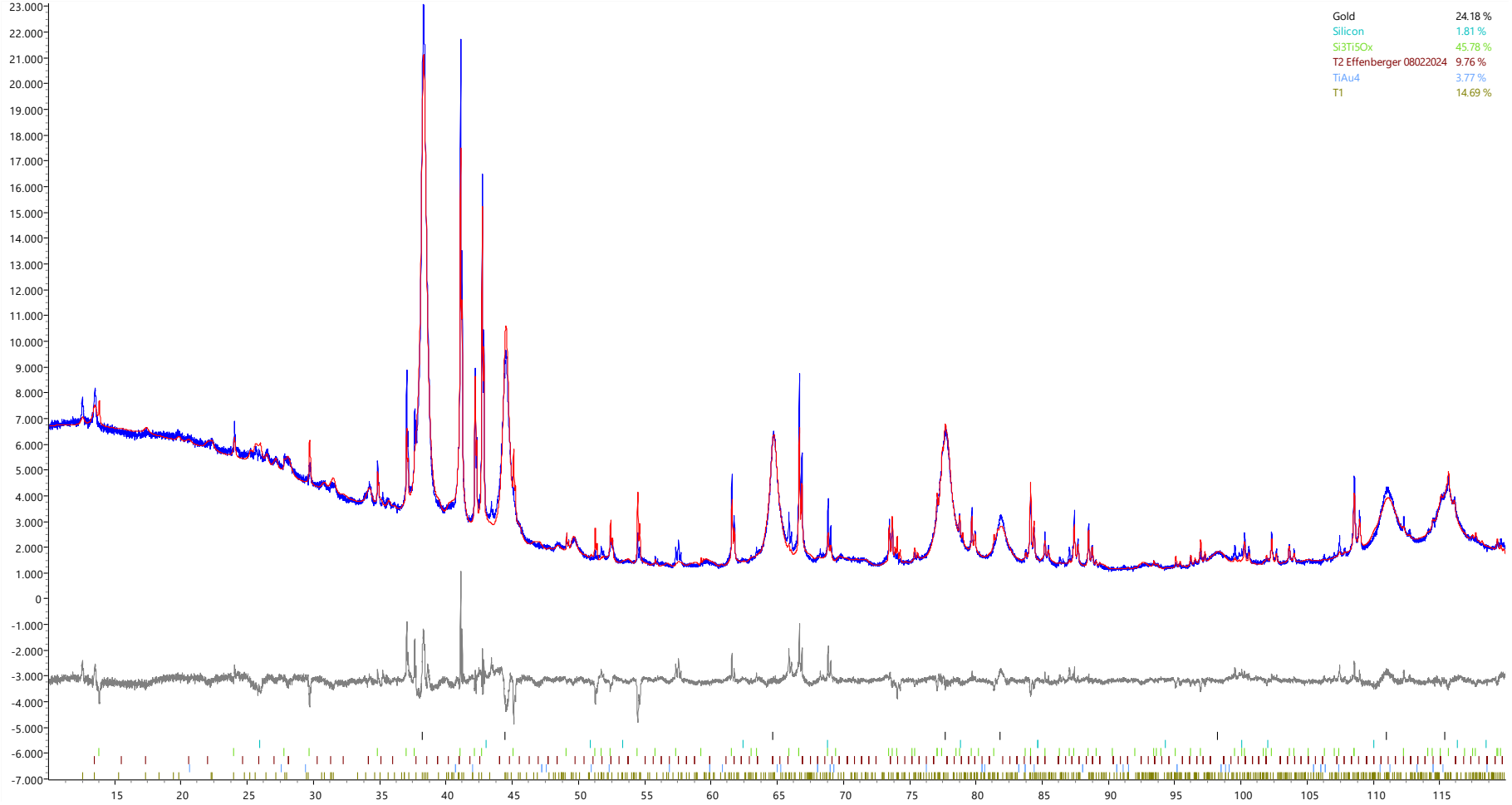

Figure 3.2.9 - Refined P-XRD pattern of sample AuSiTi 6 with O on position O1

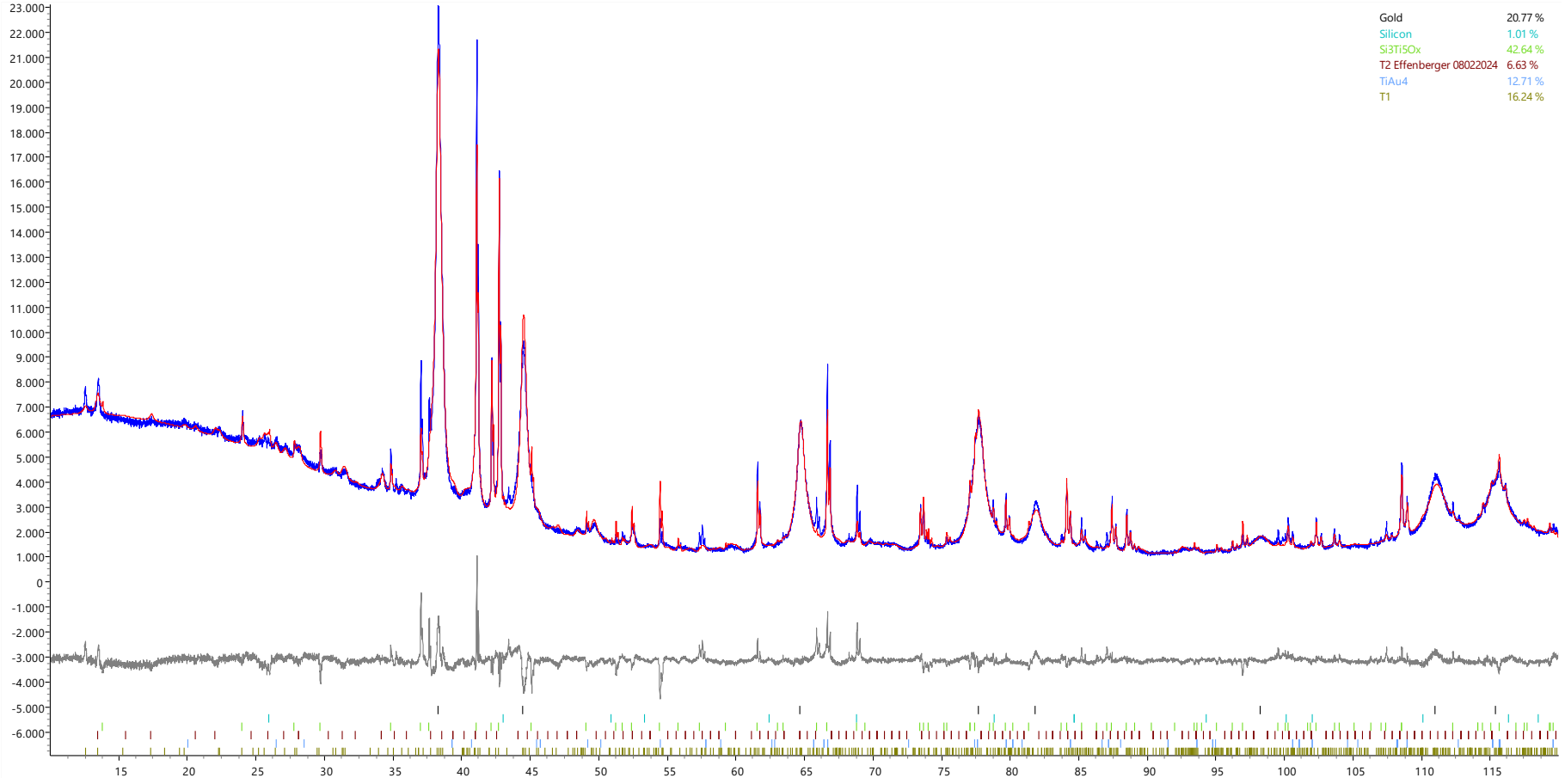

Figure 3.2.10 - Refined P-XRD pattern of sample AuSiTi 6 with Ti on position O1

SC-XRD revealed an oxygen occupancy of 0.961 on position O in Si_3Ti_5O (Table 3.2.6) and refinement in P-XRD revealed that the oxygen site has an occupancy of 1. However, P-XRD refinement was not optimal due to an additional model peak at 2θ = 13.80 (Figure 3.2.9.), meaning that the required electron density in the bulk sample in the Rietveld-model is higher. Occupying the position with Si does not fit the phase diagram and simultaneous occupation with Ti and O is not likely. However, in the Si-Ti phase diagram there is a known deviation of Ti in Si_3Ti_5 leaning towards the Ti-rich side (3). Therefore, a model was tested where oxygen in position O was exchanged for Ti. This improved the R-factor in the Rietvield refinement from 5.864 with O to 5.705 with Ti and reduced the peak at 2θ = 13.80 (Figure 3.2.10). The model revealed that Ti has an occupancy of 0.5315 in the O position, close to 50 % Ti statistically. The structures of Si_3Ti_5O with Ti, Si_3Ti_5O with O and Si_3Ti_5 are shown in Figures 3.2.11 – 3.2.13 respectively.

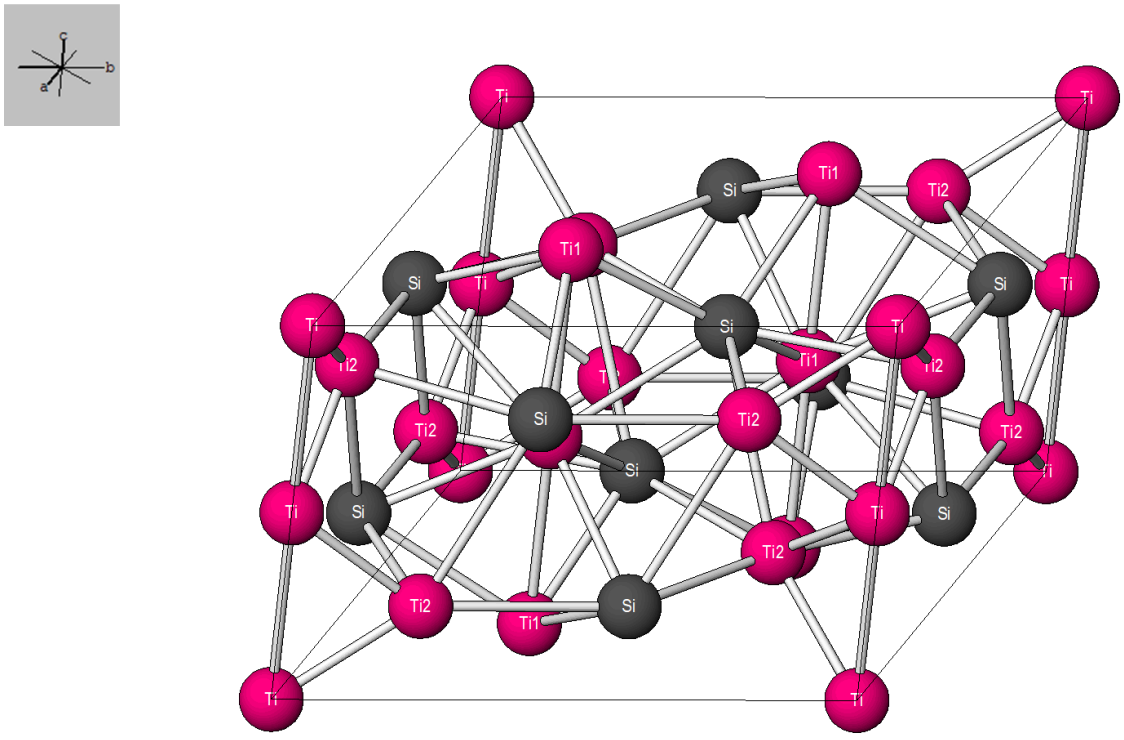

Figure 3.2.11 – Structure of Si_3Ti_5O with Ti

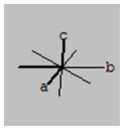

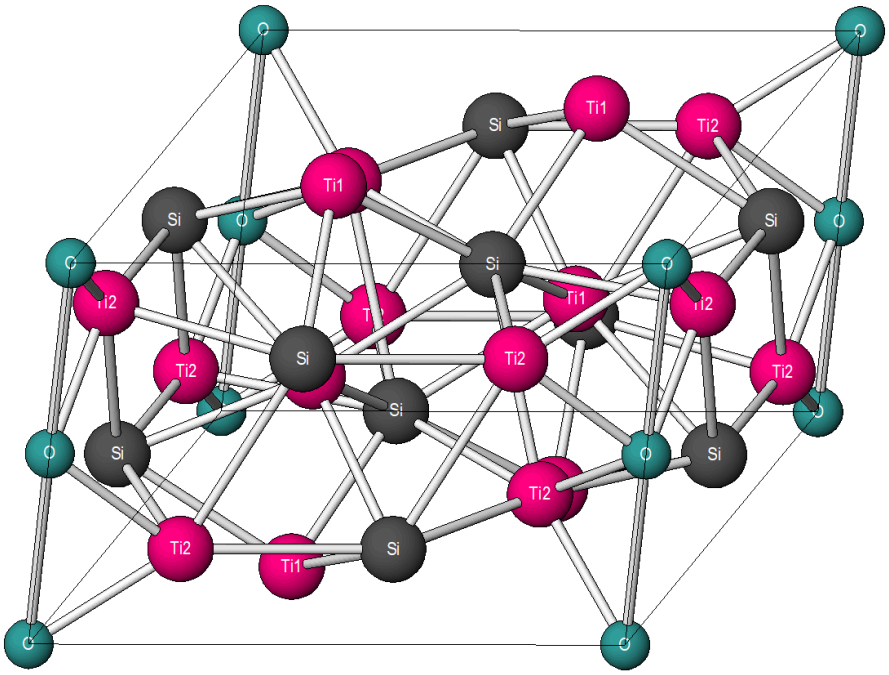

Figure 3.2.12 – Structure of Si_3Ti_5O with O

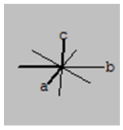

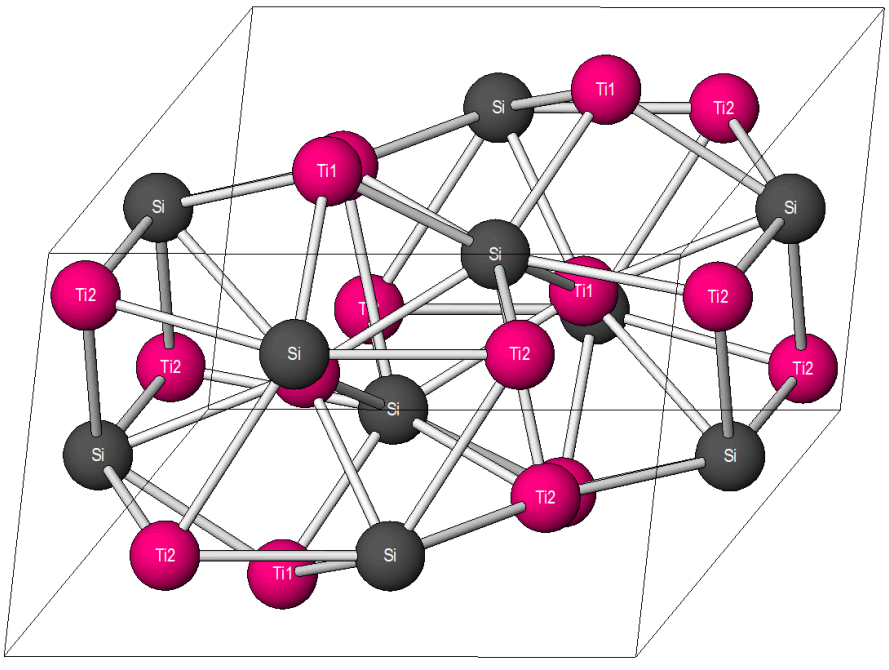

Figure 3.2.13 – Structure of Si_3Ti_5

Structure Si_3Ti_5O and Si_3Ti_5 are both of space group *P63/mcm*. Compared to Si_3Ti_5, in Si_3Ti_5O oxygen is positioned in the corners of the unit cell and in-between the origin 0 and the c-axis. With Ti on position O, the structure is the same as Si_3Ti_5O, yet the oxygen positions are occupied with Ti. According to the improved model, structure with Ti is present in 50 % sample AuSiTi 6. This results in the formula $Si_3Ti_{5.5}$ and corresponds to 64.7 % Ti, which is the boundary composition of Si_3Ti_5 in the Si-Ti phase diagram (Figure 1.3.4). Therefore, it can be hypothesized that the crystal chosen for SC-XRD was Si_3Ti_5O, yet the bulk sample contains Ti-rich Si_3Ti_5 and the half-occupation is probably due to atomic distances.

3.3. Au-Ni-Sn

Previously, a structural model of the $(Au,Ni)_3Sn_2$ superstructure was created by Hans Flandorfer and Klaus Richter (45). This model of the $(Au,Ni)_3Sn_2$ superstructure, with formula $AuNi_2Sn_2$, was a good fit for the P-XRD diffractogram of sample AuNiSn 12. The crystallographic data of $AuNi_2Sn_2$ in sample AuNiSn 12 are presented in Tables 3.3.1. - 3.3.3 and the refined P-XRD pattern of sample AuNiSn 12 is shown in Figure 3.3.1.

Table 3.3.1 – Crystallographic data of $AuNi_2Sn_2$ in sample 12

Sample	AuNiSn 12
Phase notation	$AuNi_2Sn_2$
Compound	$AuNi_2Sn_2$
Structure type	own
Pearson symbol	*oP*22
a (Å)	5.303
b (Å)	4.152
c (Å)	7.190
Space group	*Pmma*

Table 3.3.2 - Sites, occupation, multiplicity and coordinates of $AuNi_2Sn_2$ in sample 12

Site	Atom	Occupation	Wyckoff letter	Site symmetry	*x*	*y*	*z*
Au 1	Au	0.63	2 (*b*)	.2/m.	0	0.5	0
	Ni	0.37			0	0.5	0
Ni 1	Au	0.11	2 (*c*)	.2/m.	0	0	0.5
	Ni	0.89			0	0	0.5
Ni 2	Ni	0.67	2 (*e*)	mm2	0.25	0	0.83
Sn 1	Sn	1	2 (*f*)	mm2	0.25	0.5	0.63
Sn 2	Sn	1	2 (*e*)	mm2	0.25	0	0.19

Table 3.3.3 – Bond lengths of $AuNi_2Sn_2$ in sample 12

Bond	Atoms	Length (Å)	Multiplicity
Au1-Au1	Au-Au	2.6500	x4
	Au-Ni	2.6500	x4
	Ni-Ni	2.6500	x4
Au1-Sn2	Au-Sn	2.8156	x8
	Ni-Sn	2.8156	x8
Au1-Ni2	Au-Ni	2.7487	x8
	Ni-Ni	2.7487	x8
Au1-Sn1	Au-Sn	2.9720	x4
	Ni-Sn	2.9720	x4
Ni1-Ni1	Ni-Ni	2.6500	x4
	Ni-Au	2.6500	x4
	Au-Au	2.6500	x4
Ni1-Ni2	Ni-Ni	2.7176	x8
	Au-Ni	2.7176	x8
Ni1-Sn1	Ni-Sn	2.6334	x8
	Au-Sn	2.6334	x8
Ni1-Sn2	Ni-Sn	2.5930	x8
	Au-Sn	2.5930	x8
Ni2-Sn1	Ni-Sn	2.5246	x4
Ni2-Sn2	Ni-Sn	2.6539	x4

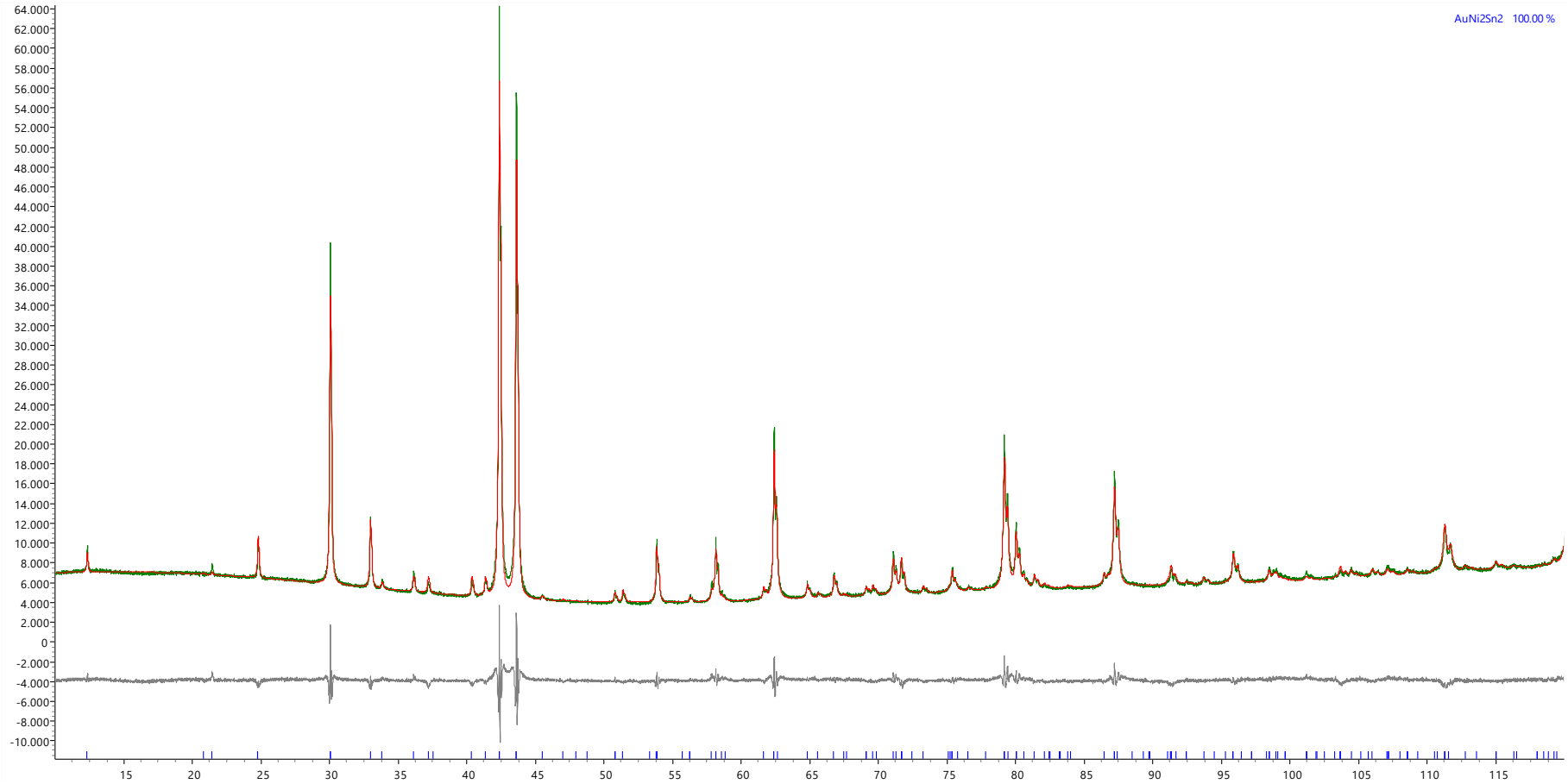

Figure 3.3.1 - Refined P-XRD pattern of sample AuNiSn 12

Visualisations of the crystal structures of $AuNi_2Sn_2$ and of (Au,Ni)3Sn2 are shown in Figures 3.3.2 – 3.3.6.

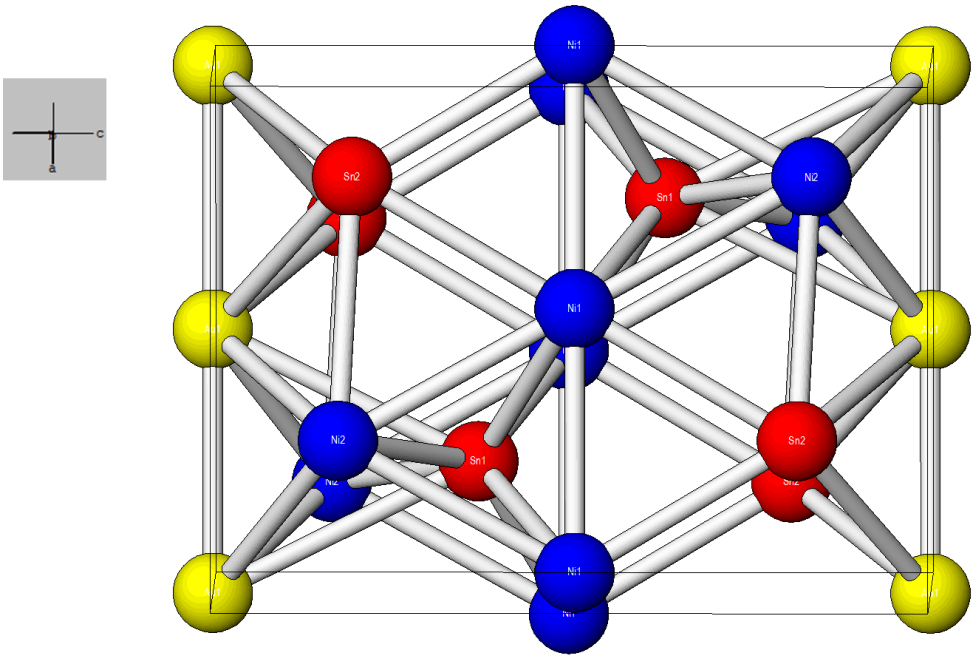

Figure 3.3.2 – Unit cell of $AuNi_2Sn_2$ with Au on position Au1 and Ni on position Ni1

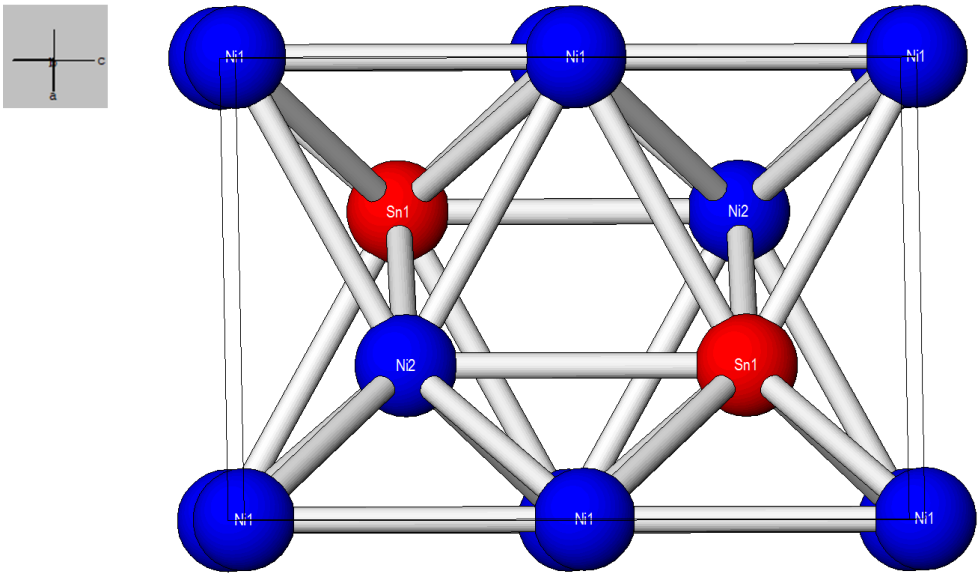

Figure 3.3.3 – Unit cell of $(Au,Ni)_3Sn_2$ with Ni on position Ni1

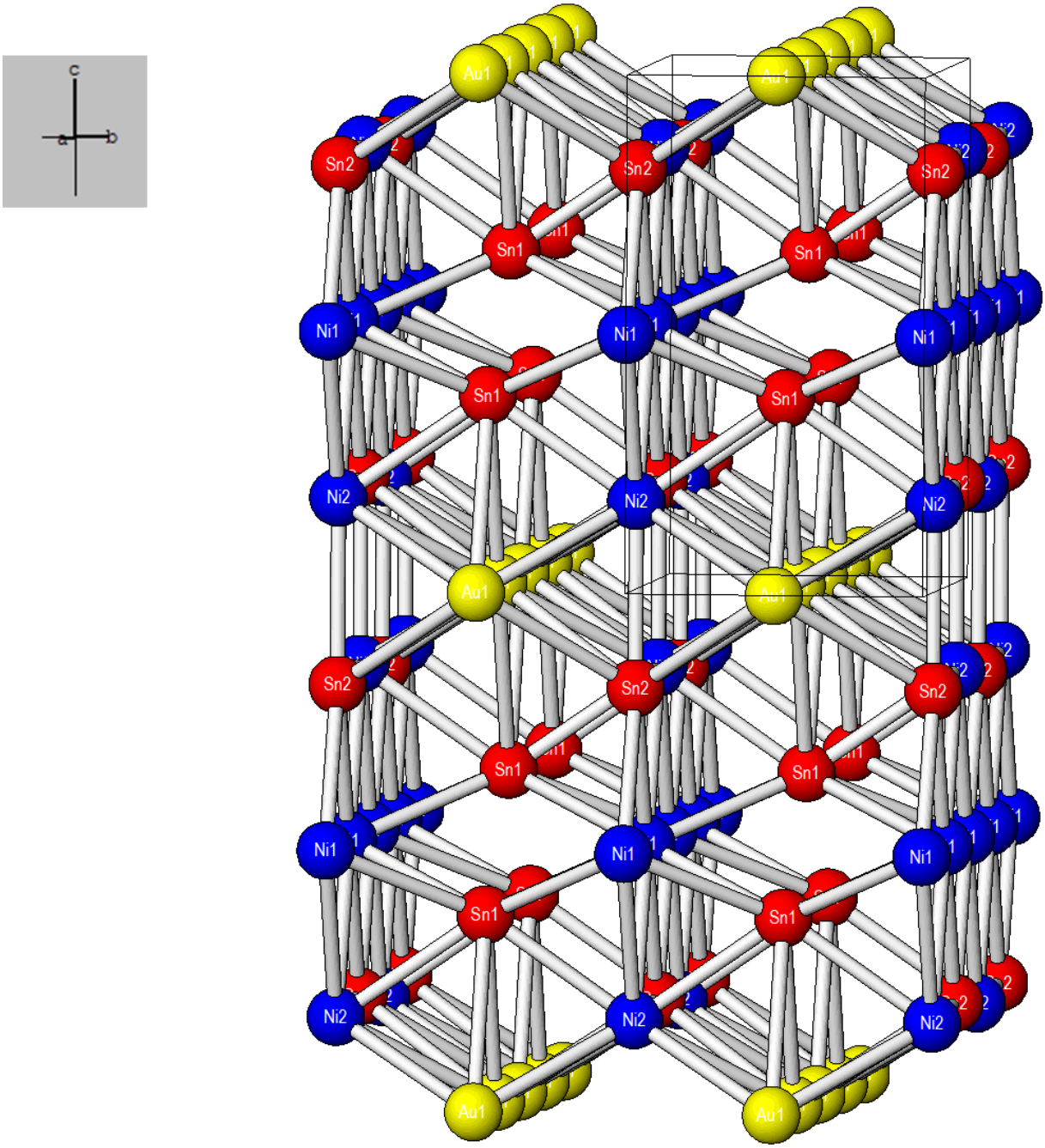

Figure 3.3.4 – Au and Ni chains in $AuNi_2Sn_2$ with Au on position Au1 and Ni on position Ni1

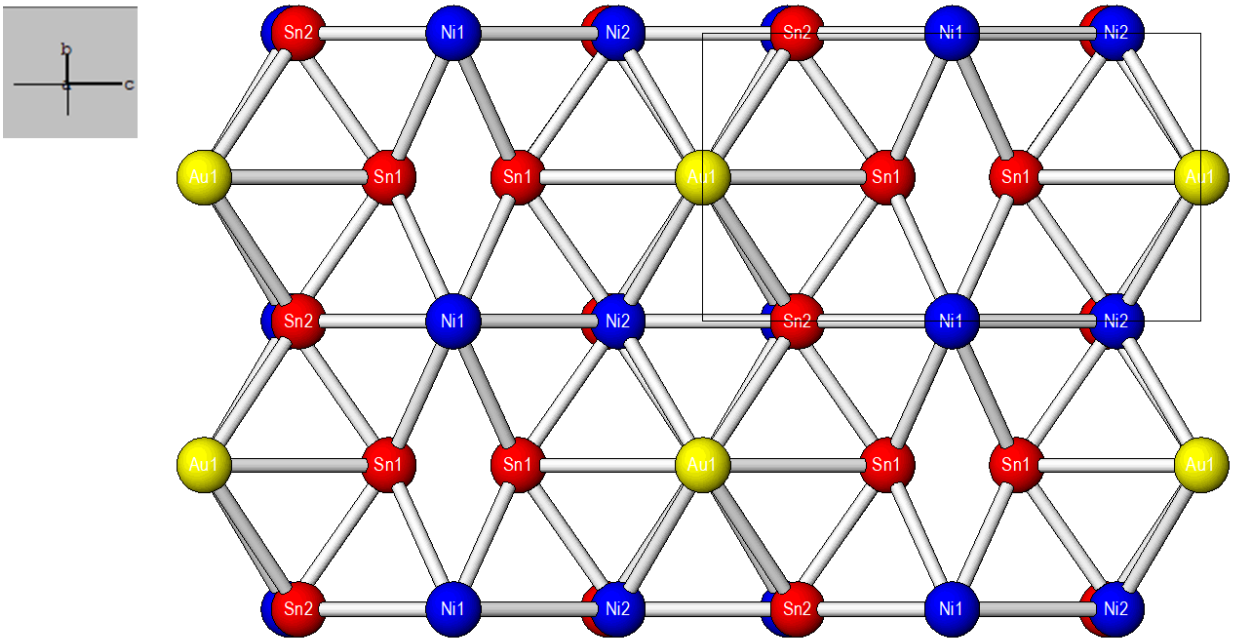

Figure 3.3.5 – Pseudo-hexagonal arrangement in $AuNi_2Sn_2$ with Au on position Au1 and Ni on position Ni1

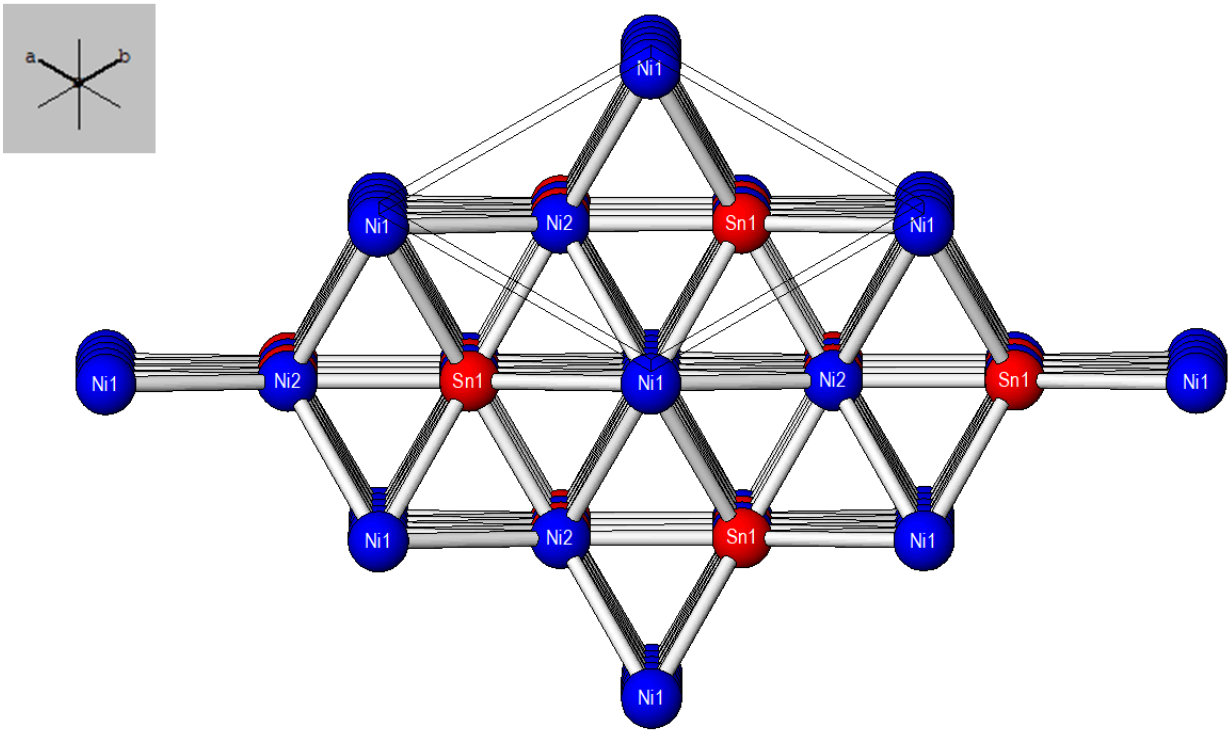

Figure 3.3.6 – Hexagonal order in $(Au,Ni)_3Sn_2$ with Ni on position Ni1

As seen in Figures 3.3.5 and 3.3.6, the arrangement in $AuNi_2Sn_2$ is pseudo-hexagonal and resembles the arrangement in $(Au,Ni)_3Sn_2$. The *a*-axis in the $AuNi_2Sn_2$ is equal to the *c*-axis in the hexagonal $(Au,Ni)_3Sn_2$ structure. Therefore $AuNi_2Sn_2$ is an orthorhombically distorted superstructure of $(Au,Ni)_3Sn_2$. In $(Au,Ni)_3Sn_2$ there are chains of Ni alternating with Sn (Figure 3.3.6). In $AuNi_2Sn_2$, although there are chains of Ni and Sn on positions Ni1 and Sn2 respectively, there are vacancies around Sn on position Sn2 and therefore there is no consistent alternation with Ni (Figure 3.3.5). In $AuNi_2Sn_2$ there are more vacancies around position Ni1 compared to position Ni1 in $(Au,Ni)_3Sn_2$. Furthermore, in $AuNi_2Sn_2$ the order is altered, as there are additional chains of Au on position Au1 (Figure 3.3.4). However, Au can be exchanged for Ni on position Au1 and Ni can be exchanged for Au on position Ni1, depending on the composition. In $(Au,Ni)_3Sn_2$ position Ni1 also has mixed occupations of Au and Ni. The interstitial position Ni2 is underoccupied in both $(Au,Ni)_3Sn_2$ and $AuNi_2Sn_2$, with the occupation depending on the composition.

The phases, lattice parameters as well as compositions determined by P-XRD and SEM of additional samples are listed in Table 3.3.4. Samples AuNiSn 10-14 were not completely homogenous, as composition differences were observed in SEM. Therefore, subsequent samples AuNiSn 15 and 20 were annealed at higher temperature in order to achieve a better state of equilibrium. The SEM images of samples AuNiSn 10-15 and 20 are shown in Figure 3.3.7.

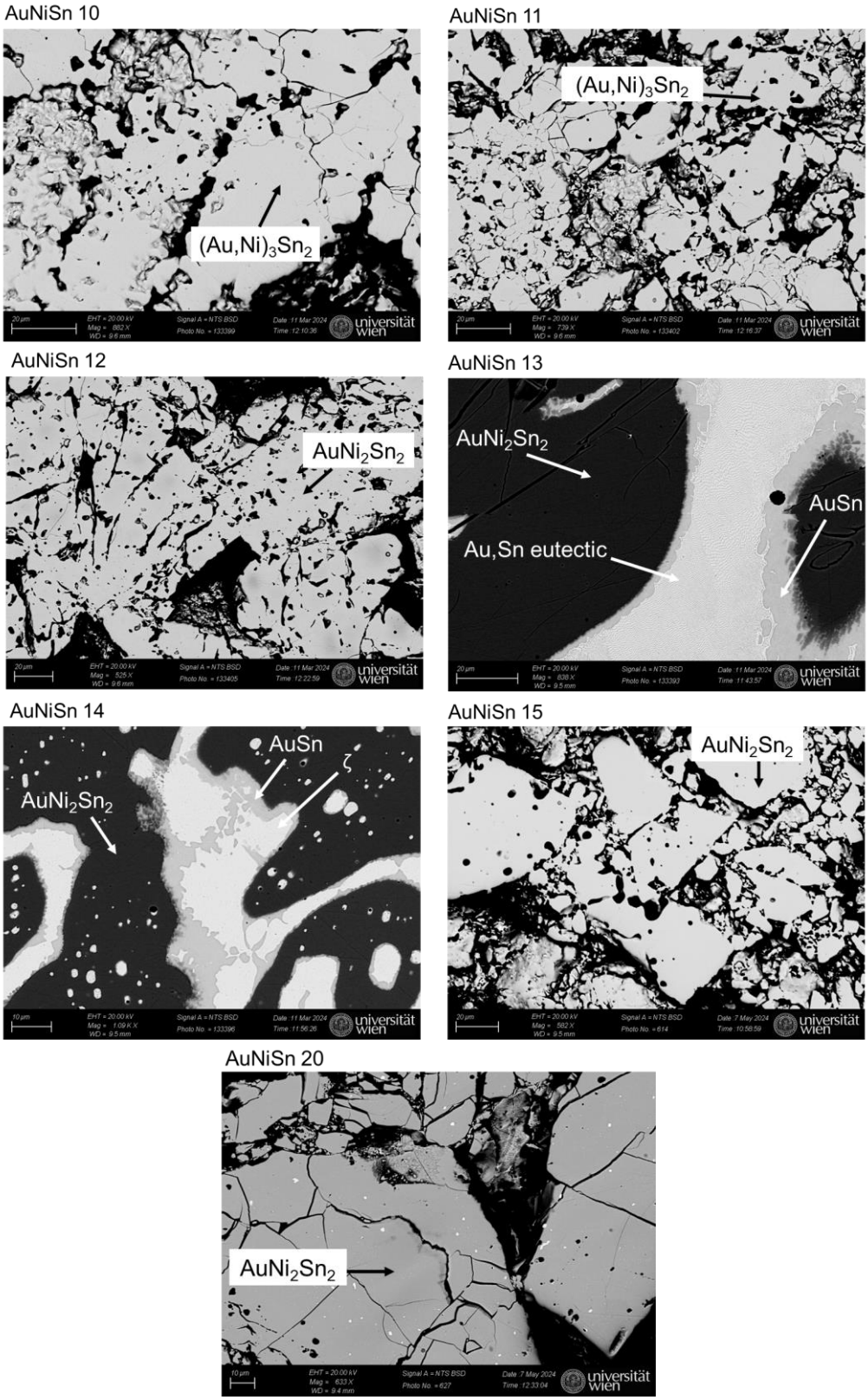

Figure 3.3.7 – SEM images of samples AuNiSn 10-15 and 20

Table 3.3.4 – Au-Ni-Sn samples, their phases, lattice parameters and compositions determined by P-XRD and SEM

							Composition determined by P-XRD (at. %)			Composition determined by SEM (at. %)		
Sample	(Au/Ni/Sn)	Phase	Fraction (%)	a (Å)	b (Å)	c (Å)	Au	Ni	Sn	Au	Ni	Sn
10	(21.0/34.5/44.5)	(Au,Ni)3Sn2	100	4.173	-	5.327	24	31	45	21.97 ± 0.33	32.60 ± 0.41	45.43 ± 0.09
11	(18.0/38.5/43.5)	(Au,Ni)3Sn2	100	4.166	-	5.319	21	36	43	18.06 ± 0.10	37.92 ± 0.28	44.02 ± 0.18
12	(14.0/43.5/42.5)	$AuNi_2Sn_2$	100	5.303	4.152	7.190	16	41	43	13.10 ± 1.91	44.21 ± 2.41	42.69 ± 0.52
13	(28.0/32.0/40.0)	AuSn	-	4.306	-	5.533	50	-	50	46.71 ± 1.07	3.77 ± 1.44	49.52 ± 0.40
		Au, Sn eutectic	-	-	-	-	-	-	-	69.45 ± 0.11	-	30.55 ± 0.11
		$AuNi_2Sn_2$	-	5.290	4.146	7.181	15	43	42	13.41 ± 0.12	43.45 ± 0.32	43.14 ± 0.22
14	(24.0/38.0/38.0)	ζ	2	2.938	-	4.768	85	-	15	82.61 ± 1.04	0.45 ± 0.89	16.95 ± 0.54
		AuSn	8	4.306	-	5.509	50	-	50	47.68 ± 0.59	3.20 ± 0.94	49.12 ± 0.41
		$AuNi_2Sn_2$	90	5.296	4.144	7.177	13	45	42	10.83 ± 0.08	47.59 ± 0.28	41.59 ± 0.23

Table 3.3.4 (continued) – Au-Ni-Sn samples, their phases, lattice parameters and compositions determined by P-XRD and SEM

							Composition determined by P-XRD (at. %)			Composition determined by SEM (at. %)		
15	(9.5/47.5/43.0)	$AuNi_2Sn_2$	100	5.321	4.121	7.137	12	45	43	9.80 ± 0.26	46.47 ± 0.67	43.73 ± 0.44
20	(5.5/54.5/50.0)	$AuNi_2Sn_2$	100	5.229	4.132	7.156	8	51	41	5.45 ± 0.57	53.41 ± 0.61	41.16 ± 0.27

$AuNi_2Sn_2$ was detected in samples 12 – 15, and 20, as well as in seven samples prepared in preliminary works by students during laboratory courses (45). The composition of the superstructure determined by SEM of each sample is listed in Table 3.3.5. A corresponding phase field of $AuNi_2Sn_2$ was added to the Au-Ni-Sn phase diagram and is shown in Figure 3.3.8. The superstructure is present on the phase boundary of $(Au,Ni)_3Sn_2$ and also extends beyond the phase border of $(Au,Ni)_3Sn_2$ in the ternary phase diagram.

Table 3.3.5 – Composition of $AuNi_2Sn_2$ in different samples measured by SEM

Sample	Au (at. %)	Ni (at. %)	Sn (at. %)
12	13.10	44.21	42.69
13	13.41	43.45	43.14
14	10.83	47.59	41.58
15	9.80	46.47	43.73
20	5.45	53.41	41.16
SS20_15	15.60	41.32	43.08
SS20_16	13.20	44.46	42.34
SS20_17	10.84	47.79	41.37
SS20_18	8.21	51.58	40.21
SS21_4	19.13	37.61	43.26
SS21_10	22.35	33.89	43.76
SS21_11	22.17	33.53	44.26

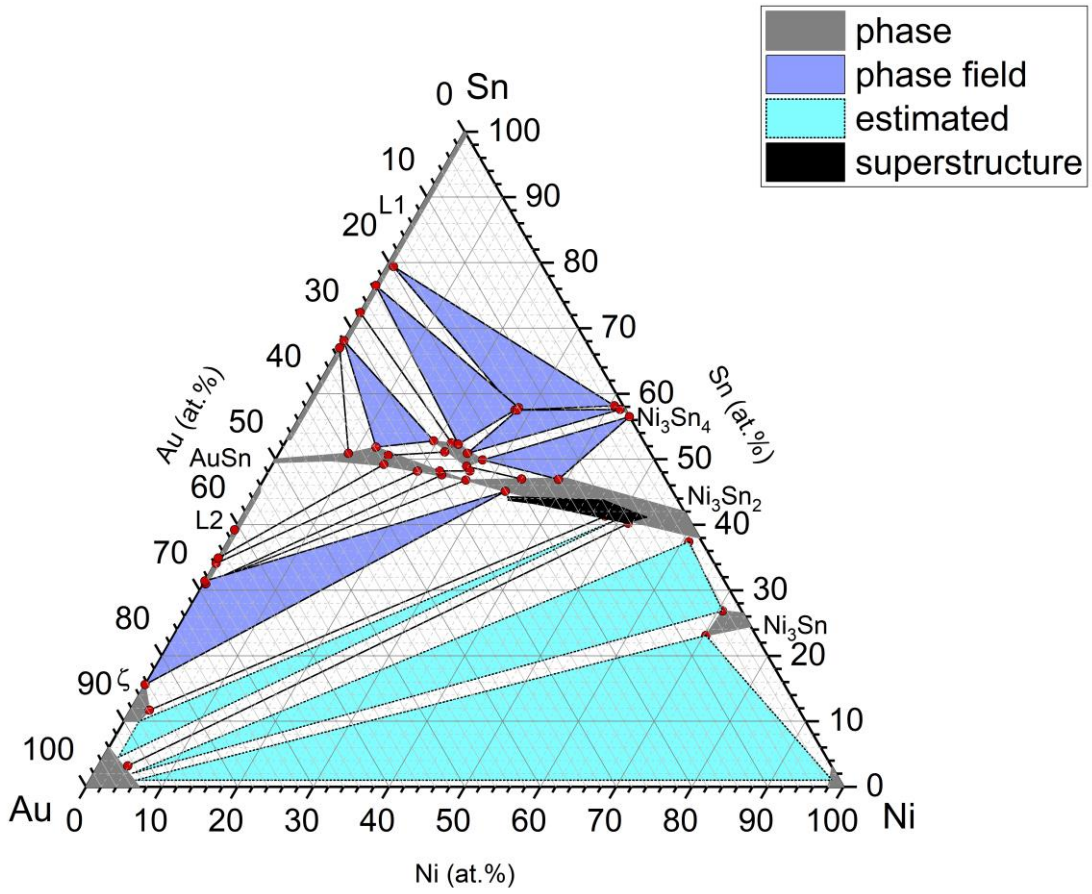

Figure 3.3.8 – Au-Ni-Sn phase diagram with the $AuNi_2Sn_2$ region

4. Conclusion

In conclusion, the systems Al-Fe-Ge, Au-Si-Ti and Au-Ni-Sn were investigated to characterize unknown phases. In Al-Fe-Ge the phase $\tau 8$ was synthesized and characterized as orthorhombic of space group *Fmm2* and formula Al_7FeGe_2. The occupational models in the independent atomic positions were discussed. In Au-Si-Ti, phase T2 was synthesized and characterized as cubic of space group *I43d* and formula $Au_{8-x}Si_6Ti_9$ ($x \sim 0.9$). The structure was discussed in relation to the structure of phase T1. Furthermore, an oxygen-stabilized variation of Si_3Ti_5, Si_3Ti_5O, was discovered and characterized. It was also found that Ti may partially occupy the additional 2 (*b*) site, explaining the homogeneity range of Si_3Ti_5. In Au-Ni-Sn, a superstructure of $(Au,Ni)_3Sn_2$, $AuNi_2Sn_2$, with space group *Pmma* was characterized. The presence of the superstructure in the ternary phase diagram was determined and added to the phase diagram.

5. Bibliography

1. Han J, Matsubara S, Moriguchi S, Kaliske M, Terada K. Crack phase-field model equipped with plastic driving force and degrading fracture toughness for ductile fracture simulation. *Computational Mechanics*. 2022;69(1): 151–175. https://doi.org/10.1007/s00466-021-02087-1.

2. Liu Y, Huang ZR, Liu XJ. Joining of sintered silicon carbide using ternary Ag-Cu-Ti active brazing alloy. *Ceramics International*. 2009;35(8): 3479–3484. https://doi.org/10.1016/j.ceramint.2009.03.016.

3. Massalski TB, Okamoto H, Subramanian PR, Kacprzak L. *Binary Alloy Phase Diagrams, 2nd Edition*.. 2nd ed. ASM International; 1990.

4. *Directive 2011/65/EU of the European Parliament and of the Council of 8 June 2011 on the restriction of the use of certain hazardous substances in electrical and electronic equipment (recast) Text with EEA relevance*. OJ L Jun 8, 2011. http://data.europa.eu/eli/dir/2011/65/oj/eng [Accessed 7th March 2024].

5. *The Safe Drinking Water Act as amended by The Safe Drinking Water Act of 1996 Public Law 104–182, August 6, 1996*. U.S. Government Printing Office; 2000.

6. Chen Z, He M, Kumar A, Qi GJ. Effect of Interfacial Reaction on the Tensile Strength of Sn-3.5Ag/Ni-P and Sn-37Pb/Ni-P Solder Joints. *Journal of Electronic Materials*. 2007;36(1): 17–25. https://doi.org/10.1007/s11664-006-0008-1.

7. Dunn BD. Whisker Formation on Electronic Materials. *Circuit World*. 1976;2(4): 32–40. https://doi.org/10.1108/eb043543.

8. Moon KW, Boettinger WJ, Kattner UR, Biancaniello FS, Handwerker CA. Experimental and thermodynamic assessment of Sn-Ag-Cu solder alloys. *Journal of Electronic Materials*. 2000;29(10): 1122–1136. https://doi.org/10.1007/s11664-000-0003-x.

9. Miller CM, Anderson IE, Smith JF. A viable tin-lead solder substitute: Sn-Ag-Cu. *Journal of Electronic Materials*. 1994;23(7): 595–601. https://doi.org/10.1007/BF02653344.

10. Kim KS, Huh SH, Suganuma K. Effects of intermetallic compounds on properties of Sn-Ag-Cu lead-free soldered joints. *Journal of Alloys and Compounds*. 2003;352(1–2): 226–236. https://doi.org/10.1016/S0925-8388(02)01166-0.

11. Hammad AE. Evolution of microstructure, thermal and creep properties of Ni-doped Sn–0.5Ag–0.7Cu low-Ag solder alloys for electronic applications. *Materials & Design (1980-2015)*. 2013;52: 663–670. https://doi.org/10.1016/j.matdes.2013.05.102.

12. Kim KS, Huh SH, Suganuma K. Effects of cooling speed on microstructure and tensile properties of Sn-Ag-Cu alloys. *Materials Science and Engineering A*. 2002;333(1–2): 106–114. https://doi.org/10.1016/S0921-5093(01)01828-7.

13. Sayyadi R, Naffakh-Moosavy H. The Role of Intermetallic Compounds in Controlling the Microstructural, Physical and Mechanical Properties of Cu-[Sn-Ag-Cu-Bi]-Cu Solder Joints. *Scientific Reports*. 2019;9(1): 8389. https://doi.org/10.1038/s41598-019-44758-3.

14. Rosalbino F, Zanicchi G, Carlini R, Angelini E, Marazza R. Electrochemical corrosion behaviour of Sn–Ag–Cu (SAC) eutectic alloy in a chloride containing environment. *Materials and Corrosion*. 2012;63(6): 492–496. https://doi.org/10.1002/maco.201005979.

15. Mousavi T, Aksoy C, Grovenor CRM, Speller SC. Microstructure and superconducting properties of Sn–In and Sn–In–Bi alloys as Pb-free superconducting solders. *Superconductor Science and Technology*. 2015;29(1): 015012. https://doi.org/10.1088/0953-2048/29/1/015012.

16. Lan X, Li K, Wang J, Yang M, Lu Q, Du Y. Developing Al–Fe–Si alloys with high thermal stability through tuning Fe, Si contents and cooling rates. *Intermetallics*. 2022;144: 107505. https://doi.org/10.1016/j.intermet.2022.107505.

17. Burzyńska-Szyszko M, Fadeeva VI, Matyja H. Formation of ternary intermetallic phase by mechanical alloying of Al-Fe-Ge. *Materials Science Forum*. 1997;235–238(PART 1): 97–102. https://doi.org/10.4028/www.scientific.net/MSF.235-238.97.

18. Reisinger GR, Effenberger HS, Richter KW. Al-Fe-Ge: Phase equilibria and new ternary compounds at 400 °C. *Journal of Alloys and Compounds*. 2022;905: 164178. https://doi.org/10.1016/j.jallcom.2022.164178.

19. Reisinger GR, Effenberger HS, Richter KW. Al–Fe–Ge: New ternary compounds and phase equilibria at 800 °C. *Journal of Alloys and Compounds*. 2018;762: 849–857. https://doi.org/10.1016/j.jallcom.2018.05.214.

20. Golovin IS, Strahl A, Neuhäuser H. Anelastic relaxation and structure of ternary Fe-Al-Me alloys with Me = Co, Cr, Ge, Mn, Nb, Si, Ta, Ti, Zr. *International Journal of Materials Research*. 2006;97(8): 1078–1092. https://doi.org/10.3139/146.101341.

21. Rosalbino F, Carlini R, Parodi R, Zanicchi G. Effect of silicon and germanium alloying additions on the passivation characteristics of Fe 3Al intermetallic in sulphuric acid solution. *Electrochimica Acta*. 2012;62: 305–312. https://doi.org/10.1016/j.electacta.2011.12.031.

22. Kanibolotsky DS, Lisnyak VV. Thermodynamics of formation of aluminum-iron-germanium amorphous alloys. *Journal of Non-Crystalline Solids*. 2004;333(2): 194–198. https://doi.org/10.1016/j.jnoncrysol.2003.09.054.

23. Yakovenko OM, Roik OS, Kazimirov VP, Sokol'skii VE, Golovataya NV, Zelinskaya GM, et al. Structure of the Al–Ge–Fe alloys in the liquid and solid

state. *Journal of Non-Crystalline Solids*. 2017;455: 75–82. https://doi.org/10.1016/j.jnoncrysol.2016.10.026.

24. Yokoyama Y, Yamada Y, Yamaguchi A, Matono K, Fukaura K, Sunada H. Phase transition and magnetic properties of supercooled Al-Ge-TM (TM=Cr, Fe, Co) alloys. *Materials Transactions, JIM*. 1998;39(4): 433–438. https://doi.org/10.2320/matertrans1989.39.433.

25. Reisinger GR, Effenberger HS, Richter KW. Al7+xFe23Ge14−xand Al7+xFe9Ge5−x: Two new ternary compounds related to Fe6Ge5. *Journal of Alloys and Compounds*. 2017;693: 692–699. https://doi.org/10.1016/j.jallcom.2016.09.236.

26. Restorff JB, Wun-Fogle M, Hathaway KB, Clark AE, Lograsso TA, Petculescu G. Tetragonal magnetostriction and magnetoelastic coupling in Fe-Al, Fe-Ga, Fe-Ge, Fe-Si, Fe-Ga-Al, and Fe-Ga-Ge alloys. *Journal of Applied Physics*. 2012;111(2). https://doi.org/10.1063/1.3674318.

27. Kanibolotsky DS, Kotova NV, Bieloborodova OA, Lisnyak VV. Enthalpies of mixing of liquid Al-Fe-Ge alloys. *Zeitschrift fuer Metallkunde/Materials Research and Advanced Techniques*. 2003;94(12): 1280–1292. https://doi.org/10.3139/146.031293.

28. Beloborodova EA, Kanibolotskii DS, Zinevich TN, Kotova NV. Thermodynamics of component interactions in Ge−Fe−Al liquid alloys. *Powder Metallurgy and Metal Ceramics*. 1999;38(7): 381–386. https://doi.org/10.1007/BF02676174.

29. Roik OS, Yakovenko OM, Kazimirov VP, Sokol'skii VE, Golovataya NV, Zelinskaya GM. Formation of short-range order in Al–Ge–Fe melts: influence of composition. *Physics and Chemistry of Liquids*. 2020;58(1): 94–104. https://doi.org/10.1080/00319104.2018.1550776.

30. Smolenskaya GN, Kudryavtsev NT. Electroplating of titanium. *Metal Science and Heat Treatment*. 1960;2(11): 615–616. https://doi.org/10.1007/BF00651936.

31. Smeltzer CE, Hammer AN. *Titanium braze system for high temperature applications. Final technical report*. Report number: AD-A-036575; RDR-1786-6, 1976 Aug [Accessed 10th March 2024]. https://www.osti.gov/biblio/7301261 [Accessed 10th March 2024].

32. Gorynin IV, Farmakovsky BV, Vasiliev AF, Vinogradova TS, Samodelkin EA. Activated soldering of dissimilar materials with amorphous solders. *Inorganic Materials: Applied Research*. 2017;8(6): 892–898. https://doi.org/10.1134/S2075113317060053.

33. Pertlik J. Das System Au-Si-Ti. 2019; https://doi.org/10.25365/thesis.57081.

34. Harpster TJ, Najafi K. Field-assisted bonding of glass to Si-Au eutectic solder for packaging applications. In: *IEEE The Sixteenth Annual International Conference on Micro Electro Mechanical Systems, 2003. MEMS-03 Kyoto*.

2003. p. 630–633. https://doi.org/10.1109/MEMSYS.2003.1189828. [Accessed 1st March 2024].

35. Weyrich N, Leinenbach C. Low temperature TLP bonding of Al2O3-ceramics using eutectic Au-(Ge, Si) alloys. *Journal of Materials Science*. 2013;48(20): 7115–7124. https://doi.org/10.1007/s10853-013-7526-z.

36. Tiensuu AL, Bexell M, Schweitz JÅ, Smith L, Johnsson S. Assembling three-dimensional microstructures using gold-silicon eutectic bonding. *Sensors and Actuators A: Physical*. 1994;45(3): 227–236. https://doi.org/10.1016/0924-4247(94)00836-1.

37. Wolffenbuttel RF. Low-temperature intermediate Au-Si wafer bonding; eutectic or silicide bond. *Sensors and Actuators, A: Physical*. 1997;62(1–3): 680–686. https://doi.org/10.1016/S0924-4247(97)01550-1.

38. Chidambaram V, Yeung HB, Shan G. Reliability of Au-Ge and Au-Si eutectic solder alloys for high-temperature electronics. *Journal of Electronic Materials*. 2012;41(8): 2107–2117. https://doi.org/10.1007/s11664-012-2114-6.

39. Onzawa T, Suzumura A, Ko MW. Brazing of Titanium Using Low-Melting-Point Ti-Based Filler Metals. *Welding Research Supplement*. 1990; 462–467.

40. Henderson B, Raynor GV. The effective valencies of transition metals in solid solution in gold and silver alloys. *Proceedings of the Royal Society of London. Series A. Mathematical and Physical Sciences*. 1962;267(1330): 313–328. https://doi.org/10.1098/rspa.1962.0102.

41. Neumann A, Kjekshus A, Rømming C, Røst E. The crystal structure of AuNi2Sn4. *Journal of Solid State Chemistry*. 1995;119(1): 142–146. https://doi.org/10.1016/0022-4596(95)80021-G.

42. Lange S, Nilges T, Hoffmann RD, Pöttgen R. The Stannides AuNiSn2 and AuCuSn2 – Bulk Synthesis and Superstructure Determination. *Zeitschrift für anorganische und allgemeine Chemie*. 2006;632(7): 1163–1166. https://doi.org/10.1002/zaac.200500414.

43. Neumann A, Kjekshus A, Røst E. The Ternary System Au–Ni–Sn. *Journal of Solid State Chemistry*. 1996;123(2): 203–207. https://doi.org/10.1006/jssc.1996.0169.

44. Lidin S, Larsson AK. A Survey of Superstructures in Intermetallic NiAs-Ni2In-Type Phases. *Journal of Solid State Chemistry*. 1995;118(2): 313–322. https://doi.org/10.1006/jssc.1995.1350.

45. Flandorfer H, Richter KW. *Unpublished Results*. University of Vienna;

46. Lyubimtsev AL, Baranov AI, Fischer A, Kloo L, Popovkin BA. The structure and bonding of Ni3Sn. *Journal of Alloys and Compounds*. 2002;340(1): 167–172. https://doi.org/10.1016/S0925-8388(02)00047-6.

47. Xian C, Wang J. Synthesis, magnetic and transport properties of HTP-Ni3Sn2 single crystals obtained by the chemical vapor transport method. *RSC Advances*. 2017;8(1): 213–216. https://doi.org/10.1039/C7RA12322A.

48. Jaberg B, Jeitschko W. Structure refinement of Ni3Sn4. *Acta Crystallographica Section B: Structural Crystallography and Crystal Chemistry*. 1982;38(2): 598–600. https://doi.org/10.1107/S056774088200346X.

49. Song HG, Ahn JP, Morris JW. The microstructure of eutectic Au-Sn solder bumps on Cu/electroless Ni/Au. *Journal of Electronic Materials*. 2001;30(9): 1083–1087. https://doi.org/10.1007/s11664-001-0133-9.

50. Yoon JW, Jung SB. Investigation of interfacial reaction between Au–Sn solder and Kovar for hermetic sealing application. *Microelectronic Engineering*. 2007;84(11): 2634–2639. https://doi.org/10.1016/j.mee.2007.05.058.

51. Yang CY, Laksono AD, Yen YW, Guo YZ, Wang CH, Li JL, et al. Investigation of phase equilibria of the Au–Ni–Sn ternary system and interfacial reactions in the Au/Sn/Ni/Cu multilayer couple. *Materials Chemistry and Physics*. 2022;289: 126494. https://doi.org/10.1016/j.matchemphys.2022.126494.

52. Brandon DG, Kaplan WD. *Microstructural Characterization of Materials*.. 2nd ed. Wiley & Sons Ltd; 2008.

53. Zhao JC. *Methods for Phase Diagram Determination*.. 1st ed. Elsevier Science; 2007.

54. Marker M University of Vienna;

55. Emsley J. *The Elements*.. 2nd ed. Clarendon Press; 1989.